PULSAR SEARCHING WITH THE EFFELSBERG TELESCOPE

Dissertation

zur

Erlangung des Doktorgrades (*Dr. rer. nat.*)

der

Mathematisch-Naturwissenschaftlichen Fakultät

der

Rheinischen Friedrich–Wilhelms–Universität, Bonn

vorgelegt von

Marina Berezina

aus

Woronesch, Russland

Bonn, 2018

Angefertigt mit Genehmigung der Mathematisch-Naturwissenschaftlichen Fakultät
der Rheinischen Friedrich–Wilhelms–Universität Bonn

1. Referent: Prof. Dr. Michael Kramer
2. Referent: Prof. Dr. Norbert Langer
Tag der Promotion: 01.04.2019
Erscheinungsjahr: 2020

RHEINISCHE FRIEDRICH–WILHELMS–UNIVERSITÄT BONN

Abstract

of the dissertation "Pulsar searching with the Effelsberg telescope"

by Marina Berezina

for the degree of

Doctor rerum naturalium

Pulsars proved themselves as incredible tools for exploring many aspects of fundamental physics inaccessible on the Earth. Tiny in size but big in promise, these highly-magnetised rotating neutron stars find their application, for example, in studying matter at supranuclear densities and probing the interstellar medium, revealing the formation and evolution of binary systems and testing general relativity. More opportunities for building new theories and challenging the existing ones (in particular, theories of gravity) come with new pulsar discoveries, hence, are determined by the success of ongoing pulsar surveys. In this thesis, I present one such ambitious searching project, the Northern High Time Resolution Universe survey (HTRU-North) for pulsars and fast transients conducted with the Effelsberg telescope, and report on the scientific exploitation of the discoveries made.

The HTRU-North was initiated in 2010, aiming to perform the first-ever scanning of the whole northern sky at the L-band with high time and frequency resolution. By the end of its first stage in early 2013, after observing a small portion of the medium Galactic latitudes ($|b| < 15°$) with 3-minute integrations, the survey has already discovered 15 new pulsars. This determined the main goal for the second stage of the survey, which took place within the timescale of this thesis: to cover more mid-latitudes and perform a shallow (3-minute) sweep of the low Galactic latitudes ($|b| < 3.5°$) in hope of quickly finding many more bright pulsars. During this work, the percentage of the observed mid-latitude pointings reached 50%, with encompassing a total sky area of $\sim 7620\,\mathrm{deg}^2$. All the recorded data have been processed with the quick-look pipeline, without performing the acceleration search needed for short period pulsars in tight binary orbits. This resulted in 15 new discoveries, among which are 2 binary millisecond pulsars (MSPs), PSR J2045+3633 ($P = 31.7$ ms) and PSR J2053+4650 ($P = 12.6$ ms), and a relatively young pulsar, PSR J1951+4721. Nine of these pulsars were also found by other surveys at about the same time. Including these co-detections into the survey statistics brought the total yield to 30, which appeared to be less than half the number predicted for this portion of the mid-latitude pointings. To find out whether a potentially reduced survey sensitivity could be responsible for this,

I performed the analysis of 202 known pulsar redetections. This analysis showed that the survey is indeed slightly less sensitive than expected, most likely because of the influence of RFI which was either initially underestimated or became much more significant during the last years. From this we concluded that RFI could theoretically have prevented the discovery of some new pulsars. However, it also seems likely that inaccuracy of the models (the Galactic pulsar population model and the Galactic electron density model) used for estimating the discovery rate could be another reason for the discrepancy between the expected and observed yields. In particular, the publication of a new Galactic electron density model now places many known pulsars further away from the Earth what reduces the expected number of discoveries for any sensitivity-limited survey.

A considerable amount of this thesis work was devoted to studying the most interesting new discoveries, PSR J2045+3633 and PSR J2053+4650. Though both of them are mildly recycled (spun up through the accretion of material from an evolved companion) and have massive CO or ONeMg white dwarf (WD) companions, their totally different orbital period and eccentricity suggest that they followed different evolutionary paths. With a long-term goal of getting a closer insight into their formation history and a short-term goal of measuring the pulsar and companion masses, we started timing campaigns. The favourable orbital parameters of both pulsars – the relatively high eccentricity of PSR J2045+3633, $e = 0.01721244(5)$, and the nearly edge-on orbital configuration of PSR J2053+4650 – allowed us, in nearly two years, to obtain the following constraints (with the assumption of general relativity): $M_p = 1.33^{+0.30}_{-0.28}\,M_\odot$ and $M_c = 0.94^{+0.14}_{-0.13}\,M_\odot$ for PSR J2045+3633, and $M_p = 1.40^{+0.21}_{-0.18}\,M_\odot$, and $M_c = 0.86^{+0.07}_{-0.06}\,M_\odot$ for PSR J2053+4650.

Additionally I report on the results of the long-term timing campaign carried out for PSR J1946+3417, the first MSP discovered in the HTRU-North. PSR J1946+3417, orbiting an intermediate-mass He WD companion, has a relatively high orbital eccentricity, $e \sim 0.13$, unusual for this type of systems, hence, raising questions about its formation. The multi-telescope timing campaign aimed to use the benefits of this high eccentricity to precisely measure the advance of periastron which, when combined with a measurement of the Shapiro delay, allowed for a precise determination of the pulsar and the companion masses. The obtained values, $M_p = 1.828(22)\,M_\odot$ and $M_c = 0.2656(19)\,M_\odot$, apart from placing PSR J1946+3417 in the position of the third most massive pulsar currently known, helped to narrow down the list of possible evolutionary scenarios suggested for this binary. For this project my main contribution was the reduction and analysis of the Effelsberg timing data, coupled with occasional observations.

Techniques used for pulsar searching are also sensitive to other types of astrophysical sources, in particular, to transients such as fast radio bursts (FRBs). FRBs are millisecond-duration pulses of unclear origin likely coming from outside the Galaxy. All but one of a few dozens of FRBs known to date are observed

to be one-off events. With only a single burst it is impossible to determine their exact locations and, therefore, progenitors. Intensive follow-up of known FRB fields carried out with many telescopes, sometimes at multiple frequencies in parallel, aim to detect additional bursts or a potential afterglow that could help identify their host galaxies. As a supplementary project within this thesis work, I present the follow-up of FRB 150418 first detected at Parkes. In particular, I focus on 2.3-hour observations performed with the Effelsberg telescope as part of an international collaboration. These observations, as well as the whole multi-telescope campaign, resulted in no additional burst detections. However, radio imaging showed a potentially related afterglow located in the galaxy WISE 0716-19, although this has been disputed. I describe the processing and analysis of the Effelsberg data and give the upper limits on the flux density for non-detection.

Acknowledgements

Though I am very grateful to everyone whom I met during my PhD and who influenced me during these years, I want to express special thanks to the following people:

• Dr. Norbert Wex and Prof. Dr. Michael Kramer – for giving me a possibility to be a part of this fantastic team and make scientific history;

• David Champion – for being a very thoughtful supervisor and one of the most wonderful people I've ever met, for helping me to overcome my biases and unnecessary perfectionism and showing how real science works, for a long-term support and for the 5-year old "I wish my German was even half as good as your English". Of course, I did not believe you :) but that was inspiring.

• Ralph Eatough – for my first steps in pulsar science;

• Ewan Barr – for writing the original version of the FAST PIPELINE and bequeathing it to me;

• Laura Spitler - for helping a lot with observations;

• Paulo Freire and Gregory Desvignes – for helping with timing and polarisation data reduction;

• Cherry Ng, Sylvia Carolina Mora, Pablo Torne Torres, Patrick Lazarus and Eleni Graikou – for my first international friendships;

• Dominic Schnitzler, Alessandro Ridolfi and James McKee – for cordial conversations and my further international friendships;

• Alice Pasetto, Ancor Damas and Tilemachos Athanasiadis – for being good friends and perfect officemates;

• Jason Wu, Leon Houben, Andrew Cameron and Joey Martinez – for giving good apropos advices;

• Marilyn Cruces – for making me feel useful;

• Maja Kierdorf, Yik Ki (Jackie) Ma and Madhuri Gaikwad – for nice antidepressive lunches;

• Alexandra Kozyreva and Galina Kozyreva – for becoming my second family during their time in Bonn;

• Frau Erika Schneider, Nataliya Porayko and Victoria Yankelevich – for providing the kindest and funniest Russian-speaking environment;

• Kira Kühn, Tuyet-Le Tran and Barbara Menten – for making my German life much easier;

• my former landlord Christoph Dohmgörgen and my current landlords Renita and Manfred Bublies – for hospitality, a lot of help and pleasant life conditions;

• my former supervisor Alexander Zavrazhnov (Voronezh State University) – for nourishing my natural need for broad knowledge and interests;

• Maryna Immel and Kindermusiktheater "Marissel" – for immersing me into a fairytale when it was extremely necessary;

• the Orchestra of Collegium Musicum Bonn for the most passionate musical moments, very inspiring Probenwochenende and a more Russian than played by Russians performance of the works by Tschaikowski, Glasunov, Rachmaninoff.

• • • (related to the pervious item) Peter Ilyitch Tschaikowski – for including the famous Russian folk song about the birch tree ("bereza") into the fourth movement of his Symphony N4. This "plagiarism" appeared to be life-changing for me, and, probably, influenced the fate of this thesis as well.

• my closest friends Valeria Kasatkina, Maria Druzhinina and Svetlana Poltoran – for being with me despite the distance separating us;

• my violin teacher Irina Geladze – for more than 20 years of my musical and, in general, cultural education, without this I would be a totally different person;

• and the biggest "spasibo" to my family (and cat Physteshka who skyped with me until her last day) for everyday support and compassion.

Contents

List of Figures

List of Tables

Chapter 1

Introduction

A pulsar is a rapidly rotating highly magnetised neutron star emitting beams of electromagnetic radiation along its magnetic axis. Due to rotation and misalignment of the magnetic and rotational axes, the directed beam crosses our line-of-sight periodically and, thus, can be detected in series of pulses. The temporal separation between these pulses is determined by the period of the neutron star's rotation. Not all neutron stars can be observed as pulsars, either due to the unfavourable beam configuration relative to Earth or due to the weakness of their signals (compared to the detection threshold of our instruments). For the majority of known pulsars, their electromagnetic radiation is detected in the radio band. Some pulsars can be detected in the optical, X-ray and/or γ-ray bands. With all the respect to the whole pulsar population, this thesis work is devoted to radio pulsars.

Per aspera ad astra pulsaris

The existence of stellar objects where "atomic nuclei come in close contact forming one gigantic nucleus" was first anticipated in 1931 by the Soviet physicist L.D. Landau (Landau, 1932). However, the concept of neutron stars as one of the possible endpoints of stellar evolution produced in supernova explosions saw the light a bit later, in 1934, in the work by Baade & Zwicky (1934). Thought to be composed of extremely tightly packed neutrons ($\sim 10^{15}\,\mathrm{g\,cm^{-3}}$), these objects should be supported in equilibrium due to the balance between gravity and pressure of a degenerate cold Fermi gas. The first attempts to obtain the equation of state, as well as estimates of possible limits on the masses of neutron stars, were made already at the late 1930-s by Oppenheimer & Volkoff (1939) and Tolman (1939). Unfortunately, the lack of knowledge about nuclear interactions at that time prevented the authors from getting non-contradictory results: the obtained upper limit for neutron star masses, $\mathrm{M_{NS}} = 0.71\mathrm{M_\odot}$, appeared to be twice lower than that for white dwarves, $\mathrm{M_{WD}} = 1.44\mathrm{M_\odot}$, calculated earlier by Chandrasekhar (1935). Only twenty years later the nuclear forces were included into consideration by Cameron (1959), yielding the value close to the currently accepted one, $\mathrm{M_{NS}} \sim 2\mathrm{M_\odot}$ (see e.g. Lorimer & Kramer, 2012). For a few decades the topic of collapsed stars remained purely "academic": although some supernova remnants (e.g. the Crab Nebula or Cassiopea A) were known at that time, targeted searches of their possible neutron star residents were not performed.

The progress in physics (especially, particle physics) accumulated by the 1960-s contributed greatly to further investigations of the equation of state (e.g. Salpeter (1960), Ambartsumyan & Saakyan (1960); Zeldovich (1962)). Another subject of

interest was the internal structure of neutron stars, resulting in the prediction of superfluidity in their interior (Migdal, 1960).

Deep theoretical studies of superdense matter went along with discussions on possible observational manifestations of neutron stars. For example, Zeldovich & Guseynov (1966) proposed to inspect "suspicious" spectroscopic binaries, the ones containing a main-sequence star and an unobserved companion. Such companions were surmised to be neutron stars that could be possibly indirectly detected by Doppler shifts of optical spectral lines of the main-sequence star.

The first non-optical glimmer of hope emerged from the models of neutron star cooling (Chiu & Salpeter, 1964; Morton, 1964; Bahcall & Wolf, 1965; Tsuruta & Cameron, 1965) predicting the potential observability of the soft X-ray (thermal) emission from non-magnetic neutron stars. A possibility to prove this hypothesis appeared with the discovery of the first X-ray source located outside the Solar System, Scorpio X-1 (Giacconi et al., 1962). Ironically, in this particular case the X-ray emission had a bit different, non-cooling, origin, nonetheless, also related to neutron stars. As was argued by Shklovsky (1967), the Scorpio X-1 X-ray emission was caused by the accretion of matter from the companion onto a neutron star. However, this correct interpretation did not get support at that time, ten more years passed until it was confirmed by de Freitas Pacheco et al. (1977). A few other X-ray sources, found by 1967, (Friedman et al., 1967) also did not seem to behave like cooling neutron stars[1]. Thus, these first searching attempts were unsuccessful.

Meanwhile, theoretical investigations of neutron star formation, with a focus on magnetic properties, revealed some interesting perspectives. Ginzburg (1964) considered the collapse of a protostar, evolving into a one-solar-mass neutron star, and, assuming magnetic flux conservation, calculated the accurate value for the post-collapse magnetic field strength: $B \sim 10^{12}$G. Further, Ginzburg & Ozernoi (1965) concluded the possible existence of "magnetoturbulent atmospheres around collapsing magnetic protostars". These magnetospheres were thought to be filled with relativistic charged particles emitting electromagnetic waves with frequencies from radio to X-ray. Thus, these authors *de facto* substantiated the key role of non-thermal radiation from neutron stars.

In parallel, Kardashev (1964) developed a model of a rotating neutron star left after the supernova explosion in the Crab Nebula, as well predicting a strong magnetic field. Finally, Pacini (1967) introduced a general model of a neutron star – an oblique rotator with a dipolar magnetic field – and discussed some possible mechanisms and consequencies of the release of magnetic and rotational energy by this rotator.

[1] As turned out later, for the majority of pulsars the luminosity of thermal radiation due to neutron star cooling is under the detection threshold. Thus, solely (prevailing) thermal X-ray emission can be detected only for a few nearest sources forming a subgroup of X-ray dim isolated neutron stars (see e.g. Mereghetti, 2011).

Radio discovery

Despite all the progress and profound predictions made in theory of neutron stars, the first observational evidence of their existence came serendipitously, in the form of the famous "bit of scruff" – a periodical radio signal which appeared on the recordings of Jocelyn Bell (now Prof. Bell-Burnell) who at that time was studying scintillations of compact radio sources in the newly-built Mullard observatory (Bell Burnell, 1977).

However, the signal was not associated with neutron stars immediately after detection. Firstly, it was considered to be man-made radio-frequency interference. Its extraterrestrial origin was established only after detecting the same signal many times in the same part of the sky, at the same sidereal time. Nonetheless, the precise periodicity of 1.3 s, with a pulse duration of about 0.3 s, seemed a bit suspicious, even giving rise to alien-related explanations. Fortunately, before the discovery was announced in 1968 (Hewish et al., 1968), three more objects of apparently the same nature were found by Bell in different regions of the sky, confirming their non-artificial provenance.

Among the possible sources of these periodical signals, further discussed in scientific community, were oscillating white dwarfs and neutrons stars or binary systems orbiting each other and emitting in radio. The discoverers themselves associated the pulsed radiation with the radial pulsations of a white dwarf or a neutron star (Hewish et al., 1968). The subsequent discovery of the short-period Crab pulsar (33 ms) (Staelin & Reifenstein, 1968) and the Vela pulsar (88 ms) (Large et al., 1968) excluded the oscillating white dwarf scenario, since the lowest limit on the periodicity of such pulsations was expected to be much larger, 0.25 s. The observed lack of Doppler shift in frequency ruled out the hypothesis of orbiting binary systems.

Gold (1968a) presented the model where periodical signals from pulsars, finally, found their connection with rotation of neutron stars. Moreover, this model also predicted the slow-down of rotation with time due to the loss of rotational energy in the form of radiation. When this prediction was observationally confirmed for the Crab Pulsar (Richards & Comella, 1969), no space was left for other models and the concept of pulsars as highly magnetised rotating neutron stars settled in astronomy. The theory of orbiting neutron stars found its application with the discovery of the first binary pulsar in 1974 (Hulse & Taylor, 1975). The importance of pulsar discoveries has been marked by two Nobel prizes.

1.1 The very basic pulsar model: theory and observables, magnetosphere and radiation

Half a century has passed since their discovery, but pulsars still posit many questions. The main unsolved mystery dates back to the earliest days of their observations. As became clear already in the late 60-s (Ginzburg et al., 1969), the extremely high pulsar brightness temperatures (10^{26}–10^{31} K) could not have a thermal origin. As soon as pulsar radiation was related to that of a magnetised rotating neutron star, numerous models appeared to explain the generation of radio emission by some coherent non-thermal processes (see a review by Melrose & Yuen, 2016). In these models the key roles

were given to charged particles moving with relativistic speeds in a strong magnetic field. Many efforts have been made to obtain solutions where particles emit in phase and in a strongly pre-determined direction producing sharp energetic beams. The most widely discussed theories considered some form of plasma emission (Ginzburg & Zheleznikov, 1975; Hinata, 1976), curvature radiation (Radhakrishnan, 1969; Komesaroff, 1970; Ruderman & Sutherland, 1975) and maser-like mechanisms (Chiu & Canuto, 1971; Kaplan & Tsytovich, 1973). In course of time the models became more complicated, finding arguments both in favour and against. Despite considerable progress in understanding pulsar electrodynamics (see e.g. Beskin et al., 2013), the consensus on emission mechanism is still not achieved.

However, as it turned out, the question of emission's nature can be left aside for interpreting many observed pulsar properties at a qualitative level. A very basic understanding can already be obtained from the "classical" model proposed by Goldreich & Julian (1969).

Magnetosphere

A highly magnetised rotating neutron star whose magnetic axis is inclined with respect to its rotational axis can be considered as a rotating conducting sphere with a predominantly dipolar magnetic field. The strong magnetic field induces an enormous electric field ($E \sim 10^{11}$V/cm) which tears the charged particles out of the surface and accelerates them to relativistic speeds (with Lorentz factors $\gamma > 10^2$–10^3). These primary particles, in turn, initiate electron-positron pair-creation populating the region near the star with a secondary plasma which co-rotates rigidly with it. The rigid co-rotation is maintained up to a certain distance from the star. At this distance (called the radius of the "light cylinder") the speed of a rotating point becomes luminal:

$$r_c = \frac{Pc}{2\pi}, \tag{1.1}$$

The radius of the "light cylinder" (Eq. 1.1) defines a border between closed and open magnetic field lines, i.e. the border of the *magnetosphere*. The regions of the magnetosphere surrounding the poles of the magnetic axis and restricting a bundle of open field lines comprise the so-called *"polar caps"*. Extremely high strengths of the magnetic fields make particles stream along the field lines since the velocity of gyration is negligible compared to the tangential one. The particles following the "closed field line paths" turn back to be re-captured near the surface whereas the ones travelling along the open field lines leave the magnetosphere from polar caps carrying away the energy in the form of pulsar wind (see e.g. Beskin et al., 1993) and emitting radiation in the direction of their motion.

Generation of radiation takes place as long as the magnitude of the electric-potential drop along the magnetic field lines exceeds some critical value and is sufficient for maintaining the flow of the particles. Due to the transformation of the star's rotational energy into electromagnetic radiation and pulsar wind, its rotation slows down with time (for more details see Section 1.2). As a result, the waning magnetic field cannot

anymore provide conditions necessary for accelerating the primary particles and the emission ceases.

1.2 Pulsar spin evolution, magnetic field strengths and characteristic ages

Observations show that pulsar rotations tend to slow down. The rotational kinetic energy mostly goes on particle acceleration and generation of high-energy emission. The exact mechanism of energy transformation is still debatable, though numerous works (for a detailed review see e.g. Beskin et al., 2015) are devoted to this question.

In general terms, the losses in the rotational kinetic energy (also called the spin-down luminosity) $\dot{E}$ can be written as:

$$\dot{E} = -\frac{\mathrm{d}(I\Omega^2/2)}{\mathrm{d}t} = -I\Omega\dot{\Omega}, \tag{1.2}$$

where I is the pulsar's moment of inertia (with a typically used value of $10^{45}\,\mathrm{g\,cm^2}$), Ω and $\dot{\Omega}$ – the spin frequency and its first derivative.

Historically (see e.g. Gold, 1968b; Goldreich & Julian, 1969; Gunn & Ostriker, 1969; Chiu, 1970), a spinning magnetised neutron star has been considered as an oblique magneto-dipole rotator. A simplistic model of such a star rotating in a vacuum and loosing its rotational energy in the form of magnetic dipole radiation is still commonly used for basic description of some fundamental properties. Following the assumptions of this model, $\dot{E}$ can be also expressed (Gunn & Ostriker, 1969) as:

$$\dot{E} = \frac{2}{3c^3}\,|\vec{\mu_{\mathrm{B}}}|^2\,\Omega^4 \sin^2\alpha, \tag{1.3}$$

$\vec{\mu_{\mathrm{B}}}$ is the magnetic dipole moment, α is the angle between the rotational axis and the direction of $\vec{\mu_{\mathrm{B}}}$ which defines the magnetic axis.

Equating the right-hand sides of Eq. 1.2 and Eq. 1.3 allows derivation of the magnetic field strength at the surface of the rotator:

$$B_{surf} = \sqrt{\frac{3c^3}{8\pi^2}\frac{I P \dot{P}}{R^6 sin^2\alpha}}, \tag{1.4}$$

The majority of known pulsars have $\dot{E}$ lying within 10^{31}–$10^{34}\,\mathrm{erg\,s^{-1}}$, which corresponds to $B_{surf} \sim 10^{12}$–10^{13}G. Very young and energetic ones can demonstrate losses of 10^{38}–$10^{39}\,\mathrm{erg\,s^{-1}}$ (see the ATNF[2] catalogue). Only a small fraction (10^{-4}–10^{-6}) of the total energy losses is converted into radio emission: the radio luminosities are usually of order 10^{26}–$10^{28}\,\mathrm{erg\,s^{-1}}$.

From Eq. 1.2 and Eq. 1.3 one can express $\dot{\Omega}$ as an exponential function of Ω:

$$\dot{\Omega} = -C\Omega^3 \tag{1.5}$$

[2]http://www.atnf.csiro.au/people/pulsar/psrcat/; Manchester et al. (2005)

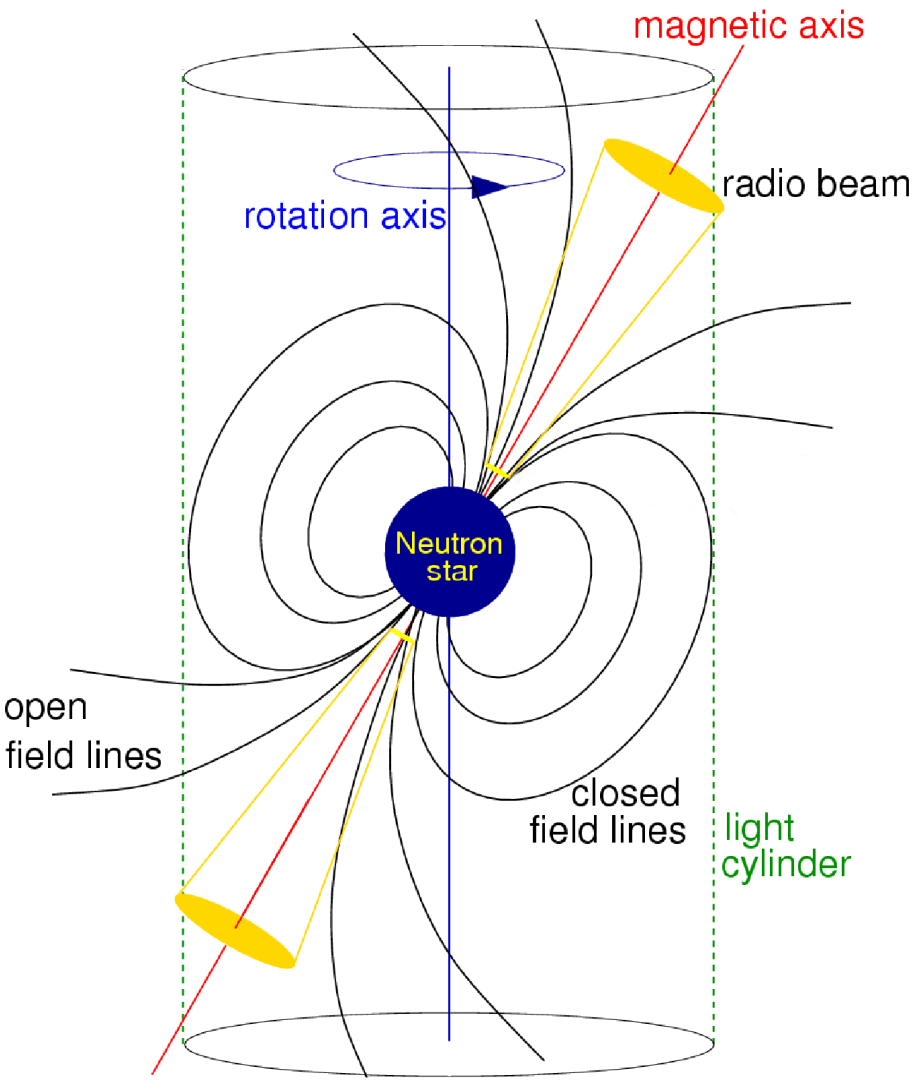

Figure 1.1: The "lighthouse model" of pulsar radiation. The figure is slightly modified from Lorimer & Kramer (2012).

The power of the exponent equals 3 only in the case of pure magnetic dipole braking, assuming vacuum surroundings. This fairly rough "spherical cow in a vacuum" assumption is not (quite) correct since a real pulsar has a magnetosphere whose own fields and currents also affect the rotation. Moreover, some pulsars might show deviations from the "canonical" slow-down behaviour. For example, glitching pulsars (see e.g Haskell & Melatos, 2015) experience transient increases in their rotation rate, glitches, that are thought to be caused by the activity of pulsar interior. Even more non-standard are intermittent pulsars (Kramer et al., 2006a; Lorimer et al., 2012; Camilo et al., 2012; Lyne et al., 2017) who switch between two distinct regimes: radio-loud ("on") and radio-quiet ("off"), with the spin-down rate appearing to be higher in the "on" state than in the "off" state. Thus, a variety of physical processes (sometimes unknown) are involved in pulsar rotational evolution. Accounting for possible contributions from different factors, one can re-write Eq. 1.5 as a general power law:

$$\dot{\Omega} = -C\Omega^n, \tag{1.6}$$

where C is a constant coefficient and n is the so-called *braking index* (also ***assumed*** to be constant).

Differentiating the Eq. 1.6, it is possible to eliminate the constant C and find n.

$$n = \frac{\Omega\ddot{\Omega}}{\dot{\Omega}^2}, \tag{1.7}$$

Practically, it is difficult to measure $\ddot{\Omega}$ and n. Up to 2018, $\ddot{\Omega}$ has been obtained only for a few pulsars providing the values of n ranging from 0.9 ± 0.2 to 2.839 ± 0.001 (see Lyne et al., 2015, and references therein). A recently reported measurement for PSR J1640−4631 by Archibald et al. (2016) gives $n = 3.15 \pm 0.03$.

Having information on braking indices is crucial not only for getting a better insight into the physics of spin-down but also for evaluating pulsar ages. Expressed in terms of the spin period P and its first derivative $\dot{P}$, Eq. 1.6 becomes:

$$\dot{P} = -CP^{2-n}. \tag{1.8}$$

If at the moment of its birth the pulsar had a spin period P_0, then integrating Eq. 1.8, one can obtain the pulsar age:

$$Age = \frac{P}{(n-1)\dot{P}}\left[1 - (\frac{P_0}{P})^{n-1}\right]. \tag{1.9}$$

Since it is hard to measure the exact values of braking indices for the majority of currently known pulsars ($\sim$ 2600 pulsars), their true ages, in most cases, remain unknown. One exception are young ($< 10^4$–10^5 yr) pulsars whose ages can be determined more precisely if it is possible to establish connections with the associated supernova remnants (SNR) and pulsar wind nebulae (PWN) whose ages can be obtained from kinematic measurements (imaging) (see e.g. Crawford et al., 2002; Arzoumanian et al., 2011).

Assuming $n = 3$ and $\frac{P_0}{P} \ll 1$, one can introduce the so-called characteristic age, τ_c:

$$\tau_c = \frac{P}{2\dot{P}}, \tag{1.10}$$

Since both assumptions may not reflect the real situation, τ_c should be considered only as a rough estimate for the order of magnitude of pulsar age in cases when a reliable measurement is not achievable. Calculated for young pulsars, it may give contradictory results, compared to the age estimates provided by SNR/PWN-related measurements.

1.3 Pulse profiles

Though we know a number of pulsars detectable through their single pulses, in most cases pulsars are too weak to hunt them out by a single pulse sunken in the sea of noise. Individual pulses usually do not have exactly the same shape and intensity (see, for example, Fig. 1.2) that is why they cannot be considered as a reliable "carte de visite" for a particular object. A much more robust way is to coherently sum up (fold) hundreds or thousands of pulses. This gives an extremely stable *integrated pulse profile* (different for different observing frequencies), a characteristic which can be used to great advantage in pulsar timing (see Chapter 4).

Pulsars demonstrate a great variety of integrated profiles (the black curves in every upper plot in Fig. 1.3). Among the factors largely influencing the exact profile appearance are the inclination angle α, i.e. the angle between the magnetic $\vec{m}$ and rotational $\vec{\Omega}$ axis, and the impact angle (the viewing angle) β, which is simply the angle between the magnetic axis and our line-of-sight (see Fig. 1.4). These two angles determine the geometry of the cutting region making possible many different configurations of cross-sections, hence, observed profiles. A more rare case is having components separated for $\sim 180^\circ$ from the main pulse, they are called interpulses. One of the explanations for this phenomenon is that the interpulse originates from the beam emitted by the opposite pole of the pulsar seen when the magnetic axis is perpendicular to the rotation axis. Another possibility, first proposed by (Manchester & Lyne, 1977), is the emission of different edges within a large beam from one pole in the case of nearly aligned magnetic and rotation axes.

The morphology of the pulse profile depends significantly on the observing frequency, even the number of the profile components may vary. Across very wide frequency ranges (from tens of MHz to hundreds of GHz[3]) pulses demonstrate a general tendency to be broader at lower frequencies than at higher ones. Most probably, this is a direct consequence of the fact that different-energy emission is produced at different altitudes over the pulsar surface (namely, magnetic poles) and what we see at different frequencies is simply the different-size cuts of the emitting cone (Cordes, 1978). For the

[3] In pulsar astronomy the most commonly used bands – according to the IEEE radar band definition – are: the UHF-band(300 MHz and 1 GHz), L-band (1 to 2 GHz range), S-band (2 to 4 GHz) (see IEEE convention) and C-band (4 to 8 GHz).

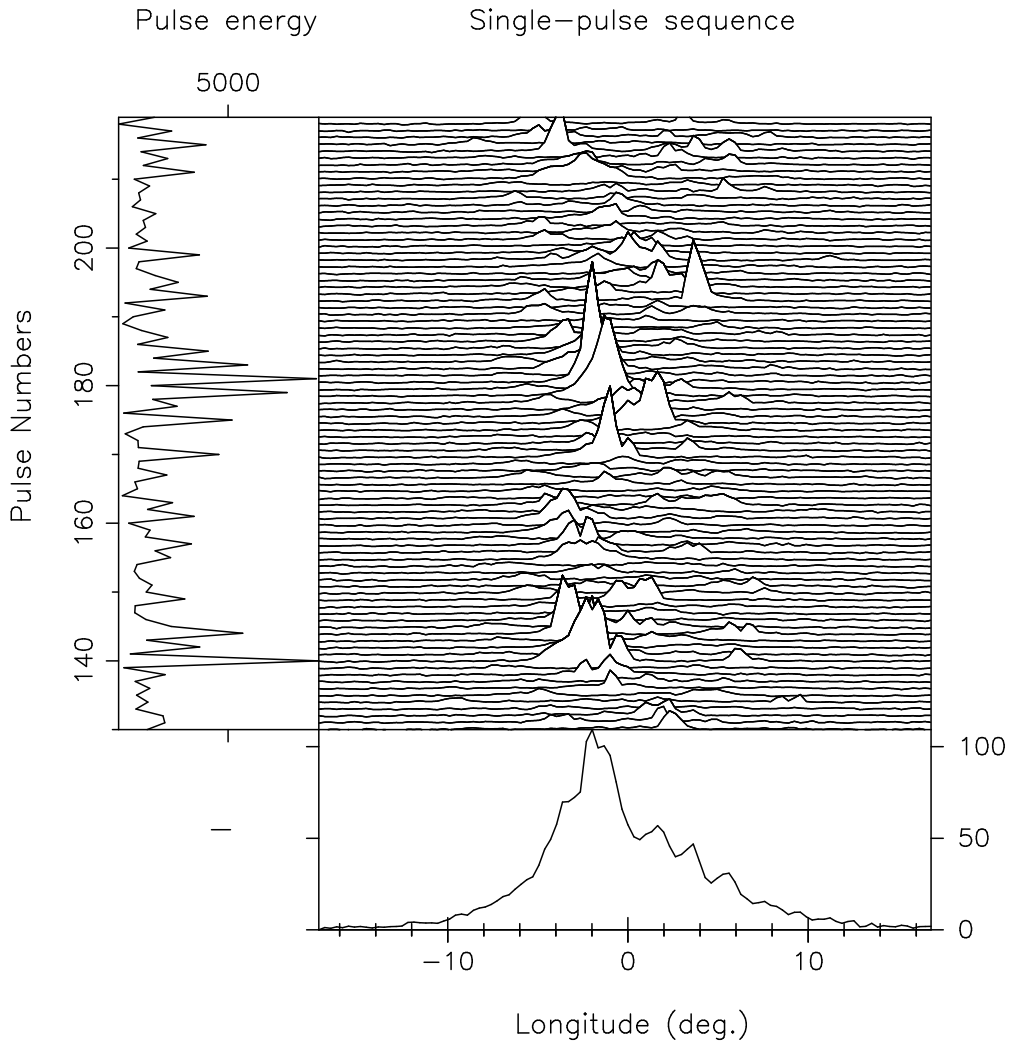

Figure 1.2: A sequence of single pulses from PSR B0943+10 with $P = 1.0977$ s as a function of pulse number and longitude (central panel), together with the integrated pulse profile (bottom panel) and pulse energy as a function of pulse number (left panel). The figure is taken from Deshpande & Rankin (1999).

majority of modern receivers used in pulsar observations, whose bandwidths lie within tens–hundreds of MHz, pulse profiles are assumed to be constant, unless egregious deviations emerge. However, the implementation of new-generation receivers having bandwidths up to a few GHz (see e.g. Liu et al., 2014a) imply the need for taking the frequency-dependent profile variations into account on a regular base.

1.4 Polarisation of pulsar emission

The polarisation properties of radiation received by an observer can be studied by measuring the four Stokes parameters: I, Q, U and V. The most commonly used parameter is the total intensity I. The linearly polarised intensity can be obtained as

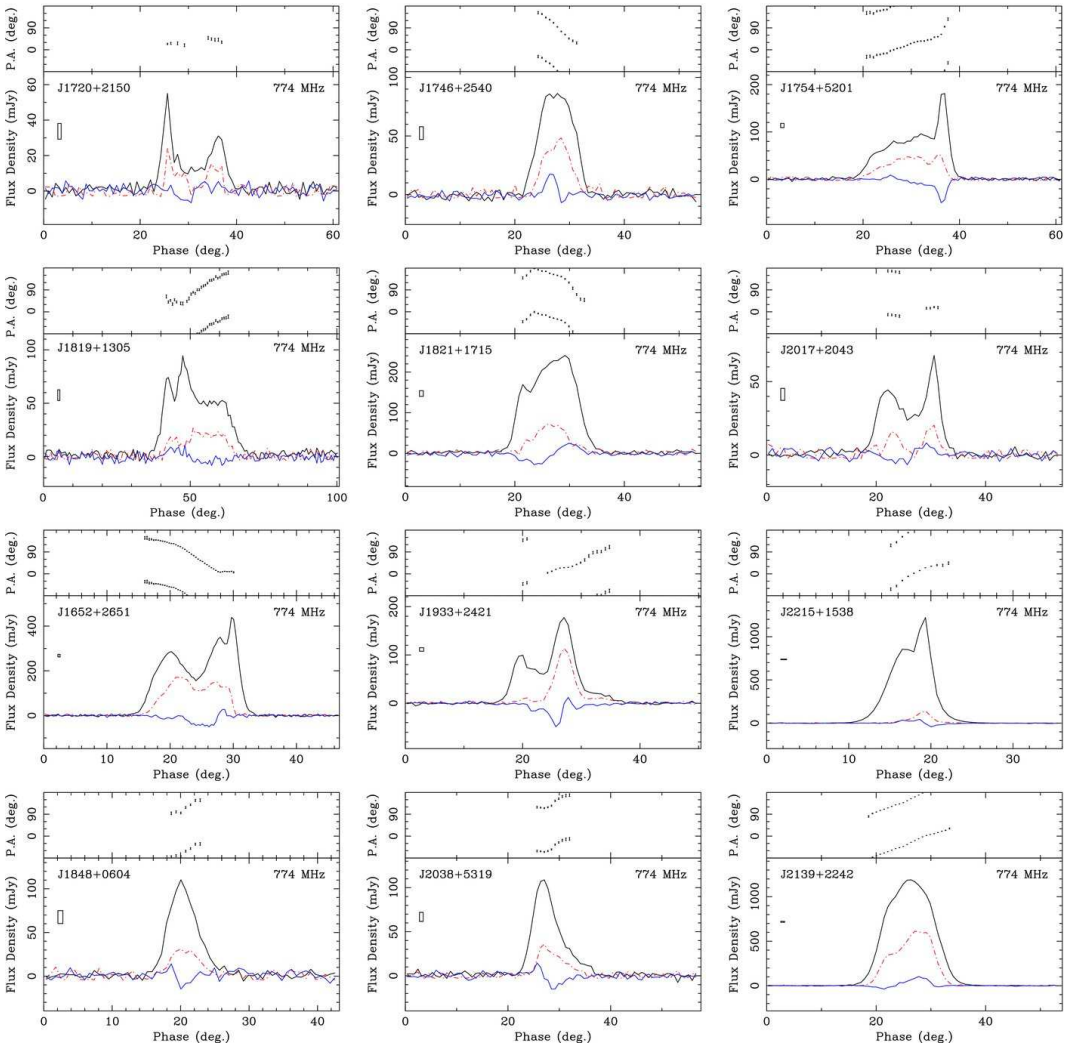

Figure 1.3: In the lower part of each plot we demonstrate the integrated profiles of several pulsars with the total intensity (the black line), the linearly polarised intensity (the red dash-dot-dashed line) and the circularly polarised intensity (the blue line) given. In the upper part, we show the P.A. of the linearly polarised emission vs. pulse phase. The figure is taken from Han et al. (2009).

$L = \sqrt{Q^2 + U^2}$, and V here is the circularly polarised intensity. Most pulsars show a high fraction of linear polarisation, sometimes even up to 100%. The fraction of circular polarisation is lower and, on average, hovers around 10% (see e.g. Lorimer & Kramer, 2012). An example of collected profiles with polarisation are presented in Fig. 1.3.

An important measurable characteristic of the received pulsar radiation is the position angle (PA) of linear polarisation at a given rotational phase: $\psi = 1/2 \arctan(U/Q)$. As can be seen from Fig. 1.3, pulsars often demonstrate a gradual "S"-shaped swing of the on-pulse PA. A very straightforward geometrical interpretation of the ideally

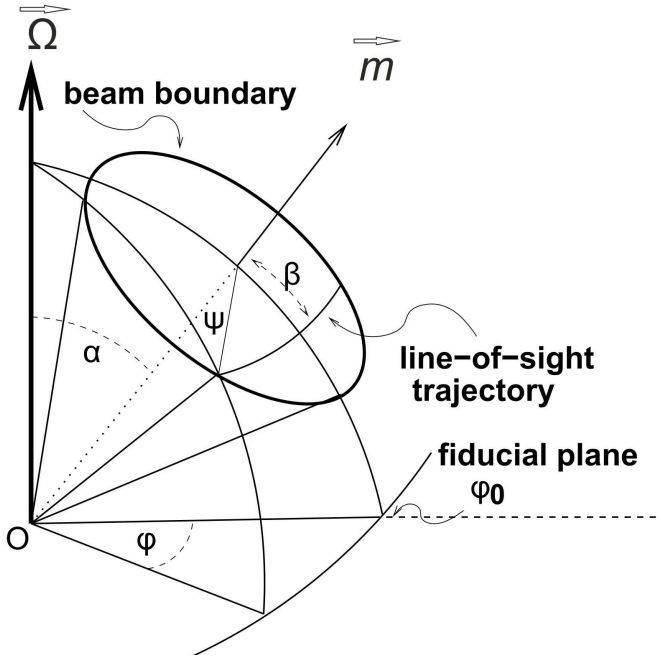

Figure 1.4: Geometry of the pulsar beam as seen by the observer: α is the inclination angle between the magnetic and rotation axis, β is the impact angle between the magnetic axis and the line-of-sight at closest approach, $\vec{\Omega}$ is the rotational axis and $\vec{m}$ is the magnetic axis, ϕ is the rotational phase, ψ is the position angle of linear polarisation. The figure is slightly modified from Johnston et al. (2005).

smooth rotation of the plane of polarisation was first proposed by Radhakrishnan & Cooke (1969) within the so-called "rotating vector model (RVM)". Here the direction of the wave's electrical field vector is determined by the inclination of the plane of a particular magnetic field line that crosses the observer's line-of-sight at the moment of observation. In other words, in the course of pulsar rotation our line-of-sight passes steadily through different magnetic field lines whose planes are inclined at different angles to the fiducial plane drawn through the rotational $\vec{\Omega}$ and magnetic $\vec{m}$ axes (see Fig. 1.4).

This is observed as a gradual change of the instantaneous direction of the encountered magnetic field line when projected onto the observer's picture plane. Then it appears natural to relate the observed smooth change of PA to the rotation of the projection of the magnetic field line, assuming that the instantaneous direction of polarisation is tangential to the magnetic field line at the point of emission.

This simplistic assumption provides an opportunity to study the magnetospheric geometry. Relating the PA measured in the observer's plane with the angle ψ between the (instantaneous) plane of the magnetic field line and the fiducial plane[4] in the

[4]For this one should assume, of course, that the consequences of interaction with the interstellar medium, namely, Faraday rotation of the plane of polarisation (see Section 1.5.3), are corrected for.

pulsar's frame, it is possible to estimate the magnetic inclination angle α and the impact angle β. If ϕ is the rotational phase, then, following the notation of Radhakrishnan & Cooke (1969):

$$\tan(\psi - \psi_0) = \frac{\sin\alpha \sin(\phi - \phi_0)}{\cos\alpha \sin(\alpha + \beta) - \cos(\alpha + \beta) \sin\alpha \cos(\phi - \phi_0)}, \tag{1.11}$$

and ϕ_0 and ψ_0 are the rotational phase and position angle corresponding to the fiducial plane.

Though being not able to explain every particular case of the observed PA variations, the RVM model still finds application (see, for example, Section 4.5.1).

1.5 Effects of propagation of a pulsar signal through the interstellar medium.

The pulse we observe on Earth is not the same as the pulse originally emitted by a pulsar. While travelling through the interstellar medium (ISM), pulsar radiation interacts with the cold ionised plasma. The most prominent consequences of this interaction are dispersion, scattering and scintillation of the pulses.

1.5.1 Dispersion

After leaving pulsar surroundings, a radio wave of frequency f enters the ISM where it further propagates with the group velocity v_g approximated as (see e.g. Chiu, 1970):

$$v_\mathrm{g} \approx c \left(1 - \left(\frac{f_\mathrm{p}}{f}\right)^2\right), \tag{1.12}$$

where c is the speed of light in a vacuum and f_p is the plasma frequency – a low-frequency cut-off for signal propagation in a given medium which determines the refractive properties of this medium and depends on the density of free electrons n_e in it[5]:

$$f_\mathrm{p} = \sqrt{\frac{e^2\, n_\mathrm{e}}{\pi\, m_\mathrm{e}}} \simeq 8.97\,\mathrm{kHz} \left(\frac{\mathrm{n_e}}{\mathrm{cm^{-3}}}\right)^{0.5}. \tag{1.13}$$

Then, as follows from Eg. 1.12, waves with lower frequencies have lower velocities. This means that they arrive to the observer later than the ones with higher frequencies. Since pulsar radiation is broadband, this fact has a great observational impact.

The delay Δt (in ms) between the arrival times of pulses at frequencies f_1 and f_2 (in MHz) can be written as (see e.g Lorimer & Kramer, 2012):

$$\Delta t \approx 4.15 \cdot 10^6 \left({f_1}^{-2} - {f_2}^{-2}\right) \cdot \mathrm{DM}, \tag{1.14}$$

[5] A typically taken value for the ISM's n_e is 0.03 cm^{-3} (Cordes & Lazio, 2002), this gives the plasma frequency of $\sim$ 1.5 kHz. As can be seen, f_p is much lower than the working frequencies of antennas used in pulsar observations.

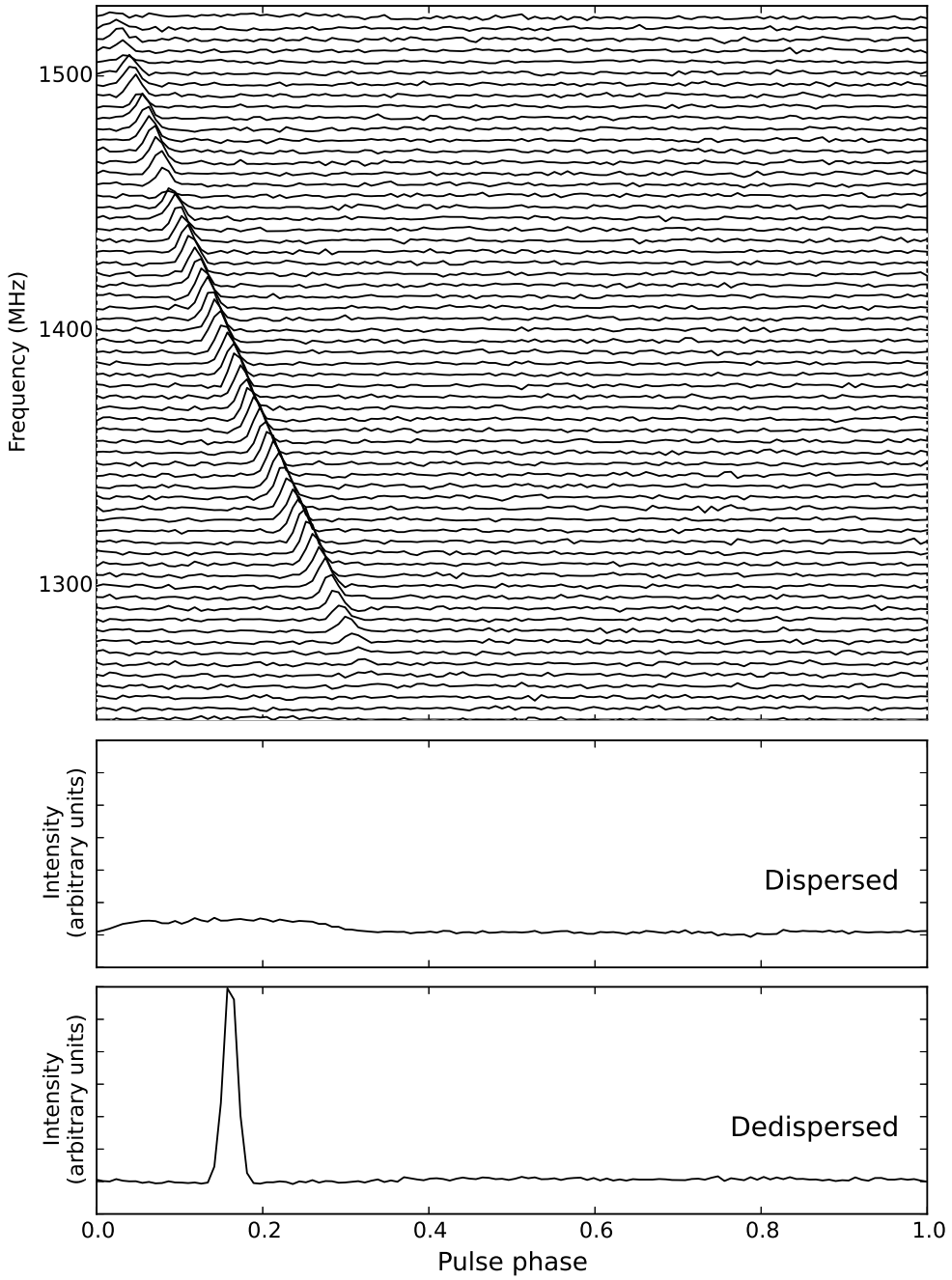

Figure 1.5: An observation of pulse dispersive smearing in PSR J1903+0135 (P = 0.7293 s and DM = 245.2 pc cm^{-3}). The top panel shows frequency vs. phase, with the central frequency of 1360 MHz and the frequency scale represented by 64 channels. The middle panel gives the smeared integrated profile obtained by direct summing of delayed pulses in all frequency channels. The bottom panel corresponds to the dedispersed integrated pulse profile. From data taken for the HTRU-North survey (see Chapter 3).

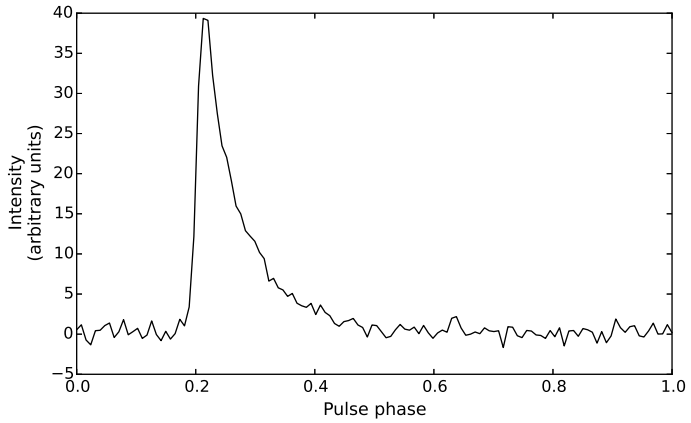

Figure 1.6: The integrated pulse profile of a high-DM pulsar PSR J1818−1422 ($P = 0.2915\,\mathrm{s}$, $\mathrm{DM} = 622.0\,\mathrm{pc\,cm^{-3}}$) showing an exponential scattering tail. From the data taken for the HTRU-North survey (see Chapter 3) at 1360 MHz.

where DM is the *dispersion measure*, the integrated electron column density along the line of sight which depends on the distance d to the source as:

$$\mathrm{DM} = \int_0^d n_\mathrm{e} dl. \tag{1.15}$$

As follows from Eq. 1.15, if the concentration of free electrons n_e in the direction of a given pulsar is known, then a measurement of Δt and, hence, DM provides an estimate of the distance to this pulsar.

If f_1 and f_2 are the upper and the lower edges of the observing band of a wideband receiver[6], then the delay accumulated between these frequencies may exceed the duration of the pulse, resulting in a noticeable reduction of S/N ratio. A natural solution to this problem is to divide the bandwidth into smaller channels with an acceptable intra-channel smearing, so that the pulses are not significantly dispersed within a single channel. The criteria of acceptability in this case are determined by the choice of the central frequency and the characteristics of possible target sources (period and DM), as well as by available technological facilities.

Fig. 1.5 provides an example observation of a pulsar signal where the pulses in individual frequency channels are clearly resolved. Without any correction applied, the pulses look misaligned and the resultant pulse profile obtained by integrating over the bandwidth is still dispersed. However, it is possible to restore the signal by compensating for the delays at every consecutive frequency. This procedure is called *dedispersion* (for more details see Section 2.2.2).

1.5.2 Scattering and scintillation

The ISM between the pulsar and the Earth is non-homogeneous. Irregularities in the turbulent plasma encountered by the signal cause multiple reflections (scattering), deviating the photons' path from the line-of-sight. Therefore, photons that were emitted at one moment in the pulsar's frame reach the observer at different moments as the distances they have travelled are different. These arrival delays produce specific distortions of the pulse shape. If we assume that all the irregularities are concentrated in a thin screen located centrally between the pulsar and the observer[7] and denote the delay in the arrival time of the deflected wave relative to the arrival time of the one that followed a direct path as δt, then the intensity can be approximated by (see e.g. Lyne & Graham-Smith, 2012):

$$I(t) \propto e^{-\delta t/t_s}, \tag{1.16}$$

with the scattering timescale, t_s, depending both on the distance and observing frequency as, $t_s \propto d^2/f^4$ (Scheuer, 1968; Lang, 1971; Romani et al., 1986)[8].

The one-sided exponential law in Eq. 1.16 determines the shape of the distorted signal: the originally sharp pulse acquires a so-called "exponential scattering tail" (see Fig. 1.6). Unlike dispersive smearing, this detrimental effect is not typically corrected for. Especially noticeable at low frequencies, scattering-caused broadening of the pulse wanes when moving to higher frequencies. However, the pulsar signal generally becomes fainter at higher frequencies, as determined by a negative index of the power-law flux density spectrum. For this reason, the choice of an optimal observing frequency should be governed by a compromise between obtaining a sharp profile and having a sufficient flux. Moreover, since the scattering effect grows with distance, it becomes the limiting factor for detectability of distant pulsars because of drastic reduction in signal-to noise ratio (S/N).

Another effect caused by the turbulent nature of the interstellar medium is scintillation. Density fluctuations disturb the wavefront of a pulsar signal producing waves with various phase shifts. At the observer's plane, these waves may superpose forming a spatial interference pattern, unique for every frequency. Since the observer traverses the interferential maxima and minima due to the motion of the Earth relative to the pulsar and the turbulent medium, the signal's intensity appears to vary with time. Scintillations are mostly observed for nearby pulsars (DM $< 100\,\mathrm{pc\,cm^{-3}}$), since both its timescale and bandwidth distance Fig. 1.7 shows an example of a scintillating pulsar.

1.5.3 Faraday rotation

Travelling through the interstellar medium influences the initial polarisation properties of the pulsar signal. Due to its birefringent nature, the ionised interstellar plasma

[6] In pulsar (radio) astronomy the bandwidths of a few hundreds MHz are generally considered wide.

[7] This is the basic assumption of the so-called *thin-screen model* (Scheuer, 1968).

[8] Though this relation is sufficient for describing "the scattering tails" of low-DM pulsars (DM $< 100\,\mathrm{pc\,cm^{-3}}$), it may be no longer appropriate with the increase of DM (Löhmer et al., 2001, 2004; Krishnakumar et al., 2015).

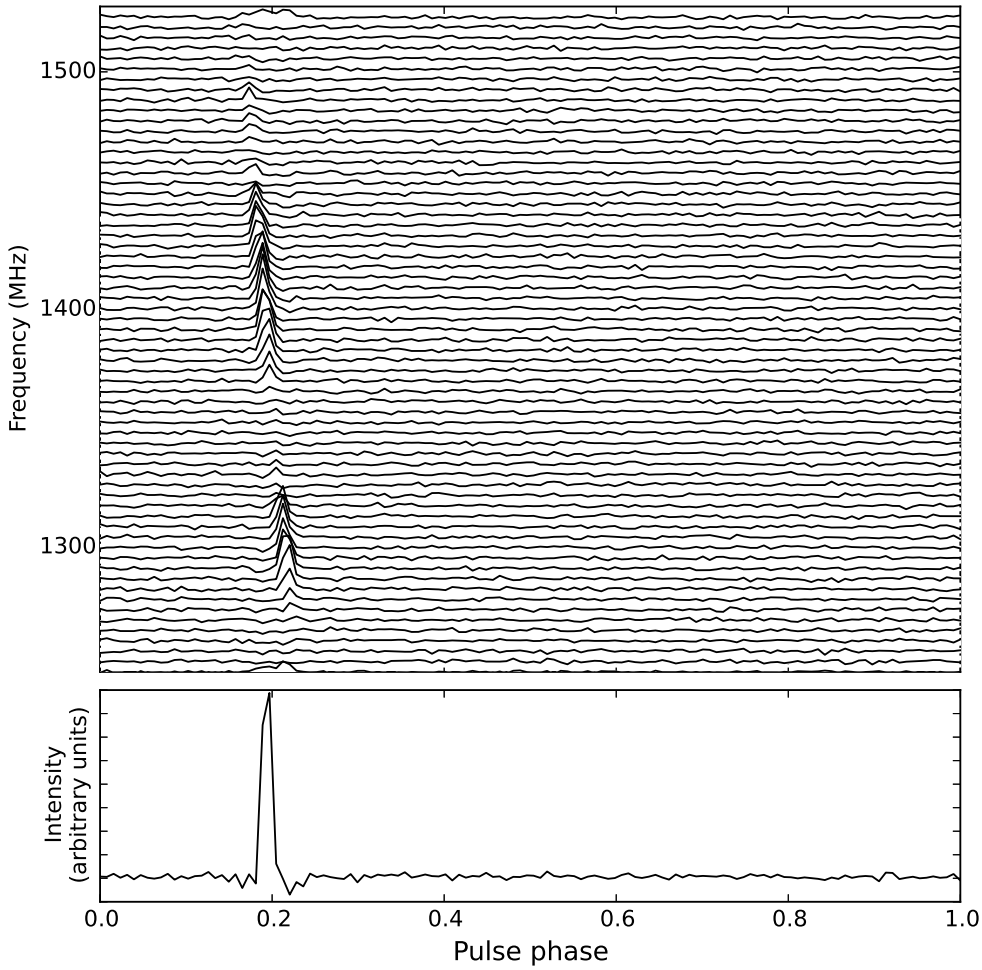

Figure 1.7: Scintillation demonstrated by PSR J1955+5059 ($P = 0.5189\,\mathrm{s}$, DM = $31.9\,\mathrm{pc\,cm^{-3}}$). Two scintles can be seen centred at 1.3 and 1.4 GHz. From the data taken for the HTRU-North survey (see Chapter 3) at 1360 MHz.

introduces a relative shift between the phases of the right and left circularly polarised waves. As a consequence, the plane of polarisation of a linearly polarised wave, that can be considered a superposition of left and right circularly polarised waves, experiences rotation as it propagates in the magnetic field of the Galaxy.

The angle of rotation Θ (so-called *Faraday rotation*) varies as a function of frequency (wavelength) and depends on the strength of the Galactic magnetic field along the line of sight $B_{||}$:

$$\Theta = \mathrm{RM}\,\lambda^2 = 0.81\,\lambda^2 \int_0^{\mathrm{d}} \mathrm{n_e B_{||} dl}, \tag{1.17}$$

where RM is the rotation measure, λ is the wavelength in meters, n_e is in cm^{-3}, $B_{||}$ is in μG and the length is in parsecs. RM can be obtained by measuring the position angle at different frequencies. If the distance d is known, for example, from parallax or DM measurement, then measuring RM provides a possibility to estimate the average $B_{||}$.

To study the signal's intrinsic polarisation state, it is necessary to compensate for Faraday rotation by applying the corresponding position angle correction determined by RM within every frequency channel.

1.6 The Pulsar Zoo

The currently known Galactic pulsar population comprises over 2600 pulsars[9] having different observational characteristics. The basic ones, such as the spin period and its derivative, vary greatly within the whole sample. For example, the observed spin periods range from 1.396 ms for PSR J1748−2446 (Hessels et al., 2006) to 23.5 s for PSR J0250+5854 (Tan et al., 2018). The order of period derivatives mostly goes from 10^{-13} to 10^{-23} (s s^{-1}) (see the `ATNF pulsar catalogue`). The wide spread of P and $\dot{P}$ values corresponds to (as discussed in Section 1.2) the variety of magnetic field strengths and characteristic ages. However, the seemingly chaotic distribution of pulsar parameters looks more ordered if P and $\dot{P}$ are considered together in the form of the "$P - \dot{P}$ diagram" (see Fig. 1.8). The plot clearly reveals clustering of objects with similar characteristics, thus, providing a way for identifying a few distinct populations of the diverse pulsar menagerie. Moreover, the diagram allows tracing the evolutionary links between the subgroups.

The majority of pulsars, called *normal* or, sometimes, *canonical*[10], have, in general, spin periods from hundreds of millisesonds to a few seconds. The shortest periods ($P \leqslant 30$ ms)[11] are observed for *millisecond* (MSP) pulsars, while the longest ones are usually associated with magnetars.

1.6.1 Normal pulsars

The subclass of normal pulsars is mostly presented by isolated neutron stars. They demonstrate a large spread of spin periods (marked in black in Fig. 1.8), occupying the central part of the $P - \dot{P}$ plane. Young normal pulsars ($< 10^4$ yr) which are observed to have fairly small values of P (tens of milliseconds) together with a high $\dot{P}$ are encamped at the top left corner of the diagram. For some of them it is possible to find associations with nearby SNRs and obtain reliable age estimates. Over the course of their evolution (hundreds of thousands of years) young pulsars "roll down" to the "main island" from where they move to the bottom-right part of the diagram as

[9] http://www.atnf.csiro.au/people/pulsar/psrcat/; Manchester et al. (2005)

[10] further in this thesis we will use these terms interchangeably with the same meaning

[11] The upper limit for period values attributed to MSPs varies slightly in the literature. The value presented in this thesis ($\sim$ 30ms) is used, for example, in Lyne & Graham-Smith (2012).

[12] http://www.atnf.csiro.au/people/pulsar/psrcat/

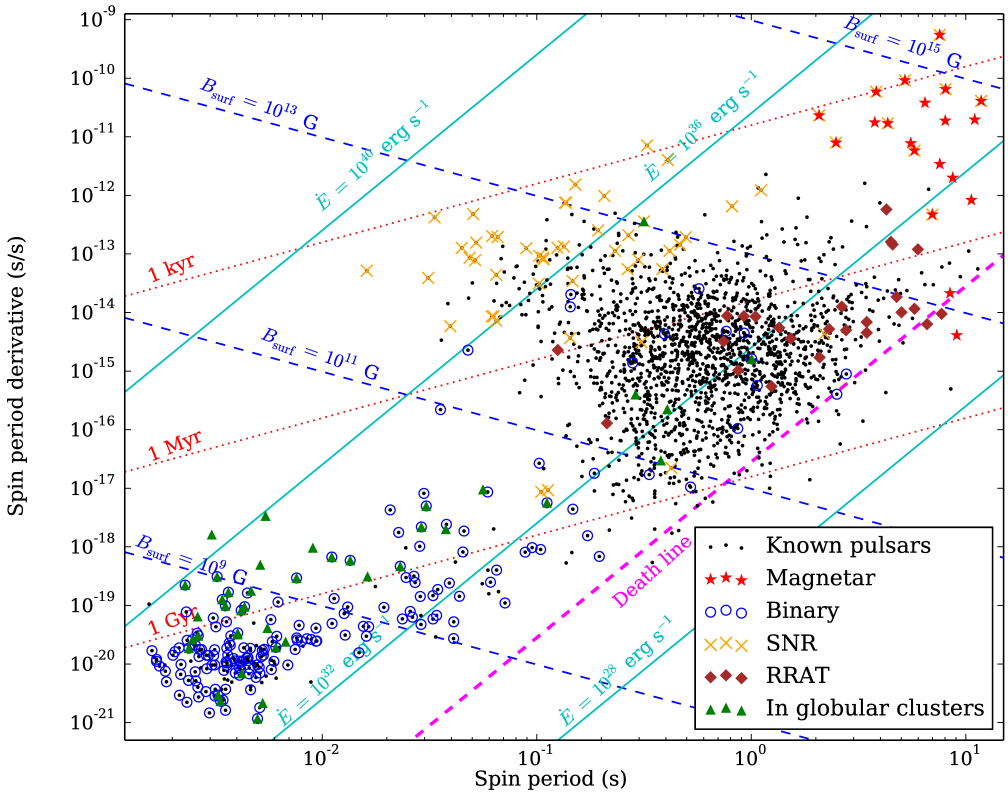

Figure 1.8: The $P - \dot{P}$ diagram for the known pulsar population with measured $\dot{P}$ (the data are taken from the ATNF[12]catalogue). The lines of constant surface magnetic field strength B_{surf}, spin-down-luminosity $\dot{E}$ and characteristic age are plotted in dashed-blue, cyan and dotted-red correspondingly. The equation $\frac{B}{P^2} = 1.7 \times 10^{11}\,\mathrm{G\,s^{-2}}$ for the death line is taken from Bhattacharya et al. (1992).

they slow down. At this stage their magnetic field strengths decrease and the ability to accelerate particles to ultra-relativistic speeds and produce radio emission wanes. After a few million years normal pulsars reach the "death line"[13](see Fig. 1.8).

1.6.2 Recycled pulsars

However, for some old neutron stars it is possible to come back to life. The necessary condition for re-juvenating is having a binary companion in a suitable orbit. A common scenario is as follows. In a system of two main-sequence stars the more massive one

[13]There exist different equations for death lines or even boundaries of the "death valley" whose exact form depends on the assumptions on the dominant radiation mechanism and the magnitude and structure of the magnetic field (e.g. Chen & Ruderman, 1993; Arons, 1998; Medin & Lai, 2007), thus, finishing their radio-detectable life.

evolves first. If its initial mass lies in the range 8–20 $M_\odot$ (see e.g. van den Heuvel, 1989), then, after exhausting the nuclear fusion supplies, the primary undergoes a supernova explosion and forms a neutron star. If the system remains bound after this energetic event, then its further evolution depends on the mass of the companion. At the same time the neutron star passes through a typical pulsar routine of slowing down as described above. When the companion expands enough to overflow its Roche lobe, the dynamic interaction between the two inhabitants of the system initiates the process of accretion of matter and angular momentum from the giant onto the neutron star (see e .g. Phinney & Kulkarni, 1994). During the accretion phase, the latter becomes spun-up to short periods (recycled), obeying the conservation of angular momentum and energy. The flowing plasma becomes heated by friction and interaction with the neutron star's surface and, thus, produces high-energy emission[14]. During this phase the system is observed as an X-ray binary, with no radio emission. Then comes the turn for the second star to reach the end-point of its evolution. The possible outcome depends on the initial mass of the companion (see Chapter 4.2) and can be either a white dwarf or a neutron star (or the companion even can ablated by the pulsar and become a "black widow" – King et al. (see e.g. 2005)). The initial conditions (not only the masses but also the orbital period) affect the resultant spin period and mass of the recycled pulsar (Tauris & Savonije, 1999; Tauris et al., 2000), as well as the orbital period of the evolved binary. After accretion ceases, no more flowing material prevents the radio emission from being observed.

Recycled pulsars are often observed as MSPs. MSPs have small period derivatives (the bottom left of Fig. 1.8) which results in extremely high rotational stability. As can be seen from the "$P - \dot{P}$ diagram", millisecond pulsars tend to have surface magnetic field strengths of 10^8–10^9 G, i.e. lower than that of normal pulsars. The exact mechanism of reduction of the magnetic field during the accretion phase is not clear. However, one of the plausible explanations can be quenching of the field by accreting matter (see e.g. Bhattacharya, 1995; Istomin & Semerikov, 2016).

A fraction of $\sim$ 20% of all known MSPs are isolated. They are believed to be formed in high-mass binaries where the companion also evolved into a neutron star but the binary itself has been disrupted during the second supernova explosion.

1.6.3 Magnetars

The upper right of the "$P - \dot{P}$ diagram" is inhabited by magnetars, young (10^3–10^5 years) isolated neutron stars posessing unusually strong surface magnetic fields (10^{14}–10^{15} G). They are characterized by rapid slow down, relatively long spin periods (P = 2–12 (11.788) s) and high luminosities in some cases exceeding the values derived from the spin-down energy loss (as stated by Eq. 1.3) by several orders (up to 3) of magnitude. Though some magnetars[15] can be observed in radio, the majority of the

[14] This is *accretion-powered* emission.

[15] For a long time since the first detection in 1979 magnetars were observed only at X-rays and γ-rays until transient pulsed radio emission had been received from the X-ray pulsar XTE J1810−197 in 2006 (Camilo et al., 2006). Currently, according to the McGill Online Magnetar Catalog

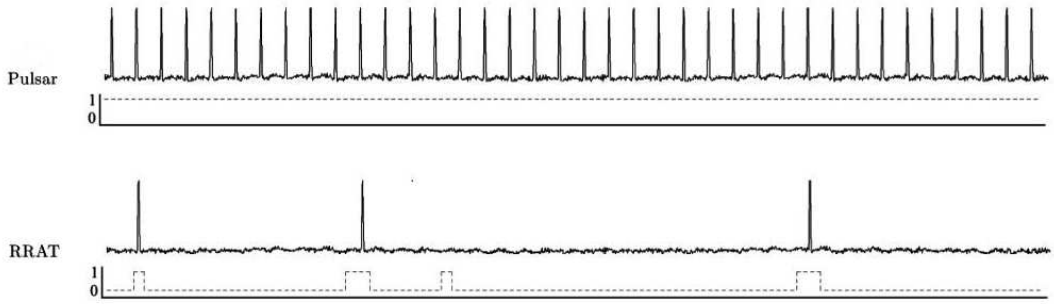

Figure 1.9: The comparison between the observed emission patterns for "canonical" pulsars and RRATs. The figure is a slightly modified version of Fig.6 from Burke-Spolaor & Bailes (2010).

population are active at X-ray and γ-ray wavelengths. This high-energy emission is believed to originate from the magnetic field decay (Duncan & Thompson, 1992). Apart from emitting regular pulses, magnetars might also exhibit occasional short- (~ 0.1 s) or long-lasting (~ 100 s) radio/X-ray/γ-ray outbursts and periods of no emission.

1.6.4 Mavericks: rotating radio transients

Another class of neutron stars are rotating radio transients (RRATs). These objects are detected by searching for their sporadic single pulses (see Fig. 1.9) rather than by checking the data for periodic signals, as it is done for the majority of know pulsars (see Chapter 2). The pulses usually last up to tens of milliseconds and are received on timescales from minutes to hours. Combining these pulses allows inferring the underlying periodicity. Since the discovery of the first RRAT in 2006 (McLaughlin et al., 2006), around 100 other objects of this type have been added to the population (see e.g. Karako-Argaman et al., 2015; Burke-Spolaor et al., 2011). The currently known RRATs have periods lying in the range of hundreds of milliseconds to 7.7 s (see Fig. 1.8)[16], relatively high spin-down rates, compared to that of canonical pulsars, 10^{-15}–$10^{-13}\,\mathrm{s\,s^{-1}}$, and DMs consistent with a Galactic contribution.

At present, it is unclear what causes the irregularity in RRAT emission and how they are related to the rest of the neutron star population. For example, (Zhang et al., 2007) considers RRATs to be old pulsars approaching the "death valley" and exhibiting sporadic turn-offs. Another explanation (Weltevrede et al., 2006) suggests that these are (distant) faint pulsars demonstrating a high pulse-to-pulse variability. It can be

(http://www.physics.mcgill.ca/ pulsar/magnetar/main.html) (Olausen & Kaspi, 2014), out of 29 known magnetars, only three other objects of this type demonstrated radio emission, these are: 1E 1547.0−5408 (Camilo et al., 2007) PSR J1622−49 (Levin et al., 2010) and the Galactic Centre magnetar SGR J1745−2900 (see e.g. Eatough R. P. et al., 2013).

[16]Nevertheless, the real distribution of spin periods can be wider, with more representatives from the millisecond edge. The currently observed lack of millisecond RRATs can simply be a manifestation of selection effects at work: it is more difficult to establish the periodicity for shorter periods.

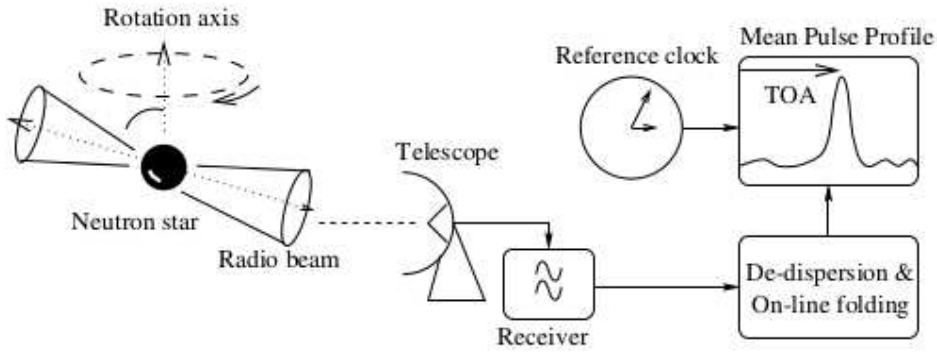

Figure 1.10: An illustration of how timing observations are performed. The image is taken from Lorimer (2005).

also possible that RRATs are related to nulling[17] pulsars (Burke-Spolaor et al., 2011) (with a nulling fraction of $> 99\%$ – see also Fig. 1.9) or originate from magnetars on the "$P - \dot{P}$ diagram" (Lyne et al., 2009). However, only with more new discoveries these alternatives can be confirmed or ruled out.

1.7 Pulsar timing

Once a new pulsar is discovered, only some basic parameters such as spin period and DM are available. Most of the further information can be obtained in the course of long-term timing observations. The phrase "pulsar timing" refers to precise measurement of the times of arrival (TOAs) of pulses at a given observatory on Earth. Many factors such as, for example, pulsar slow-down, interaction with the interstellar medium, different kinds of relative motions (pulsar proper motion, orbital motion of the Earth) and especially the presence of a companion greatly affect the observed temporal behaviour of the strictly periodic pulse train emitted by the pulsar. By incorporating their contributions into a *phase-connected timing model*, it is possible (to some level of precision) to predict when every single pulse corresponding to every single cycle of pulsar rotation should be received at a telescope. Initially a very simple model, based only on a few primarily available parameters, is used. This can further be fit by measuring the difference between the predicted and the observed times of arrival ("timing residuals") and iterating model solutions (with including more parameters) until minimal residuals (in the least-square sense) are reached.

The timing model is based on a formula which relates the pulse's time of arrival at the telescope t_{obs} and the time of emission of the same pulse by the pulsar T.

In the case of isolated pulsars the timing formula (Taylor, 1992):

$$T = t_{obs} + \Delta_C - D/f_b^2 + \Delta_{R\odot}(\alpha, \delta, \mu_\alpha, \mu_\delta, \pi) + \Delta_{E\odot} + \Delta_{S\odot}(\alpha, \delta) \qquad (1.18)$$

[17] The effect of *nulling* (e.g. Backer, 1970; Wang et al., 2007) is characterized by cessation of emission for a few cycles followed by further temporary resumption. The nulling fraction is determined by the ratio of on- and off-cycles.

needs to account for the following delay contributions: Δ_C is the delay introduced by the difference between the specific observatory's and the terrestrial time standards, D/f_b^2 is the dispersive delay caused by the interstellar medium (and depending on the observing frequency and DM), $\Delta_{R\odot}$ is the Roemer delay arising from variations of the signal's geometrical path through the Solar System and depending on the position (α, δ), proper motion (μ_α, μ_δ) and parallax (π) of the pulsar, $\Delta_{E\odot}$ is the Einstein delay accounting for the time dilation and gravitational redshift introduced by the Solar System bodies (Fairhead & Bretagnon, 1990) and $\Delta_{S\odot}$ is the Shapiro delay caused by relativistic effects (time dilation and gravitational redshift) in the gravitational field of the Sun (Shapiro, 1964).

For binary pulsars the effects caused by the presence of a companion must be taken into account. Thus, the timing formula should be modified to include the corresponding "binary" delays: (the Roemer delay Δ_R, the Einstein delay Δ_E and the Shapiro delay Δ_S):

$$T_{binary} = t_{obs} + \Delta_C - D/f^2 + \Delta_{R\odot} + \Delta_{E\odot} + \Delta_{S\odot} + \Delta_R + \Delta_E + \Delta_S \,. \tag{1.19}$$

The largest contribution comes from the Roemer delay. Caused by the pulsar's orbital motion, it can expressed through five Keplerian parameters:

1) the orbital period P_b,

2) the time of periastron passage T_0,

3) the projection of the semi-major axis a_1 on our line-of-sight $x = (a_1/c)\sin i$, where i is the orbital inclination,

4) the eccentricity e,

5) the longitude of periastron ω which can be easily measured within a short time (the exact timescale depends on the orbital period and eccentricity) for most of the binaries.

The Einstein and Shapiro delays' contributions in most cases are less prominent as they manifest the deviations from the purely Keplerian motion due to the relativistic effects in the binary. The timescale for clearly identifying these contributions depends on the "relativicity" of a particular system which can be described by a set of *post-Keplerian* (PK) parameters:

1) the rate of periastron advance $\dot{\omega}$,

2) the orbital period decay $\dot{P}_b$,

3) the Einstein delay γ,

4) the Shapiro delay terms, r (range) and s (shape).

In Damour & Deruelle (1985) it was shown that for any given theory of gravity the post-Keplerian (PK) parameters can be related to the Keplerian parameters and the pulsar and companion masses. The particular form of the equations differs for different theories. In the case of general relativity (GR) Damour & Deruelle (1986) derived:

$$\dot{\omega} = 3(P_b/2\pi)^{-5/3}(T_\odot M)^{2/3}(1-e^2)^{-1} \tag{1.20}$$

$$\dot{P}_b = -\frac{192\pi}{5}\left(\frac{P_b}{2\pi}\right)^{-5/3}\left(1+\frac{73}{24}e^2+\frac{37}{96}e^4\right)(1-e^2)^{-7/2}\, T_\odot^{5/3}\, M_p M_c M^{-1/3}, \tag{1.21}$$

$$\gamma = e(P_b/2\pi)^{1/3} T_\odot^{2/3}\, M^{-4/3}\, M_c(M_p + 2M_c). \tag{1.22}$$

$$r = T_\odot M_c \tag{1.23}$$

$$s \equiv \sin i = (a_1/c)\sin i \left(\frac{P_b}{2\pi}\right)^{-2/3} T_\odot^{-1/3} M^{2/3} M_c^{-1} \tag{1.24}$$

Here $T_\odot \equiv GM_\odot/c^3 = 4.925490947\mu$s, G is the Gravitational Constant, $M_\odot$ is the mass of the Sun, $M = M_p + M_c$, the sum of the pulsar mass M_p and the companion mass M_c (in units of solar mass).

M_p and M_c are related to each other and to the Keplerian parameters through the mass function (Lorimer & Kramer, 2012):

$$f(M_p, M_c) = \frac{(M_c \sin i)^3}{(M_p + M_c)^2} = \frac{4\pi^2}{T_\odot}\frac{x^3}{P_b^2}, \tag{1.25}$$

This implies that, if two PK parameters are precisely measurable, then, together with the mass function, they give a system of three equations with three unknowns. Solving this system yields the masses of the pulsar and the companion. With every subsequent parameter measured, the system becomes overdetermined opening a possibility for testing the convergence (self-consistency) of the theory.

1.8 Pulsar science

Pulsar science encompasses a wide variety of topics. Indeed, to answer the handful of questions which arise, for example, when studying pulsar evolution, emission processes or internal structure, it is necessary to employ various branches of physics and astrophysics. The latter, in turn, can themselves benefit from this exploitation gaining access to a fantastic space laboratory significantly dissimilar to the terrestrial ones. Such a laboratory provides unique opportunities for testing physical theories that cannot be examined under other conditions. The continued progress in both pulsar searching and timing enlarges the possibilities for multi-faceted investigations. To get a better insight, below we briefly list some applications and forefront fields of research.

1.8.1 Exploring gravity

Testing general relativity

Neutron star binaries dwell in conditions where the relativistic effects become dominant. Thus, a number of gravity tests can be performed, depending on the nature, hence, mass of the companion. Strong gravitational fields produced by nearly equally massive components of double neutron star (DNS) binaries make them a perfect tool for testing general relativity (GR) in the strong-field regime and putting constraints on alternative theories of gravity (see e.g. Wex, 2014). For example, the first binary pulsar B1913+16 ("the Hulse-Taylor pulsar", Hulse & Taylor, 1975)), appeared to be a milestone in confirming predictions of GR. The precise measurement of Post-Keplerian

(PK) parameters (see Section 1.7) for this DNS system resulted in the first high-precision measurements of the component masses (Taylor et al., 1979). The ensuing tracing of the orbital decay, as well predicted by GR, provided the first Nobel-Prize-winning evidence for the existence of gravitational waves. The unique double pulsar system PSR J0737−3039, with both neutron stars periodically beaming towards us in radio, further contributed to gravity experiments. For this DNS, five PK parameters and the neutron star mass ratio have been measured, resulting in four independent tests of GR where the theory's correctness has been demonstrated at the 0.05% level (Kramer et al., 2006b). With all the great expectations put on the DNS population, currently numbering at 16 systems[18], it is necessary to mention the recently discovered highly-eccentric ($e = 0.6$) DNS system PSR J1757−1854 (Cameron et al., 2018). Named "the most accelerated binary", this system has already (after 1.6 years of timing) provided precise measurements of five PK parameters with three successful tests of GR.

The systems of pulsar-white dwarf (WD) binaries found their application in probing alternative (e.g. tensor-scalar) theories of gravity or possible violations of the strong equivalence principle since the predicted effects are determined by the difference in gravitational self-energy (see e.g. Perrodin & Sesana, 2017). The discovery of a black hole–pulsar binary ("the Holy Grail" of pulsar astronomy) could open great opportunities for performing even more stringent tests of general relativity (Damour & Esposito-Farèse, 1998; Liu et al., 2014b).

Pulsar timing arrays (PTAs)

A simultaneous high-precision timing of multiple MSPs spread across the sky, comprising a so-called "pulsar timing array" (PTA), can be used to search for the low frequency ($\sim 10^{-7}$–10^{-9} Hz) gravitational waves (GWs) that comprise the stochastic GW background. GW signals cause correlations in the timing residuals of pulsars. Since these signals are very weak, the timing precision of the order of ~ 100 ns is required for an MSP to be included in a PTA. Bright, stable, short-period pulsars having sharp profiles with fine structure (narrow features)[19] are the best candidates for this purpose. At present, around 50 pulsars are periodically observed within the International Pulsar Timing Array (IPTA)[20] project (Verbiest et al., 2016). Expanding the current set with more MSPs discoveries (such as the ones described in Chapters 4 and 5), whose characteristics satisfy the aforementioned conditions, will increase the sensitivity of PTAs, hence, the chances for detection.

[18] https://www3.mpifr-bonn.mpg.de/staff/pfreire/NS_masses.html

[19] The highest potentially achievable precision of TOAs is a function of the pulse width and the signal-to-noise ratio of the integrated profile.

[20] which is a product of combined efforts by the European and Parkes Pulsar Timing Arrays (EPTA and PPTA, correspondingly) and North American Nanohertz Observatory for Gravitational Waves (NANOGrav)

1.8.2 Studying dense matter physics

The high degeneracy of matter in pulsar interiors predisposes the extreme form of the equation of state (EOS), one of the most fundamental characteristics relating pressure, density and temperature. Constructing the EOS requires considering both condensed matter physics and quantum chromodynamics (QCD) as it is thought that compact stars exhibit quantum phenomena: from superfluidity and superconductivity to the existence of novel phases of matter (for example, quark cores for two-solar-mass pulsars (Lai & Xu, 2011)). Existing EOSs (Lattimer, 2012) put different constraints on the observed properties such as the mass-radius relation, the maximum and minimum possible mass and the highest rotation rate (Lattimer & Prakash, 2001; Lattimer & Prakash, 2004). By measuring precisely the neutron star masses, it is possible to test the predicted values and confirm or rule out particular equations.

1.8.3 Properties of the interstellar medium

Modulations of the pulsar signal caused by its interaction with the interstellar medium on the way to the observer (see Section 1.5) give an excellent opportunity to investigate the properties of the cold ionised plasma. For example, the electron content along different sightlines can be estimated by measuring the signal's dispersion if the distance to the source is known from independent measurements. The Galactic magnetic field strength can be determined by tracking the Faraday rotation of the polarised radio emission. Irregularities in the electron density responsible for the Galactic turbulence can be probed by observing pulsar scintillations and DM variations.

1.8.4 Understanding neutron star population and binary stellar evolution

The continued discovery of new pulsars through pulsar surveys will enrich our knowledge of the underlying neutron star population and clarify the mechanisms of neutron star formation. The latter is currently an open question due to the so-called birthrate problem (Popov et al., 2006; Keane & Kramer, 2008) that arose from the discrepancy between the observed supernovae rate and the number of neutron stars predicted by population models, if the new observational manifestations of neutron stars such as RRATS (see Section 1.6.4) and X-Ray Dim Isolated Neutron Stars (XDINS) (see e.g. Haberl, 2004) are taken into account. To explain this discrepancy, other channels of formation, for example, by accretion-induced collapse of a white dwarf (Dessart et al., 2006; Freire & Tauris, 2014)) have been hypothesized. Measuring the binary parameters of new discoveries and looking at the population as a whole, such theories can be tested.

1.9 Thesis outline

In this thesis the main focus is given to searching for pulsars with the 100-m Effelsberg radio telescope and the further follow-up of the discoveries made.

In **Chapter 2** I describe the methods and instrumentation used in pulsar searches in general and give special attention to those relevant for projects with the Effelsberg radio telescope.

In **Chapter 3** I report on the latest updates on the High Time-Resolution Universe Pulsar Survey – the North: the all-sky survey being conducted with the 100-m Effelsberg radio telescope. In this chapter I show the recent progress in observing and processing the data, analyze the survey sensitivity and present newly discovered pulsars.

In **Chapter 4** I provide detailed timing solutions and speculate on possible evolutionary scenarios for "Two MSPs from the HTRU-North", PSR J2045+3633 and PSR J2053+4650, two most exciting survey discoveries in the past five of years.

In **Chapter 5** I discuss smaller projects conducted with the Effelsberg telescope, namely: timing of the unusually eccentric pulsar–He white dwarf system PSR J1946+3417 and searching for repeating radio signals from FRB 150418.

In **Chapter 6** I summarize the current work and consider future prospects.

Chapter 2

Pulsar and transient searches

In this chapter I will briefly describe: 1) how radio signals undergo transformation from being weak oscillations of the electromagnetic field gathered by an antenna to becoming a ready-to-work-with set of quantized values recorded in a file; 2) what operations should be performed over these values to extract information about the nature of the source, i.e. to make a conclusion whether the received signal is a pulsar or terrestrial signal, or just noise.

2.1 Instrumentation and data acquisition

In this thesis all the data were obtained with a single-dish telescope, hence, in the following discussion we consider the scheme with this kind of antenna.

Fig. 2.1 shows a typical system of pulsar data acquisition. Conventionally it consists of two parts: the *frontend* and the *backend*. The frontend deals with the original radio frequency (RF) signal on its way from the antenna to the down-converting mixer. The electromagnetic waves collected and focused by the antenna's parabolic reflector are conveyed to the receiver through the feed horn where they are transformed into alternating electric voltage of the same radio frequency. Two orthogonal polarisations are selected by the probes (horizontal and vertical for linear polarisation, or clockwise and counterclockwise for circular) placed at the output of the horn and further follow the same paths in separate channels.

The induced voltage is very tiny, typically just above the thermal noise floor, and must be amplified. Amplification, in general, strengthens both the wanted signal and the background noise, thus, reducing the detectability of the former. An effective approach to minimise the injection of the latter is usage of the so-called low-noise amplifiers (LNA), the ones at the start of the chain that are incased in a cryogenic dewar whose temperature is supported at the level of a few tens of kelvins preventing the growth of the noise temperature. Outside the dewar, the signal undergoes filtering and additional amplification (RF amplifier) within the selected frequency range. Usually the frontend parts are physically situated near the receiver as the transmission losses for radio frequencies are high. In order to transfer the signal after the frontend section to the place of processing and storage with minimal losses and without additional distortions introduced by cascaded amplifier chains, it is down-converted to a lower intermediate frequency (IF). Heterodyning, i.e. mixing with the signal of the local oscillator (LO) (or a chain of local oscillators), produces a number of frequencies $f_{\mathrm{IF}_-} = f_{\mathrm{RF}} - f_{\mathrm{LO}}$ and $f_{\mathrm{IF}_+} = f_{\mathrm{RF}} + f_{\mathrm{LO}}$ though only the difference f_{IF_-} called *lower sideband* is further used. The down-converted signal passes through a set of IF amplifiers (more

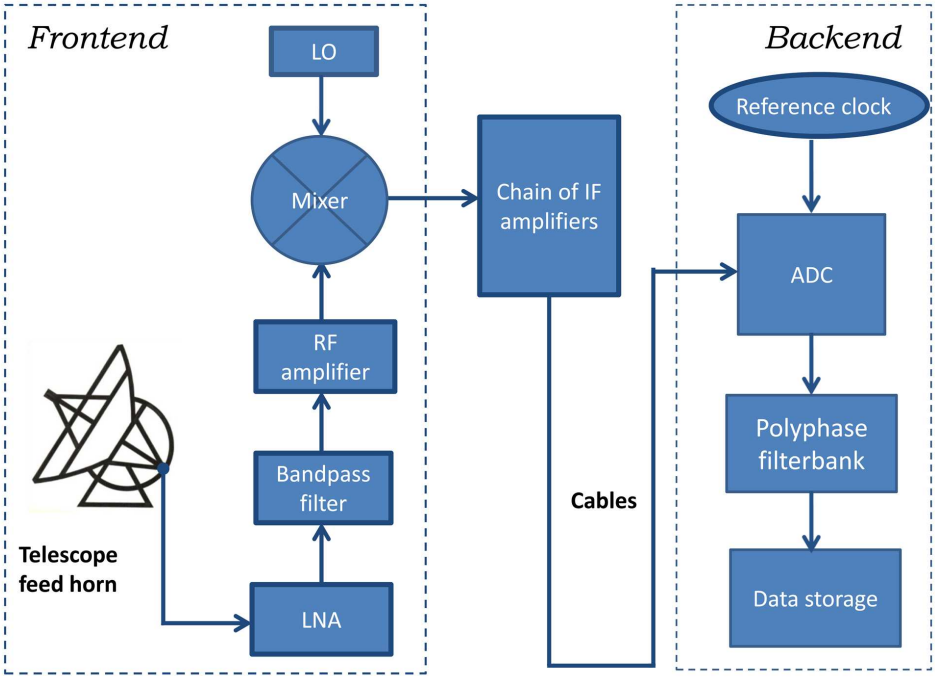

Figure 2.1: A typical data acquisition system used in a pulsar survey.

amplification is always needed!) before leaving the surroundings of the primary focus cabin and then travels a few hundred meters further via coaxial cables to enter the backend.

The backend is all the electronics responsible for signal digitisation, processing and storage. Its key components include an analog-to-digital converter (ADC) producing time-sampled data followed by a spectrometer, a device channelizing this digital data stream into many narrow frequency bands, and a temporary storage machine. Different types of digital spectrometers may be exploited depending on a particular scientific purpose and hardware resources available. The ones that have become widespread during the last decade are the Fast Fourier Transform (FFT) spectrometers[1]. They are constructed on high-performance field programmable gate array (FPGA) boards configured to provide both wide bandwidth and high-frequency resolution. They compute FFT of time-sampled data chunks and transform it into power spectra. To prevent the power from being distributed between adjacent frequency bins (due to the finite length of the FFT), a pre-FFT windowing may be performed[2]. This is implemented in so-called polyphase filterbank spectrometers accustomed for use in pulsar astronomy. The power spectra are further accumulated over a number of clock cycles and integrated to

[1]Their operation principle is based on the property that an N-point Discrete Fourier Transform (DFT) acts like a bank of N finite impulse response (FIR) bandpass filters (see e.g. Price, 2016).

[2]Weighting the FFT coefficients reduces sidelobes but widens the main lobe, i.e the resultant channel bandwidth.

bring the channelized data back in the time domain. Both polarisations are summed since the information about polarisation is not necessary for the purpose of searching. As a last point of the signal path in the data acquisition system, the resultant channels of power time samples are recorded into a file in a raw-telescope format.

2.1.1 Filterbank data format

Different telescopes have different natural formats of data recording. The raw-machine data are usually multiple-bit and, thus, large. To reduce the amount of computational and storage resources needed, these natural-format files are converted to another formats, in most cases with decreasing the number of bits. (However, the losses in sensitivity due to conversion are almost negligible.) Apart from accelerating data transfer significantly, this procedure also facilitates further processing: data converted to standard formats can be later reduced with several specialised software packages available (see Section 2.2.6), without a need for creating separate tools for every telescope.

One of the commonly used formats for processing is the `SIGPROC`[3] filterbank format. A filterbank file consists of a metadata header followed by a data sequence in the form of n-bit numbers. The header contains some general information about the observation, i.e. its duration, source coordinates, antenna position, bandwidth, etc. The data represent sequences of quantised power values S_{ij} recorded at every sampled moment of time t_i (where i goes from 0 to n_{samp}) for every frequency channel f_j (where j goes from 0 to n_{chan}).

2.2 Working with data: pulsar searching

Once the data are transferred to the processing site, the basic steps that should be done over them to search for pulsar (transient) signals include: 1) radio frequency interference rejection, 2) dedispersion, 3) periodicity and/or single-pulse search, 4) candidate sifting and identifying the best ones. While the first three steps can be fully performed within an automatic pipeline, the last one (though being automatised to some extent) still needs a human for making the final decision whether the candidate looks like a pulsar and is worth to be reobserved for possible confirmation.

The further sections of this chapter will describe these steps in more detail.

2.2.1 RFI rejection

Of the radio spectrum below 30 GHz, less than 1% is allocated exclusively for radio astronomical measurements (RR Footnote 5.340, Radio Regulations, 2012), which are, needless to say, performed in a receiving mode only. The remaining majority of frequencies are primarily occupied by actively transmitting (and receiving) industrial, communication, navigation and military services. However, for a plenty of radio astronomical studies, including pulsar science, it is necessary to probe wider bandwidths, spreading far beyond the allocated ranges. This means that human-made signals "flooding the

[3] http://sigproc.sourceforge.net/

ether" in the vicinity of telescopes may enter the receiver (through the antenna's main beam or side lobes) and corrupt the observation since they are many orders of magnitude stronger than the ones of cosmic origin. Thus, a care should be taken to protect the scientific data from contaminating terrestrial radio emissions, which are commonly named Radio Frequency Interference (RFI).

One way to reduce RFI is to place a telescope in an area located faraway from active ground-based broadcasting systems, as is the case for the 100-m Green Bank Telescope. Or make use of natural topographic barriers baffling some portion of unwanted signals, like, for example, the valley hosting the 100-m Effelsberg telescope. Unfortunately, these measures are not enough to get a "clean radio environment": RFI from artificial satellites can still show up. Moreover, spurious signals can be generated on-site by the devices at the observatory. For this reason, most of the electronics is kept in shielded Faraday rooms. Finally, interference can even come from car motors, electric cattle fences or wind turbines reflecting and modulating radio waves by their rotating blades.

This omnipresense of RFI dictates the need for wise removal algorithms that can be applied to the recorded data. For the case of pulsar searching, these algorithms aim to cover the whole time-frequency plane, for treating all the variety of unwanted signals – narrowband or wideband, persistent or impulsive, and often periodic.

Narrowband signals can be excised by zeroing dubious frequency channels whose average power exceeds by a few sigma the threshold set up by the median bandpass. Given that sensitivity to pulsars is proportional to the square root of the bandwidth (see Section 3.5), zeroing a few channels does not impact it severely.

Strong impulsive RFI, which is mostly broadband, can be identified in the time domain. Since man-made signals are not expected to experience dispersion, they can be effectively captured in the so-called zero-DM time series which are obtained by integrating all the frequency channels. By using a running boxcar, these time series are inspected for the presence of conspicuous spikes. If significantly outlying ($>3\sigma$) time samples are detected, they will be further replaced with constant noise values in a way to match the median bandpass.

Periodic RFI can also be dealt with in the Fourier domain. In some cases when the periodicity is known (like, for example, the 50-Hz mains signal and its harmonics), it is possible to excise it by zapping the corresponding Fourier frequencies.

An additional recipe for tracing RFI becomes available when pulsar surveys are carried out with multi-beam receivers, like, for example the PALFA or HTRU surveys (see Section 2.3). Unlike the majority of real pulsars, unwanted signals often appear in different beams simultaneously. Analysis of the multi-beam statistics allows the reduction of the RFI elimination threshold, thus, targeting weaker contamination.

To conclude, it is necessary to say that all the above-mentioned techniques should be applied prudently, tuned to a particular survey, to prevent rejection of the desired pulsar signals.

2.2.2 Dedispersion: removing the propagation effects

As was mentioned in Chapter 1.5, while travelling in the interstellar medium, the pulsar signal gets dispersed: pulses at lower frequencies arrive later than the ones at higher frequencies. If not corrected, this effect can significantly reduce the S/N, hence, our chances to detect the desired signal in the shroud of noise (see Fig. 1.5). For this reason, the recorded data should undergo the procedure of dedispersion. This can be done before or after signal's detection, i.e., by operating either on the raw voltage or on the power data.

Incoherent (post-detection) dedispersion

Incoherent (post-detection) dedispersion is mostly used in pulsar searching systems and deals with the power (intensity) signal after the squaring operation of detection when no phase information is retained. This type of dedispersion takes place within the off-site processing pipeline, usually after RFI removal and prior to searching for periodicities. The total bandwidth, Δf, of a searching backend is preliminary divided into a number of frequency channels.

For a receiver with $n_{\rm chan}$ frequency channels, Eq. 1.14 can be re-written to express the delay in pulse arrival time at the j-th frequency channel, centred at f_j, with respect to some reference, $f_{\rm ref}$ (often the central frequency of the entire band), considering a given DM (Lorimer & Kramer, 2012):

$$\Delta t_j \approx 4.15 \times 10^6\,{\rm ms} \times \left(\frac{1}{{f_{\rm ref}}^2} - \frac{1}{{f_j}^2}\right) \times {\rm DM}, \tag{2.1}$$

unless specified otherwise, here and later in this chapter all the frequency variables in equations are assumed to be in MHz and DM units are ${\rm cm}^{-3}\,{\rm pc}$.

In terms of the number of time samples n_j delayed in the j-th channel with respect to the reference channel, $f_{\rm ref}$, this corresponds to:

$$n_j = \left(\frac{4.15 \times 10^6}{t_{\rm samp}}\right) \times {\rm DM} \times \left(\frac{1}{{f_{\rm ref}}^2} - \frac{1}{{f_j}^2}\right), \tag{2.2}$$

where the sampling time $t_{\rm samp}$ is measured in ms and n_j is taken as the nearest integer number to the value given by the right side of the equation.

To correct for these delays in order to align the pulses in all the frequency channels, the corresponding time samples are appropriately shifted according to Eq. 2.2. Then the frequency channels are added together to maximize the S/N of the potential detection.

However, the compensating effect of incoherent dedispersion is limited by the uncorrectable delays within individual channels:

$$\Delta t_{{\rm DM}_{\rm chan}} = 8.3 \times 10^6\,{\rm ms} \times {\rm DM} \times f_{\rm c}^{-3} \times \Delta f_{\rm chan}, \tag{2.3}$$

where $\Delta f_{\rm chan}$ is the channel width such that $\Delta f_{\rm chan} << f_{\rm c}$.

This means that for a particular survey, characterized by its $\Delta f_{\rm chan}$ and $f_{\rm c}$, intra-channel smearing puts a certain constraint on the pair "spin period–DM" to which the survey can be sensitive: for short-period pulsars at high DMs $\Delta t_{\rm DM_{chan}}$ can reach a considerable fraction of the pulse period. Thereby, $\Delta f_{\rm chan}$ and $f_{\rm c}$ should be chosen in accordance with the desired parameter space to be investigated. As can be seen from Eq. 2.3, higher central frequencies allow the use of wider channels and probe higher DMs. To illustrate this fact, let us calculate $\Delta t_{\rm DM_{chan}}$ for two real surveys: the 1.36-GHz HTRU-North survey (see Chapter 3) and the 350-MHz GBNCC survey (see Section 2.3). HTRU-North has a 300-MHz bandwidth divided into 512 channels with $\Delta f_{\rm chan} = 0.58$ MHz, what results in $\Delta t_{\rm DM_{chan}} = 1.9\,{\rm DM}\,\mu$s. GBNCC has a 100-MHz bandwidth split into 4096 channels with $\Delta f_{\rm chan} = 0.024$ MHz, and using Eq. 2.3 gives $\Delta t_{\rm DM_{chan}} = 4.6\,{\rm DM}\,\mu$s. Thus, in the case of the HTRU-North survey the intra-channel smearing sets a 1-ms limit on the time resolution at DM = 500 pc cm^{-3}, whereas for the GBNCC survey this happens already at DM = 200 pc cm^{-3}.

DM search and the choice of DM step size

In blind surveys candidate DMs are not known *a priori*, hence, a range of DM values must be tried. This makes the whole process computationally expensive. DM ranges probed in the most advanced modern surveys (see Section 2.3 for more detail) may go from 0 up to even 10000 pc cm^{-3}, depending on $f_{\rm c}$ and the sky region to be explored. The choice of the maximum DM is determined by the estimated maximal contribution from free electrons along the surveyed line-of-sights, given by the models of the Galactic electron density (e.g. Cordes & Lazio, 2002; Yao et al., 2017).

The DM step size, ideally, should be chosen to compromise between the load on computational resources and the resultant sensitivity: the objects whose DMs fall in-between the trial values should remain detectable while keeping the number of calculations minimal.

The mismatch in DM determination, ΔDM, (the difference between the true DM value and the trial one used for dedispersion) contributes to broadening of the intrinsic pulse width, $W_{\rm int}$, across the whole bandwidth, Δf as $t_{\rm BW} = 8.3 \times 10^6\,{\rm ms} \times |\Delta{\rm DM}| \times {f_{\rm c}}^{-3} \times \Delta f$.

In a general case, some other factors should be taken into account when estimating pulse broadening, namely: the contributions from the above-mentioned uncorrectable intra-channel smearing, $\Delta t_{\rm DM_{chan}}$, scattering, $\tau_{scat} \sim f^{-4}$ (see Section 1.5.2), and the limit on temporal resolution imposed by sampling, $t_{\rm samp}$.

The resultant effective pulse width is:

$$W_{\rm eff} = \sqrt{{W_{\rm int}}^2 + {\Delta t_{\rm DM_{chan}}}^2 + {t_{\rm BW}}^2 + {t_{\rm samp}}^2 + {\tau_{\rm scat}}^2}. \tag{2.4}$$

For a given spin period, P, the S/N of a detection scales with the effective pulse width, $W_{\rm eff}$, as (see e.g. Lorimer & Kramer, 2012):

$$\mathrm{S/N} \sim \sqrt{\frac{\mathrm{P} - \mathrm{W_{eff}}}{\mathrm{W_{eff}}}}.$$

If one fixes the parameters of the observing system, f_c, Δf, $\Delta f_{\rm chan}$, and the true DM value, then additive contributions from $t_{\rm samp}$, $\tau_{\rm scat}$ and $\Delta t_{\rm DM_{chan}}$ can also be regarded as fixed. Thus, one can move from $W_{\rm int}^2$ to ${W'_{\rm int}}^2 = {W_{\rm int}}^2 + {\Delta t_{\rm DM_{chan}}}^2 + {t_{\rm samp}}^2 + {\tau_{\rm scat}}^2$ and consider only the impact of $t_{\rm BW}$.

Fig. 2.2 and Fig. 2.3 demonstrate the influence of DM mismatch, ΔDM, on the degradation in S/N for the cases of the 1360-MHz HTRU-North survey (see Chapter 3) and the 350-MHz GBNCC survey (Stovall et al., 2014). In each figure different plots (from (a) to (d)) correspond to a particular spin period and a variety of duty cycles.

The relative S/N, $S/N_{\rm rel}$, is calculated as:

$$S/N_{\rm rel} = \sqrt{\frac{P - W_{\rm eff}}{P - W'_{\rm int}} \frac{W'_{\rm int}}{W_{\rm eff}}}, \tag{2.5}$$

and $W'_{\rm int} = \delta P$, where δ is the observed duty cycle.

As can be seen from the plots:

1) the increase in DM offset most severely affects the detectability of short-period pulsars observed at low frequencies;

2) the drop in S/N also scales with duty cycle: it is less rapid for larger δ;

3) high-frequency surveys allow for larger DM steps than low-frequency ones do.

It seems reasonable to choose the DM step in a way that the pulse broadening due to the error in DM, $t_{\rm BW}$, is equal to the sampling time, $t_{\rm samp}$. Then the DM step, ΔDM, becomes:

$$\Delta{\rm DM} = 1.205 \times 10^{-7} \times t_{\rm samp}\,({\rm ms}) \times f_c^3/\Delta f \tag{2.6}$$

The relation 2.6 can be used until the uncorrectable intra-channel smearing, $\Delta t_{\rm DM_{chan}}$, reaches the sampling time, $t_{\rm samp}$, i.e. up to an $n_{\rm d}$-th DM trial[4]. The corresponding value, ${\rm DM_{n_d}} = 1.205 \times 10^{-7} \times t_{\rm samp} \times f_c^3/\Delta f_{\rm chan}$, is called the diagonal DM. With the further increase of n: $n > n_{\rm d}$ the intra-channel smearing, $\Delta t_{\rm DM_{chan}}$, starts to go beyond $t_{\rm samp}$, making using the native time resolution computationally inefficient. The data can now be downsampled by a factor of 2 and Eq. 2.6 can be modified to include the reduced time resolution: $t_{\rm samp}$ can be replaced by $2t_{\rm samp}$ after $n_{\rm 2d} = 2n_{\rm chan} + 1$. The procedure of further downsampling can be repeated when the next multiple (power-of-two) diagonal DMs (3-th, 4-th, etc. or 4-th, 8-th, etc.) are reached.

However, modern search packages (see Section 2.2.6) may employ alternative solutions. For example, `dedisperse_all` software from `SIGPROC` (Keith et al., 2010) uses a bit-shifting operation to efficiently introduce time offsets in neighbouring channels for multiple DMs with one pass through the data. For this reason the data are not downsampled even at high DMs. The DM step sizes are chosen such that a pulsar whose true DM lies between the steps will see a reduction in S/N of $\sqrt{2}$ at most. Fig. 2.4 shows an increase in DM step size as a function of DM trial value, as calculated by `dedisperse_all` for a 3-minute filterbank file from the HTRU-North data.

[4]In this notation the first trial corresponds to zero-DM: ${\rm DM_1} = 0$, $n_{\rm d} = n_{\rm chan} + 1$.

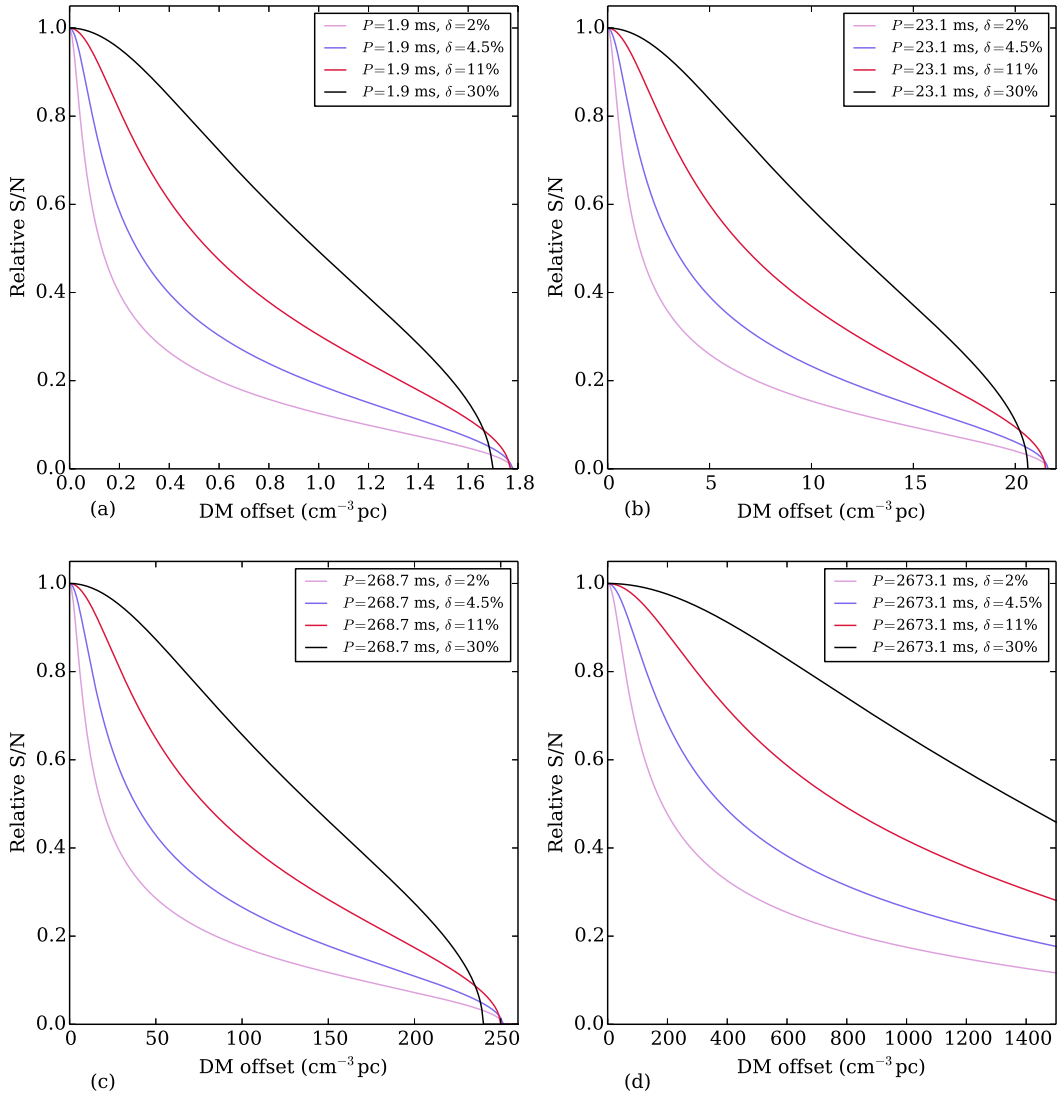

Figure 2.2: Degradation in the relative S/N with the error in DM determination for a set of pulsar spin periods and duty cycles modelled for the HTRU-North survey, having f_c = 1360 MHz and Δf = 300 MHz.

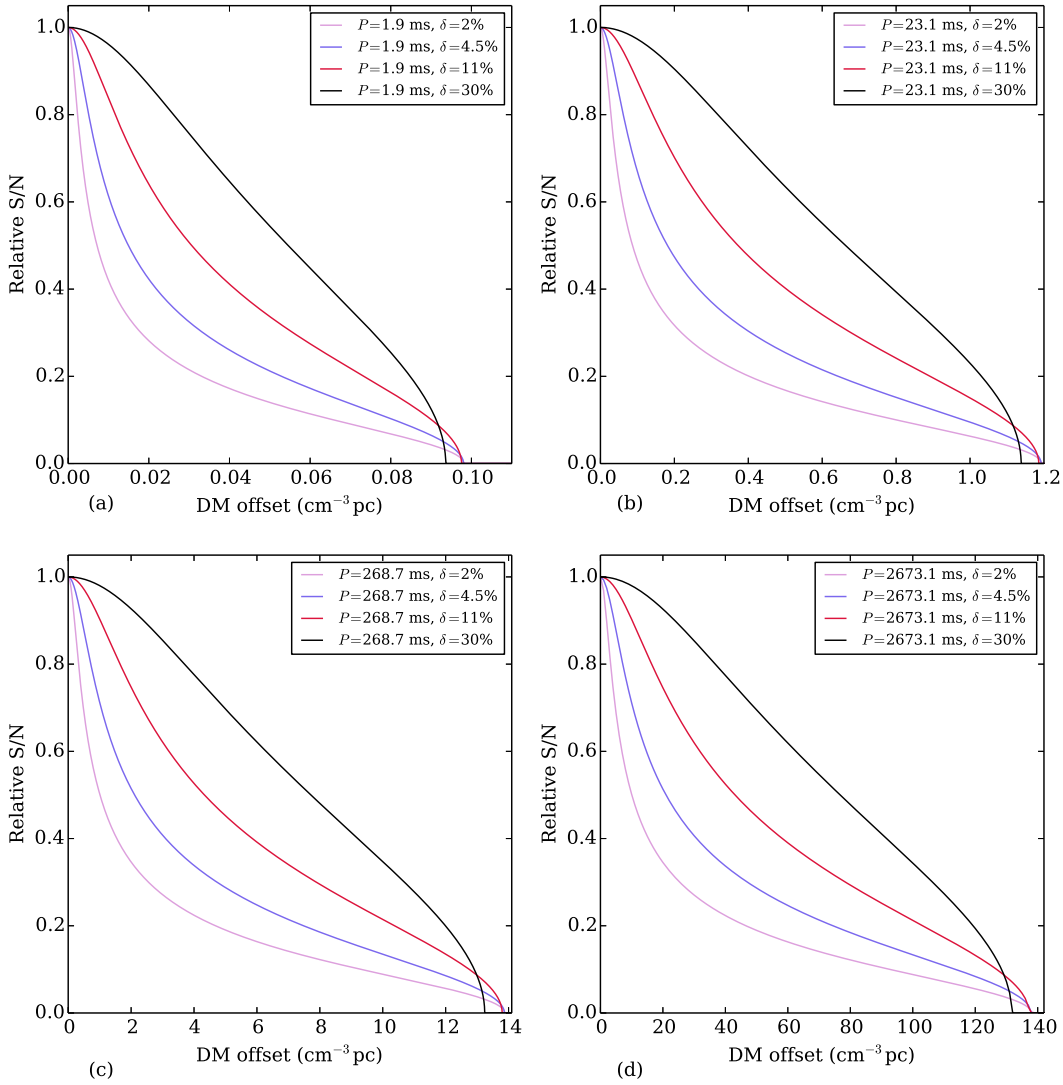

Figure 2.3: Degradation in the relative S/N with the error in DM determination for a set of pulsar spin periods and duty cycles modelled for the GBNCC survey, having $f_c = 350\,\mathrm{MHz}$ and $\Delta f = 100\,\mathrm{MHz}$.

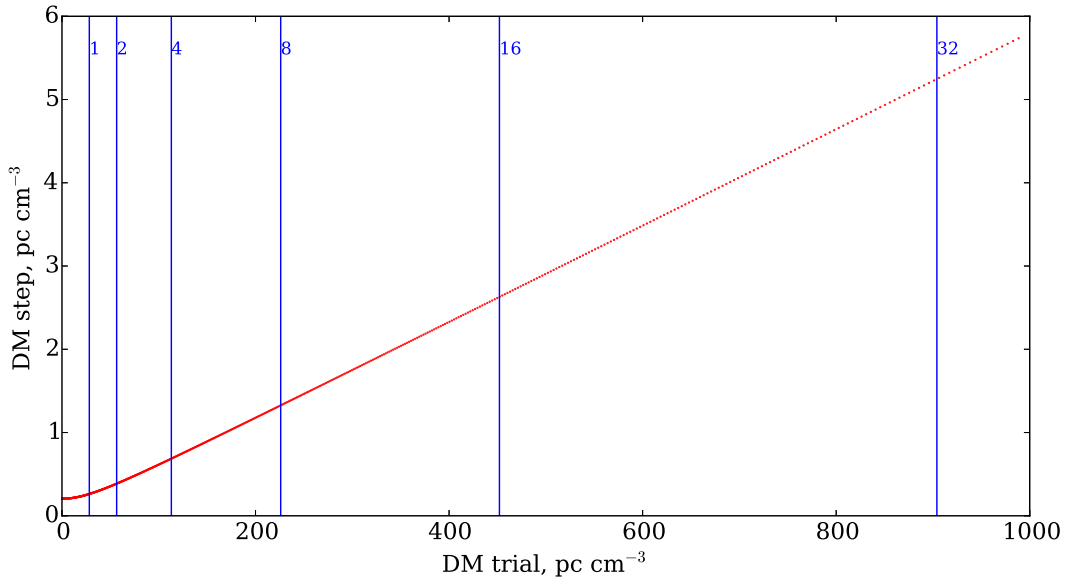

Figure 2.4: DM step size vs. DM trial values for a list of 698 DMs in the range 0-1000 pc cm^{-3} created by `dedisperse_all` on the example of a filterbank from the HTRU-North data. The vertical lines "1", "2", "4", etc. mark the corresponding multiple of the diagonal DM.

The operations of time series dedispersing at different DMs are computationally independent. Thus, to accelerate the processing, it is expedient to apply techniques of threading and task parallelising (see, for example, Section 3.4.5).

Coherent (pre-detection) dedispersion

For some tasks other than pulsar searching, it may be highly desirable to completely remove dispersive delays – for example, for increasing the precision of TOAs in pulsar timing (see Section 1.7). If the source's DM is known, another kind of dedispersion may be applied – coherent dedispersion.

The whole procedure is based on the idea that the effect of the ISM on the pulsar signal can be modelled by a (linear) "phase-only" filtering operation. This becomes clear if one considers not only time delays but also rotations of the signal phase, Φ, as the results of the propagation in the ISM: $\Delta\Phi = -k(f_c + f)d$, where $k(f)$ is the wavenumber and d is the distance to the source. In this formulation, the "ISM-filter" can be generally characterized by its transfer function:

$$H(f_c + f) = e^{-ik(f_c+f)d} \tag{2.7}$$

If the explicit form of $H(f_c + f)$ is known, the originally emitted signal can be obtained from the received signal – the output response of the "ISM-filter" – by an inverse filtering operation.

Hankins & Rickett (1975) derived the equation for the dependence of the wavenumber on frequency, $k(f_c + f)$, and showed that:

$$H(f_c + f) = e^{\left(i\frac{2\pi\mathcal{D}f^2}{{f_c}^2(f_c+f)}\mathrm{DM}\right)} \tag{2.8}$$

where the dispersion constant, $\mathcal{D}$, is related to the plasma frequency, f_p, and the average electron density along the line of sight, n_e, as $\mathcal{D} = \frac{{f_p}^2}{2cn_e}$.

To extract information about the signal's phase, it is necessary to work with complex voltages. Thus, for coherent dedispersion, baseband data are required. Complex sampling of the signal results in time resolution of $1/\Delta f$ (see e.g. Proakis & Manolakis, 2006). Thus, given the same bandwidth, Δf, the time resolution achievable with coherent dedispersion is (minimum n_{chan} times) higher than the one achievable with incoherent dedispersion.

2.2.3 Periodicity searching

2.2.3.1 Pulsar signals in context of signal processing theory: time series and spectral representation

After dedispersion, the signal is represented by a sequence of N equally spaced time samples containing the values of intensity integrated over all the frequency channels: $s_n = \{s(0), s(t_{samp}), s(2t_{samp}), s(3t_{samp}), ..., s((N-1)t_{samp})\}$, where t_{samp} is the sampling interval.

Pulsars are usually very weak sources and, looking only at the time series of the incoming signal, it is almost impossible to trace their periodic features buried in the sea of concomitant noise. However, the pulsar periodicity can be revealed by analysing the signal's spectral content. The spectrum S_k of the digitised time series s_n can be obtained by mapping s_n into the frequency domain with the discrete analogue of the Fourier transform (DFT):

$$S_k = \sum_{n=0}^{N-1} s_n W_N^{kn}, \tag{2.9}$$

where $W_N^{kn} = \exp(-2i\pi nk/N)$ is the so-called phase factor and $i = \sqrt{-1}$.

To get an idea of what kind of spectrum is expected, let us first model a pure pulsar signal. The majority of normal pulsars have duty cycles $\delta \sim$ 2–10% (see Fig. 2.5), whereas MSPs may have the ones up to 20–30% (Kramer et al., 1998). With this in mind, the wanted signal can be presented as a sequence of top-hat pulses, each of width w, received over the length of observation t_{obs} with the period P, corresponding to the pulsar spin period. The spectrum of this function, apart from the fundamental harmonic at frequency $f_f = 1/T$, will also contain multiple harmonics with frequencies $f_k = k \cdot f_f$ and amplitudes determined by a sinc-function envelope, with the number of harmonics laying within the main lobe of the sinc being equal to P/w. Then, restricting the spectrum at the first null, we get the highest frequency of $f_{high} = \frac{1}{P} \cdot \frac{P}{w} = \frac{1}{w}$ Hz. Thus, pulsar spectra usually contain from 4 to 30 detectable harmonics. For a range of the observed spin periods from 0.001 s to 10 s the highest detectable harmonics can reach the order of kHz. Estimating f_{high} is important for

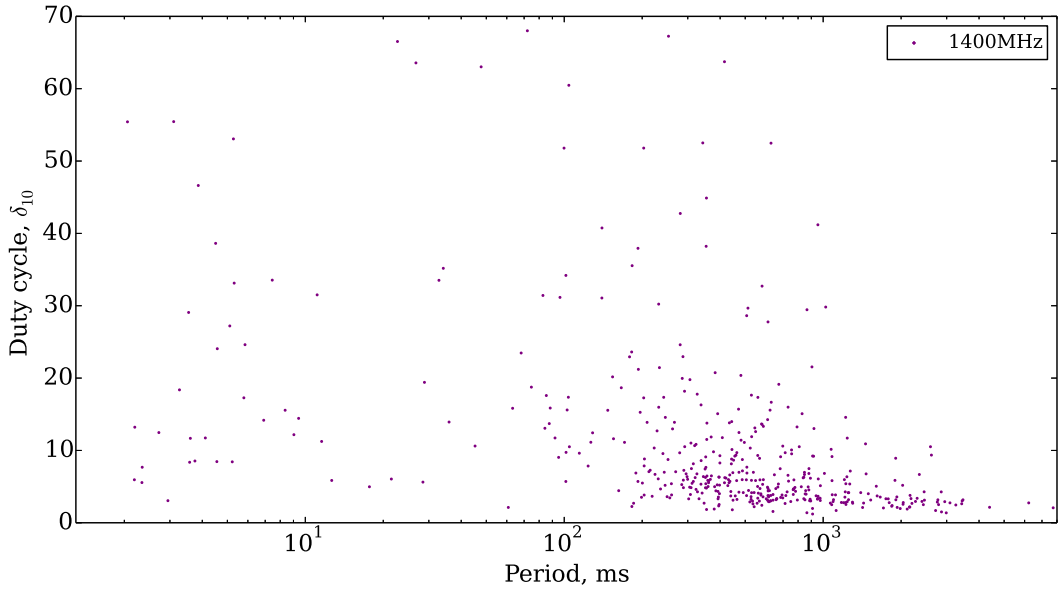

Figure 2.5: The observed distribution of pulsar duty cycles by spin periods. The 1400-MHz data are taken from the `ATNF pulsar catalogue` and include pulsars with reported pulse widths at 10% of the peak intensity.

a proper choice of sampling frequency $f_{\rm samp} = 1/t_{\rm samp}$. The choice of $f_{\rm samp}$ is determined by Kotelnikov-Nyquist-Shannon theorem stating that the sampling rate should twice exceed the highest frequency in the signal's spectrum $f_{\rm samp} \geq 2f_{\rm high}$ to prevent artefacts and aliasing in the reconstructed signal[5].

As follows from Eq. 2.9, the amplitude spectrum of the signal, s_n, is represented by the values of $|S_k|$ in every frequency bin. The k-th Fourier bin has a central frequency $f_k = k/(Nt_{\rm samp}) = k/t_{\rm obs}$ Hz and the subsequent bins are spaced at $1/t_{\rm obs}$ Hz. This means all the frequencies falling within one bin are indistinguishable. This is an important factor responsible for a sinc-shaped decrease in sensitivity to signals whose frequencies differ from exactly f_k (see e.g. Ransom, 2001). There exist a few methods to mitigate this scalloping effect, for example, zero padding or different variants of Fourier domain interpolation. In the first case the addition of zeros (or mean values of the data that also add no power) to the time series serves to artificially increase the number of samples N and obtain a smaller bin width, though raising the computational costs. In the latter case the power contained in "inside-bin" (non-integer) frequencies can be recovered by correlating the nearest integer bin with the inverse of the sinc response. This method is especially useful for fine-tuning an already detected frequency.

To estimate the distribution of the signal's power with frequency one can calculate the power spectrum: $P_k = |{\rm Re}(S_k)|^2 + |{\rm Im}(S_k)|^2$.

[5]This condition can also be written in terms of the so-called *Nyquist* frequency $f_{\rm Nyq} = f_{\rm samp}/2$: $f_{high} < f_{\rm Nyq}$.

2.2.3.2 Computational efficiency of the DFT

In a most general case, calculating a DFT of an N-point input sequence of time samples, s_n, will result in an output sequence of N complex-valued numbers, $S(k)$, represented by N points for the real part of the DFT $\mathrm{Re}(S_k)$ and N points for the imaginary part of the DFT $\mathrm{Im}(S_k)$. Such calculation involves N^2 floating-point operations of complex multiplication and $N^2 - N$ operations of complex addition. This can be computationally expensive (especially, multiplication). For example, the DFT of the time series recorded in a 3-minute filterbank file sampled every 54 μs and having the length of $N = 3295880 \simeq 1.6 \times 2^{21}$ data points requires $\mathcal{O}(2^{43})$ operations both for summation and multiplication. However, it is possible to reduce the demand on computational resources by exploiting the redundancy of the conventional DFT. As can be seen from Eq. 2.9, the DFT is always a complex-valued function, though for real-valued signals the DFT is conjugate symmetric[6], and can be calculated only for the first half of the Fourier frequencies, thus $k = 1, ..., \frac{N}{2}$.

Another smart simplification is related to the order in which the operations are performed and is implemented in fast algorithms of the Fourier transform (FFT) (see e.g. Oppenheim & Schafer, 2009). These algorithms are based on recursive decomposition of the initial N-point sequence presented through its composite multiples into a number of subsequences (where the number is determined by the radix of these multiples). The classical case of N being a power of 2 allows splitting every next subsequence into two halves in $\log_2(N)$ steps until N single-point daughter subsequences are obtained and then performing N single-point DFTs independently, thus, resulting in $\mathcal{O}(N \log_2 N)$ operations. Different algorithmic FFT solutions for data of different size are available.

Standard pulsar searching packages such as `PRESTO` and `SIGPROC` (see Section 2.2.6) include FFT which is applied to a dedispersed time series.

2.2.3.3 Spectral whitening

The noise present in the recorded signal is usually assumed to be uncorrelated. Assuming additionally noise stationarity within the integration time, one can expect the noise power to be equally distributed between the frequency bins or, in other words, the noise can theoretically be considered "white". However, in reality power spectra look far from being uniform. As can be seen in Fig. 2.6a showing the power spectrum of a 3-minute observation the "uniformity" is distorted at the low-frequency end. This abrupt rise of power values (towards zero frequency) is attributed to the "reddening" of the spectrum due to the influence of frequency-dependent noise caused by both natural (for example, atmospheric) and instrumental processes (for example, gain fluctuations in the receiver), as well as man-made RFI entering the telescope. This low-frequency noise affects the potential detectability of pulsars, being especially responsible for reducing sensitivity to the long-period ones (see e.g. Lazarus et al., 2015). A way to mitigate the deleterious influence of red noise is to "whiten" the

[6] what makes it also symmetric around the Nyquist frequency

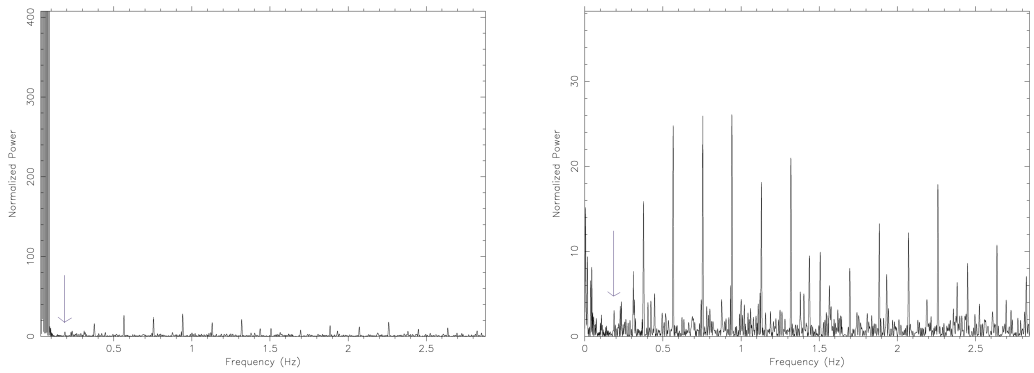

(a) (b)

Figure 2.6: Spectral representation of a 3-minute observation of PSR J1840−0840 (p=5.309 s) dedispersed at the correct DM=272.0 pc cm^{-3}: a) the original power spectrum of the signal containing red noise; b) de-reddened version of this power spectrum. The arrow in each figure points to the fundamental frequency ~ 0.192 Hz. The data are collected within the HTRU-North project.

power spectrum before searching for periodicities. Moreover, as was shown by Ransom (2001), dealing with a white-noise model makes the estimation of the signal's significance level easier. A quasi-constant form of power spectral density can be achieved after some manipulations. To obtain a nearly zero mean and a unit root-mean-square (rms), one should:

1) split the spectrum into short chunks where the local statistics (mean/median and rms) will be calculated,

2) subtract this running mean/median from the data within the particular chunk,

3) normalise the rms of every chunk using the running rms.

The number of bins (window length) used for normalisation may vary with frequency: for example, the `PRESTO` searching package implements the windows whose lengths are shorter for the lower frequencies than for the higher ones, spreading from 6 to 200 bins. As an example, the result of de-reddening procedure performed with `rednoise` utilite from `PRESTO` on a data file containing PSR J1840−0840 can be seen at Fig. 2.6.

2.2.3.4 Harmonic summing

Since the signal's power is expected to be spread in many harmonics (see Section 2.2.3.1), the most efficient way to use this power and, consequently, increase the detection S/N is to sum the fundamental harmonic with its multiples. For this a set of complementary spectra is constructed as follows. The raw spectrum, which is sometimes called fold 1 (see Fig. 2.7a), is divided into two halves, and its first half is stretched twice such that every second harmonic "moves to a place" of its corresponding fundamental (see Fig. 2.7b). Then the result of this procedure is summed with the original spectrum to produce fold 2 (see Fig. 2.7c). The S/N of fold 2 will be $\sqrt{2}$

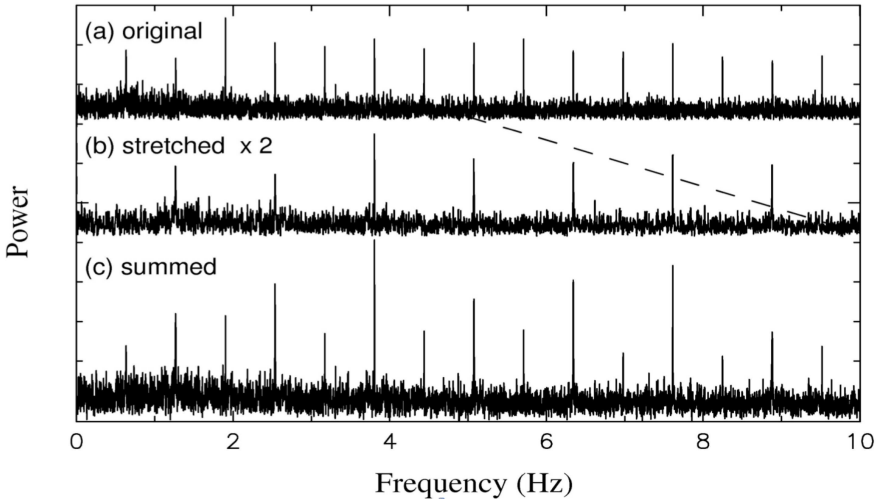

Figure 2.7: The illustration of harmonic summing procedure for the first stretch-and-add round: a) the original power spectrum; b) twicely stretched spectrum; c) the sum of a) and b) spectra. Figure is taken from Lorimer & Kramer (2012).

times larger than the S/N of fold 1, since the power in harmonics is doubled and the rms of the (supposedly Gaussian) noise is increased by $\sqrt{2}$, assuming that the power is equally distributed between the bins without signal. Repeating similar operations a few times, it is possible to get further folds including N=4, 8, 16 or 32 harmonics (sometimes up to 128 (Ransom et al., 2002)) and achieve a vigorous boost in S/N proportional to $\sqrt{N}$. However, in the case of pulsars with wide profiles and spectra containing a small number of harmonics, the highest folds may work inefficiently as they only add more noise. Since the morphology of the desired signal is not known *a priori*, the candidates (periodicities with spectral S/Ns exceeding some threshold) from each of the summation rounds are saved to be inspected for significant peaks and for further sifting.

2.2.3.5 Searching for binary pulsars: acceleration search

Pulsars in binary systems perform orbital motion introducing Doppler shifts into their rotational periods, as seen by the observer. In terms of the observed spin frequency $\nu_{\rm obs}$, the Doppler formula gives:

$$\nu_{\rm obs}(t) = \nu \left(1 - \frac{v(t)}{c}\right), \tag{2.10}$$

where ν is the "true" spin frequency, $v(t)$ is the line-of-sight velocity of the pulsar, c is the speed of light and the high-order terms of (v/c) are neglected.

If the instant line-of-sight velocity changes from $v_1 = v(t_0)$ to $v_2 = v(t_0 + t_{\rm obs})$ during the observation time, $t_{\rm obs}$, where t_0 is the moment of start, then, following Eq. 2.10, the observed spin frequency drifts from $\nu_{\rm obs_1} = \nu\left(1 - \frac{v_1}{c}\right)$ to $\nu_{\rm obs_2} = \nu\left(1 - \frac{v_2}{c}\right)$. If the difference between $\nu_{\rm obs_1}$ and $\nu_{\rm obs_2}$ is resolvable, i.e. larger than

one frequency bin, this means that the power of the "true" frequency bin will be spread between the adjacent ones. Depending on how many bins are involved in this effect, it can prevent the periodic signal from being detected. The severity of the observed power redistribution is determined by the orbital parameters and acceleration, as well as the integration time. If the latter is much shorter than the orbital period, P_b, $t_{\rm obs} \lesssim P_b/10$, then the acceleration, a, can be considered constant (Camilo et al., 2000; Ransom et al., 2003; Eatough et al., 2013) and $v(t) = at$. Calculating the frequency drift during the observation time, $|\Delta\nu_{\rm obs}| = |\nu_{\rm obs_2} - \nu_{\rm obs_1}| = a\nu t_{\rm obs}/c$, and relating it to the number of drifted bins, $N_{\rm drifted}$, where the bin width equals $1/t_{\rm obs}$, one can get:

$$N_{\rm drifted} = a\nu {t_{\rm obs}}^2/c. \tag{2.11}$$

As follows from Eq. 2.11, in principle, it should be possible to correct for this detrimental effect if the power can be "turned back" to the true bin. In some sense the procedure is identical to dedispersion: different trial acceleration values should be checked until the highest S/N is reached, i.e. all the affected bins are found. However, acceleration search is an even more computationally intensive task than dedispersion. That is the reason why the number of trials becomes crucial for restoring sufficient sensitivity without using excessive resources. The most important parameters determining this compromise are the acceleration step and range. The step should be chosen in a way to ensure a drift of no more than one frequency bin for a pulsar signal of a shortest targeted period (around 1 ms). The range usually depends on the goals of a particular survey and available computing power. Searches for highly relativistic systems, (i.e. those with large eccentricities and orbital periods of a few hours), which are supposed to experience extreme accelerations, consider trial values up to hundreds or even a thousand (for potential pulsar-black hole binaries) of m s^{-2} (Liu et al., 2014c). At the same time, not highly accelerated binaries can be still found within only standard periodicity search.

2.2.4 Separating the "chaff" from the "wheat": sifting, folding and visual inspection

Sifting

After each of the dedispersed time series has passed through the periodicity (and, optionally, acceleration) searching pipeline, the detected suspects are recorded into a list. A typical representative of this list is characterised by a spin frequency/period, DM, acceleration (if relevant) and spectral S/N corresponding to each harmonic summation round. The exact number of candidates generated in one observation varies for a particular survey, depending on the technical facilities available (antenna gain, receiver bandwidth, etc.), integration time, local RFI situation and detection thresholds. For modern large-scale surveys it is counted in tens of thousands, while the total expected outputs (upon completion) reach millions of suspects! Only a small fraction of these suspects will contribute to pulsar detections. To reduce the number of

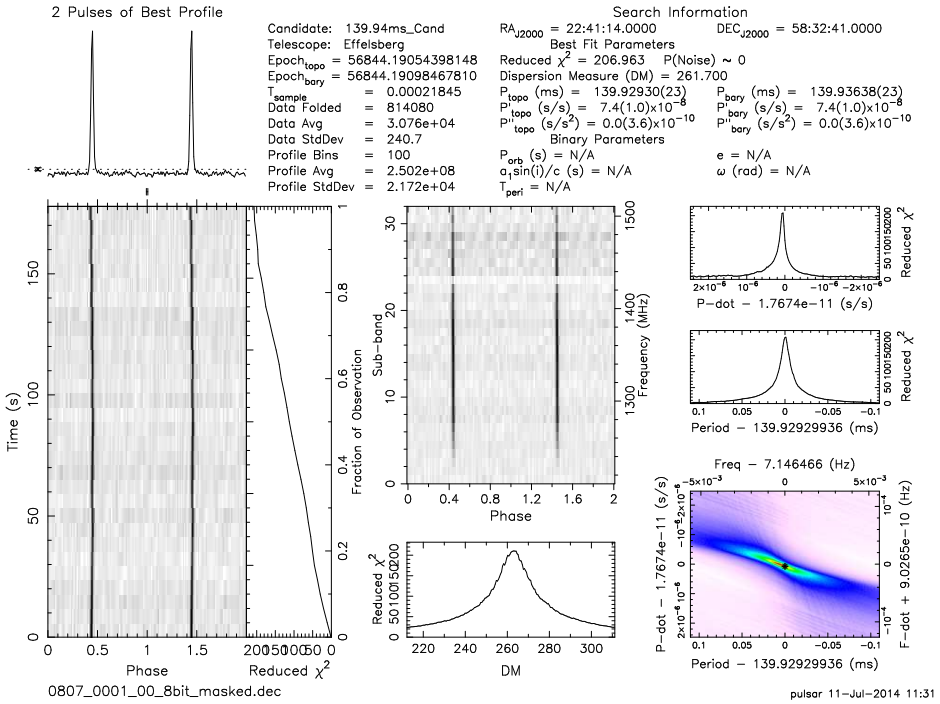

Figure 2.8: A set of diagnostic plots produced in the result of folding a 3-minute observation containing PSR J1730−3350 with P=139.94 ms and DM=261.7 pc cm^{-3}. The data are taken within the HTRU-North project.

candidates that will proceed to the next stages of the analysis, the procedure of sifting should be performed. It typically includes rejection of periodicities that have:

1) low S/N (beyond the survey's estimated detection threshold);

2) periods not expected for real pulsars (e.g. $P > 15$ s and $P < 0.5$ ms);

3) very low DMs (DM $<$ 1–2 pc cm^{-3}).

Furthermore, the same pulsar may show up in different harmonics and at multiple trial DM and acceleration values – these duplicate periodicities also need to be removed. Once this is finished, the "survivors" of sifting are ranked by their spectral S/N and stored in a new list.

Folding

Next the top candidates are folded. For this the original filterbank file is dedispersed at the candidate's DM and the resultant de-dispersed time series is divided into $n_{\rm si}$ identical segments – subintegrations – containing an integer number m of candidate's pulse periods P. (If the number of time samples at the end of the time series is not enough to form a whole period, these time samples are cut, and the whole time series has a slightly reduced length $t*_{\rm obs}$.) In other words, each subintegration has a length $t_{\rm si} = t'_{\rm obs}/n_{\rm si} = mp$. Each of m time intervals P is, in turn, divided into $n_{\rm bin}$ equally spaced elements (time bins) corresponding to particular rotational phases. Thus, the whole time series is now represented as an array of intensity values: a_{ikn},

where $i = 1, 2, ..., n_{\rm bin}$; $k = 1, 2, ..., m$; $n = 1, 2, ...n_{\rm si}$. As a next step, the averaged sum of values across k is calculated for every subintegration. This results in a new array of elements $\tilde{a}_{in}$ which can also be considered as a sequence of $n_{\rm si}$ subintegrated pulse profiles, each made of $n_{\rm bin}$ time bins. These subintegrated profiles already contain a much stronger signal than does a time interval corresponding to a single pulse period: the pulsar signal increases proportionally to the number of summed elements, while the increase in noise follows the square root law. Further summation of elements across n gives the last array A_i, the intensity averaged over the whole observation as a function of pulsar's rotational phase. This is referred as the integrated pulse profile.

Candidate selection

The outcome of folding is a set of diagnostic plots (see Fig. 2.8) containing information about the integrated pulse profile, DM−S/N and acceleration−S/N or $\dot{P}$−S/N curves, as well as about the signal's presence in particular subbands/subintegrations (observation time−pulse phase, frequency−pulse phase plots). Some peculiar features in these plots can help to distinguish a true pulsar signal from RFI. For example, though genuine pulsar pulse profiles can differ by their exact morphology, they are unlikely to have a pure sinusoidal or sawteeth form – such pattern is a telltale sign of signal's industrial origin. Further, since pulsars are known to emit in a broad range of frequencies, the true signal should cover the whole (effective) observing bandwidth. And vice versa: a narrowband trace in the frequency−pulse phase plot can definitely rule the candidate out. Additionally, the majority of pulsars, excluding scintillating ones and RRATs, are expected to appear persistently during the whole observation, unlike, for example, space-time coded terrestrial signals. Finally, a noticeable peak centred at a non-zero value in the DM−S/N curve may be a testimony of the signal's extraterrestrial origin. However, it should be noticed that a strong RFI very often also shows up at non-zero DMs. Moreover, a number of RFI signals may demonstrate a pulsar-like behaviour with narrow-peak profiles and wideband emission. Thus, a decision whether the candidate is a pulsar or not can not be made based on one factor, it is necessary to consider all the pieces of information provided in diagnostic plots together.

The results of folding can either go directly to a trained human inspector who makes the final decision or can be first analysed by specific programs. Since modern pulsar surveys produce millions of candidates, it is inexpedient to rely on human resources only. A much more effective approach includes applying different "smart" algorithms for ranking the candidates by their "pulsar-likeness". These algorithms may operate within artificial neural networks (Eatough et al., 2010) or/and be based on some euristic scores (Lee et al., 2013) or use image pattern recognition (Zhu et al., 2014). Implementation of such algorithms into the pipeline may save many "human-hours" and significantly reduce the number of plots for visual inspection.

The most promising candidates chosen by a human inspector are saved for confirmation with a telescope. If the signal with the same (or close) parameters appears in a new observation, its pulsar nature is considered proved and the source becomes a subject of further timing (see Chapter 4).

2.2.5 Single-pulse search

Fourier-based techniques proved to be a useful tool for finding faint periodic signals. However, not all pulsars demonstrate an easily detectable periodicity: for example, RRATs (see Section 1.6.4) or nulling pulsars with high nulling fractions emit quite sporadically. Further, some sources may exhibit a significant pulse-to-pulse variability, up to a few orders of magnitude: the amplitudes of the so-called giant pulses, first observed for the Crab Pulsar (Staelin & Reifenstein, 1968), may reach the values of 10^2–10^3 times the mean pulse amplitudes. Another difficulty is related to detecting long-period pulsars: they may not show up in periodicity searches because of the red-noise contamination of the low-frequency part of the spectrum, or because the number of strong pulses received during the observation may simply be insufficient for detection – usually in surveys with short integration times. In the aforementioned cases searching for single pulses becomes more efficient than applying FFT.

The detection of pulsed signals is based on the operation of matched filtering. Since the pulse width is not known *a priori*, the dedispersed time series should be cross-correlated with boxcars of different width (multiples of $t_{\rm samp}$). Then, the match is expected when the trial boxcar's width is equal to the pulse width.

To distinguish the real signal from random noise fluctuations, the output of the cross-correlation procedure should be tested against a pre-defined S/N threshold, usually a few units. The parameters of the signals having S/Ns exceeding the threshold are saved into a list. Then, to visualise the results of the whole procedure, the candidates are plotted in the DM vs. time plane, often using size and colour to denote the S/N and width (see Chapter 5.2 for an example).

2.2.6 Pulsar search software

Though the basic scheme of pulsar searching (see, for example, Fig. 2.9) seems quite straightforward, the exact realization of algorithms from scratch requires a lot of effort. Thus, it is more practical to develop standardized searching software that can be modified for the needs of a particular survey when implemented into the pipeline. Currently the most well-tested and frequently used tools are `PRESTO`[7](the PulsaR Exploration and Search TOolkit (Ransom, 2001)) and `SIGPROC`[8]. Designed for CPU[9] architectures, they have vastly contributed into enlarging the known pulsar population. With GPU[10] architectures becoming more widespread in data processing, newly developed GPU-based pulsar searching tools are gaining popularity, like, for example, `PEASOUP`[11] inspired by `SIGPROC`.

Regardless of the base platform, the packages include a set of utilities to work with frequency channels and time samples, namely, to perform dedispersion, FFT periodicity search, acceleration search, candidate optimisation and folding. At the

[7]http://www.cv.nrao.edu/ sransom/presto/
[8]http://sigproc.sourceforge.net/
[9]central processing units (CPU)
[10]graphics processing units (GPU)
[11]https://github.com/ewanbarr/peasoup

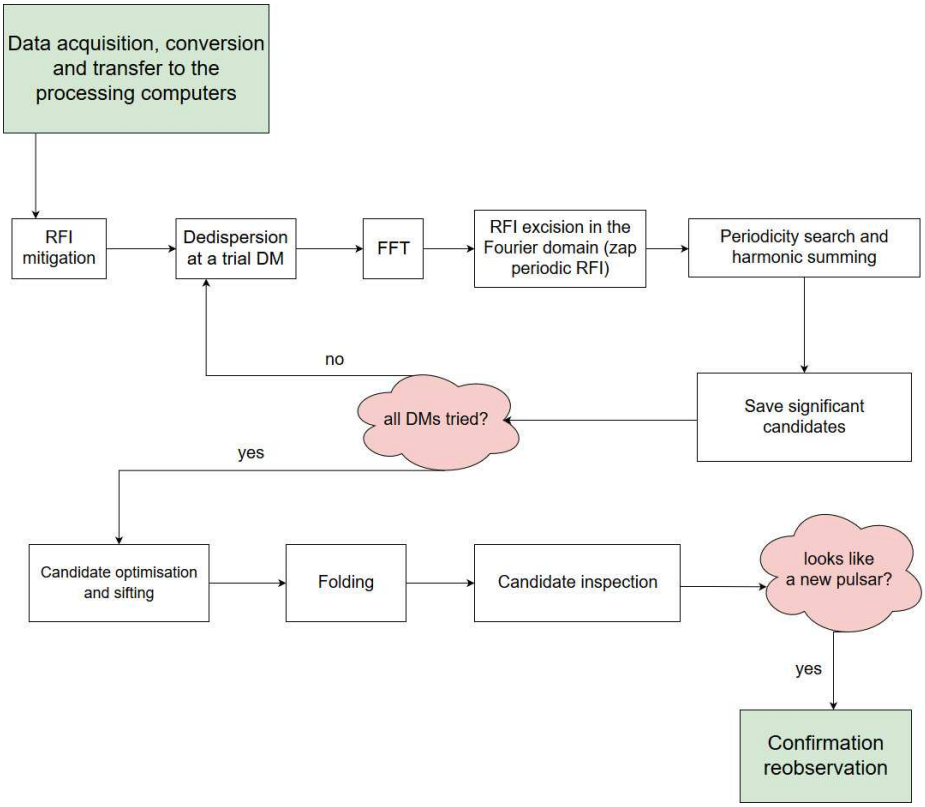

Figure 2.9: Schematic representation of a basic pulsar searching pipeline without acceleration search.

same time, they are different in a number of algorithmical solutions. For instance, the CPU-based `PRESTO` and `SIGPROC` do not share the same approach to acceleration search: while `PRESTO` operates in the Fourier domain, `SIGPROC` uses time-domain resampling (as well as the GPU-based `PEASOUP`). Another difference is related to the way how the packages estimate detection significance: `SIGPROC` and `PEASOUP` use S/N of the peaks in the normalised power spectrum whereas `PRESTO` calculates the Gaussian significance (sigma) of the peaks assuming the noise to be white.

Usually the choice of a particular software suite depends on the survey parameters (integration time, bandwidth, range of DMs to be probed, etc.) and available computational resources. Very often separate functional utilities from different packages can be combined together when assembling a pipeline. An example of using both GPU and CPU tools for processing the data from the HTRU-North survey is given in Chapter 3.4.5.

2.3 Major pulsar surveys

An important consideration when designing a pulsar survey is the observing frequency. Most pulsars have a steep spectral index making them strongest at the lower frequen-

cies, at the same time, the ISM effects are also stronger at these low frequencies. While intra-channel dispersion (a limiting factor for finding short period pulsars at high DM) can be mitigated by increasing the number of channels across the bandwidth, the effect of scattering cannot be removed from the data. Additionally most pulsars are found at low Galactic latitudes where the continuum emission at low frequencies is significant. These competing effects tend to push most pulsar surveys towards 1400 MHz where receivers are shared with e.g. HI observations. Integration time is another critical factor. The longer the observation the more sensitive the survey can be, however, these long integrations require vastly more computing resources to process.

The most successful survey to date was the Parkes Multibeam Pulsar Survey (PMPS) (Manchester et al., 2001) making use of the 13-beam 288-MHz bandwidth L-band receiver. Its southern hemisphere location provided excellent access to the inner Galaxy and the survey of the Galactic plane resulted in more than 830 discoveries what made it the standard by which other surveys are compared.

Since the PMPS there has been considerable development in searching backends and the computing needed to process the data. The High Time Resolution Universe survey (HTRU-South) (Keith et al., 2010) (also at Parkes) was designed to take advantage of both of these areas. It has higher frequency and time resolution reducing intra-channel smearing and allowing the survey to search deeper into the Galaxy. The discovery of ~ 830 pulsars, many of them at high DMs, has shown this technique to be successful.

The HTRU-North survey (Barr et al., 2013) was designed to match the specifications of the southern survey utilizing the 7-beam L-band receiver on the Effelsberg telescope. The larger gain of the telescope (compared to that of Parkes) allows using shorter integration times, but the smaller number and size of the beams mean that overall more observing time is required. Although HTRU-North does not have the same large sections of Galaxy to observe, the relative lack of surveys in the north makes this survey particularly interesting.

Beyond the HTRU surveys there are several other comparable projects. The SPAN 512 survey (Desvignes et al., 2013) at the Nançay telescope is designed to complement the HTRU-North survey by extending the mid-latitude part of the survey to higher latitudes. At Arecibo the huge gain of the telescope is being used by the PALFA survey (Cordes et al., 2006). The sensitivity of the telescope allows short integration times particularly sensitive to short-period binaries. However, Arecibo has a restricted view of the Northern sky, with the declination limit of $+38°$. Table 2.1 gives the parameters of the high-frequency surveys described above.

There are also low-frequency surveys at both AO and GBT (see Table 2.2) which are particularly sensitive to steep spectrum, low-flux pulsars. While the low frequencies limit the DM a short-period pulsar can be detected at, they are expected to provide information about the low-luminosity population which, when combined with surveys at higher frequencies, will improve our understanding of the overall pulsar population.

Table 2.1: Parameters of some ongoing 21-cm pulsar surveys. f_c is the central observing frequency, $\Delta\nu_{chan}$ is the frequency channel resolution, t_{samp} is the sampling rate, and t_{int} is the integration time.

Survey	HTRU			PALFA		SPAN512
Telescope	Parkes			Arecibo		Nançay
Start date	2008			2004		2012
Survey regions	High-lat	Mid-lat	Low-lat	Inner Galaxy	Anti-centre	-
Sky coverage, δ	$\delta < +10^\circ$			-		-
Sky coverage, l	–	$-120^\circ < l < 30^\circ$	$-80^\circ < l < 30^\circ$	$32^\circ < l < 77^\circ$	$168^\circ < l < 214^\circ$	$74^\circ < l < -150^\circ$
Sky coverage, b	–	$\lvert b\rvert < 15^\circ$	$\lvert b\rvert \leq 3.5^\circ$	$\lvert b\rvert < 5^\circ$		$3.5^\circ < \lvert b\rvert < 5^\circ$
t_{int}, s	270	540	4300	134/268	67/180	1080
Receiver	13-beam			ALFA 7-beam		NRT
Backend	PBSR			WAPP/Mock		NUPPI
f_c, MHz	1352			1420/1375		1486
Bandwidth, MHz	340[a]			100/322		512
$\Delta\nu_{chan}$, MHz	0.39			0.39/0.336		0.5
Number of channels	1024[a]			256/960		1024
t_{samp}, μs	64			64/65.476		64
DM searched, pc cm^{-3}	0-2200/3000			0-9866.4		0-1800

[a] The central frequency was increased to 1420 MHz in 2005 to reduce the influence of interference.

Table 2.2: Parameters of some ongoing low-frequency pulsar surveys. f_c is the central observing frequency, $\Delta\nu_{chan}$ is the frequency channel resolution, t_{samp} is the sampling rate, and t_{int} is the integration time. Since for some long-going surveys technical parameters changed since their launch, the table gives the most up-to-date ones.

Survey	AO 327 drift-scan	GBNCC
Telescope	Arecibo	GBT
Start date	2003	2009
Sky coverage, δ	$-1^\circ < \delta < +38^\circ$	$\delta > -45^\circ$
t_{int}, s	60	120
Receiver	327 MHz receiver	350 MHz receiver
Backend	WAPP/Mock/PUPPI	GUPPI
f_c, MHz	327	350
Bandwidth, MHz	25/57/69	100
$\Delta\nu_{chan}$, MHz	0.049/0.056/0.025	0.024
Number of channels	512/1024/2816	4096
t_{samp}, μs	256/125/82	81.92
DM searched, pc cm^{-3}	0-1000	0-3000

[α] The central frequency was increased to 1420 MHz in 2005 to reduce the influence of interference.

Chapter 3

The High Time Resolution Universe pulsar survey

The work presented in this chapter is a part of the long-term ambitious project on searching for new pulsars in the celestial Northern hemisphere with the 100-m Effelsberg telescope. For over four years I was the leading scientist of the project responsible for planning and performing observations, processing and storing the data, testing new software and analysing the obtained results. I am the first author of the survey paper (in prep.) based on the results described below.

The full author list of the paper "The Northern High Time Resolution Universe pulsar survey - II. Initial results from the Low-Latitude survey" to be submitted to Monthly Notices of the Royal Astronomical Society is:
***Berezina M.**, Champion D. J., Spitler L., Kramer M., Martinez J. G., Eatough R. P., Karuppusamy R.*

3.1 Introduction to HTRU-NORTH

The Northern High Time Resolution Universe (hereafter – HTRU-North) pulsar survey is an on-going blind hunt for radio pulsars and transients being held with the 100-m Effelsberg radio telescope. Started in 2010 as a counterpart of the HTRU-South (Keith et al., 2010) conducted with the 64-m Parkes radio telescope, the survey aims to cover the whole Northern sky at the L-band for the first time. The HTRU-North utilizes the 7-pixel multibeam receiver whose 300-MHz passband is split into 512 channels and centred around 1.36 GHz. This high observing frequency, being less influenced by the effects of the interstellar medium (than lower frequencies), allows probing deeper into the Galaxy. Coupled with high time (54 μs) and frequency resolution (0.586 MHz) provided by a polyphase filterbank system, it enables searching for short-period distant pulsars, in particular, for the most interesting binary millisecond pulsars.

The HTRU-North sky is divided into three regions distinguished by the Galactic latitudes: low-lat $|b| < 3.5°$, mid-lat $|b| < 15°$ and high-lat $|b| > 15°$ (see Fig 3.1). Each pointing has a different integration time depending on the region where it is located. As can be seen from Fig. 3.2, different Galactic latitudes are observed to host different number of pulsars and differentiate particular kinds of pulsars.

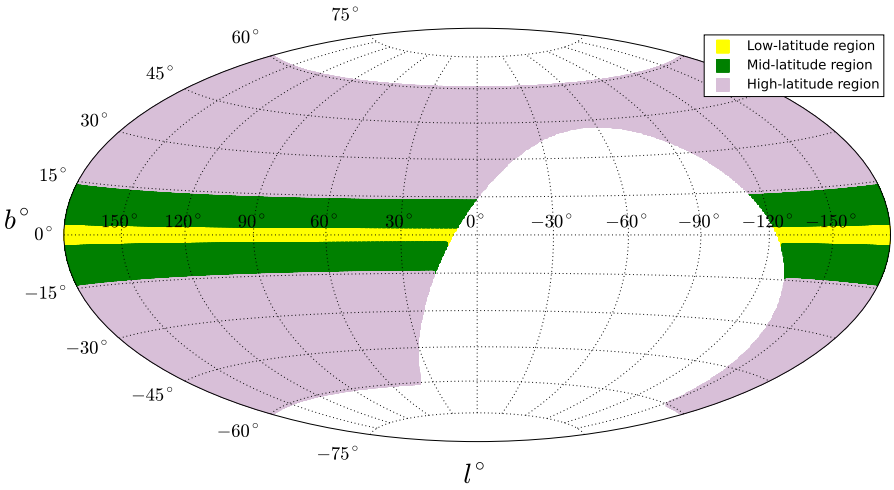

Figure 3.1: The HTRU-North sky. Plotted in the manner of (Barr et al., 2013). The white areas denote regions of sky not observable from Effelsberg location.

The longest-integrated low-lat pointings (25 minutes) should allow us to probe deeply in the Galactic plane in search of faint massive binaries, possibly turning to be double neutron stars or some exotic objects such as black hole-pulsar systems, which are not expected to migrate far from their birthplace. 3-minute mid-latitude integrations are supposed to uncover bright millisecond pulsars (MSPs) wandering above the plane. Since the medium-latitude region includes the low-latitude region, we also perform a 3-minute sweep of the Galactic plane (low-lat) in a shallow hunt for bright normal pulsars. Finally, 90-second scans of high latitudes, promise a rich haul of not only normal pulsars but also Galactic and extragalactic transients.

The difference in duration of data recording leads to different data size and, consequently, determines a need for specific processing algorithms for each latitude part of the survey. Table 3.1 presents the parameters for the three latitude regions.

3.2 "Current-epoch" observing strategy

Conducting a blind survey, we still have a strategical preference of what areas of the sky should be covered first. The regions near to the Galactic disk are thought to be a place where pulsars are born (Gunn & Ostriker, 1970). Due to the kicks during the supernova explosion, they may acquire large space velocities[1] and start their migration towards

[1]For example, the analysis of Verbunt et al. (2017) showed that the velocities of the known population of young pulsars can be modelled with two Maxwellian distributions: then 42% of pulsars from the data set have the average velocity of 120 km s^{-1} and 58% – have the average velocity of 540 km s^{-1}.

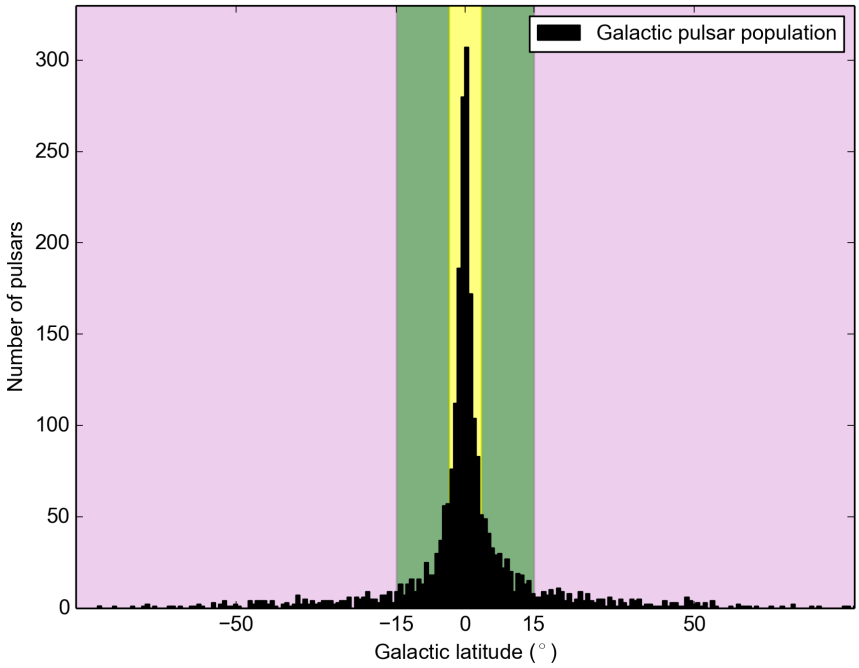

Figure 3.2: The distribution of known pulsars by Galactic latitudes. The coloured regions mark the low latitudes (yellow), medium latitudes (green) and high latitudes (purple). The data are taken from the `ATNF pulsar catalogue` and consist of 2444 pulsars. The ones in globular clusters and in the Large Magellanic Cloud are excluded from consideration.

higher latitudes.Thus, most young and energetic isolated pulsars, with characteristic ages less than 1 Myr, are found in the vicinity of the plane, whereas older isolated pulsars populate different latitudes (see Fig. 3.3). At the same time, the most massive and relativistic binaries also flock around the low latitudes (Belczynski et al., 2002) making this region a perfect target for pulsar surveys. To date, the Galactic plane is the most explored region, however, not fully covered.

In the first phase of survey observations we decided to perform a shallow sweep of the low latitudes with 3-minute integrations aiming to quickly find bright representatives of the aforementioned subspecies. This duration of a scan was considered as a good compromise between accumulating a sufficient flux and having a reasonable amount of data to store and process in a reasonable time. In the survey nomenclature every 3-minute pointing has a name made of a letter: "Z" for the low-lats and "G" for the rest of the mid-lats – followed by this pointing's 5-sign galactic longitude, ranging from 0.000 to 359.9, and 5-sign galactic latitude, ranging from −59.9 to +59.5 (for example, "G115.8+16.7"), excluding the coordinates of sky positions hidden from the Effelsberg's view. Galactic longitudes from 0 to 180° denote the direction towards the Galactic Centre, from 180 to 360° – towards the Galactic Anticentre.

Initially the choice of "Z" pointings for every single observing session was quasi-random: it was limited only by the visibility of the source at Effelsberg during the timeslot allocated for observations and a natural (and commercial) wish to use the

Table 3.1: Observational parameters for each latitude region of the HTRU-North survey. The table is taken from (Barr et al., 2013).

Survey	High	Mid	Low
Region	$\|b\| > 15°$	$\|b\| < 15°$	$\|b\| < 3.5°$
τ_{obs} (s)	90	180	1500
N_{beams}	1066135	375067	87395
T_{samp} (μs)	54	54	54
$\Delta\nu$ (MHz)	240	240	240
$\Delta\nu_{chan}$ (kHz)	585.9	585.9	585.9
N_{chans}	410	410	410
$N_{samples}$ ($\times 10^6$)	1.6	3.3	27.4
Data/beam (GB)	0.8	1.6	13.4
Data (total) (TB)	818.1	575.6	1117.8

* Both the bandwidth of the receiver ($\Delta\nu$) and the number of channels (N_{chans}) are given after removal of the band edges.

telescope time efficiently, i.e. to spend less time for source-to-source positioning what can be reached by observing nearby positions. This strategy has led to redetections of many known pulsars (see Section 3.5.1) but has not resulted in any new discoveries. Then we changed the strategy making it a bit more determined and extending the observing regions beyond the Galactic plane. We decided to further concentrate on the pointings poorly explored (or mostly unreachable) in the other L-band surveys (PMPS, HTRU-South and PALFA - see Section 2.3), mainly the ones with declinations higher than +30°. They could be either low-latitude or mid-latitude. Following this new strategy, we discovered six new pulsars (see Section 3.6).

In the preceding stage of the HTRU-North (Barr, 2012) 9% of the mid-latitude pointings were observed. By the end of this thesis work, with more than 1100 "telescope-hours" spent purely on-source, the total percentage of covered mid-latitude positions reached 50%, among these were 78.6% of the overall low-latitude positions. Fig. 3.4 shows the current status of observations.

3.3 Instrumentation and data acquisition process

The HTRU-North data are obtained with the 21-cm multi-beam receiver comprised of seven waveguide feed horns corresponding to nearly circular beams on the sky[2] The outer beams are placed in a hexagonal pattern around the central beam (Fig. 3.5a). The outer horns have a half-power beamwidth of 0.166°, the central one – 0.16° and the beams are separated by 0.25° from each other. This geometry allows to tile the

[2]http://www3.mpifr-bonn.mpg.de/div/electronic/content/receivers/21cm/report.html provides more technical details.

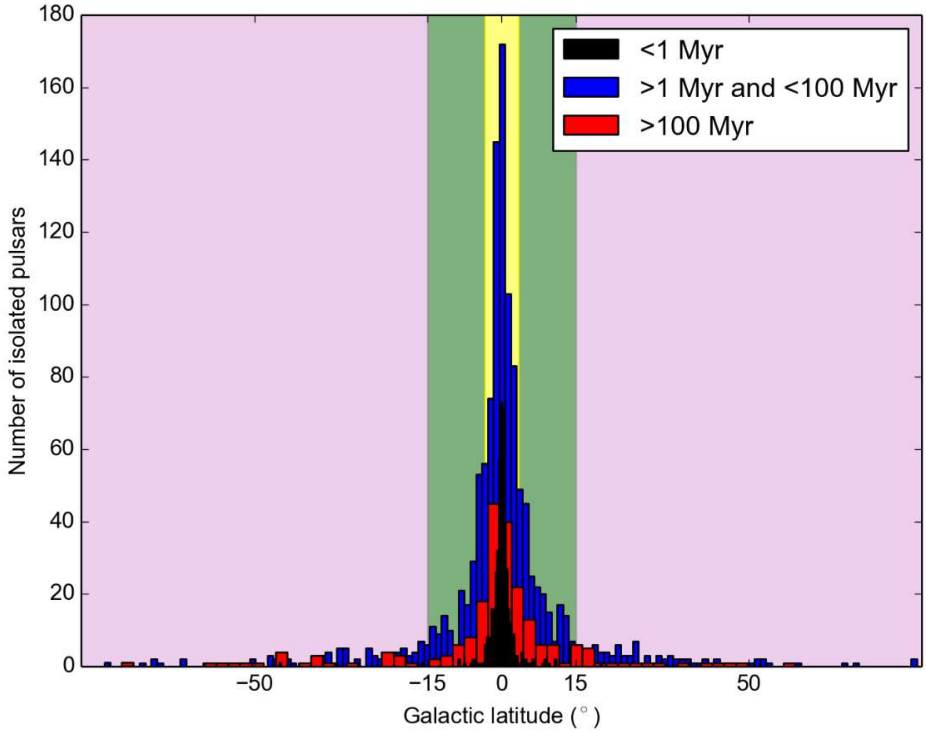

Figure 3.3: The distribution of known isolated pulsars of different ages by Galactic latitudes. The coloured regions mark the low latitudes (yellow), medium latitudes (green) and high latitudes (purple). The data are taken from the `ATNF pulsar catalogue` and consist of 1888 isolated pulsars for which the characteristic ages are reported. The ones in globular clusters and in the Large Magellanic Cloud are excluded from consideration.

whole Northern sky with 218371 pointings (1528597 beams) without leaving any gaps. Each of the horns outputs two orthogonally polarised signals: right- and left-hand circular for the central horn and linear (horizontal and vertical) for the outer ones. The further signal path follows the standard routine described in Section 2.1. The 14 signals pass through extreme low-noise amplifiers and filters (see Fig. 3.5b) what limits the original 300-MHz bandwidth centred around 1.36 GHz to 1240–1480 MHz and then enter a down-converter that shifts the band to the intermediate frequency (IF) range of 80–220 MHz. After being transported to the backend the IF signals undergo digitisation.

The FPGA-based Pulsar Fast Fourier Transform Spectrometer (PFFTS) backend (Klein et al., 2012) utilizes a polyphase filterbank algorithm enabling a nearly loss-less obtaining of power spectra. In the result, the effective bandwidth of 240 MHz is split into 410 frequency channels, each of 586 kHz width, sampled at 54 μs, and 32-bit floating-point raw-data files in the native PFFTS format are recorded on one of three machines called OBELIXes.

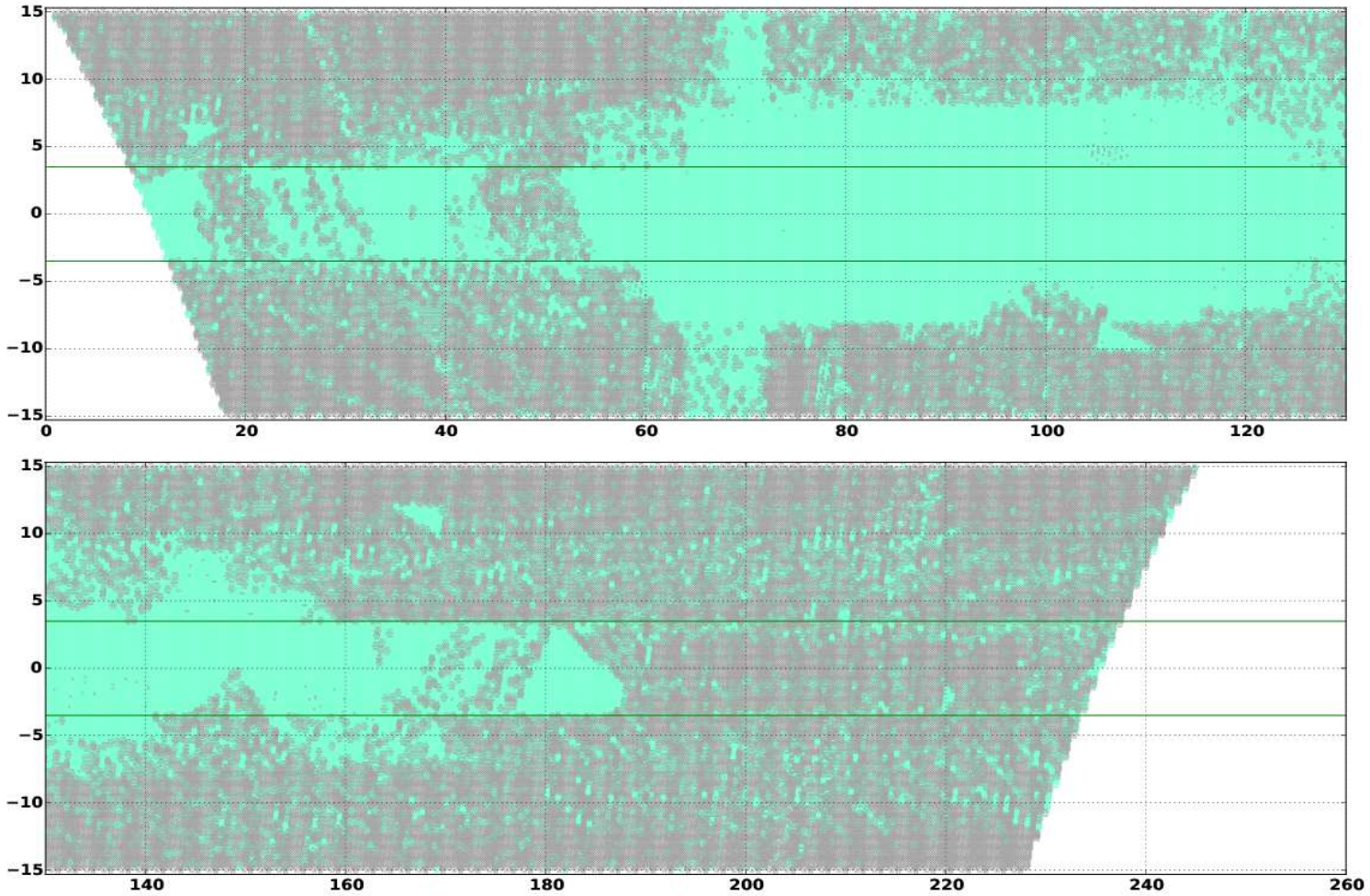

Figure 3.4: The HTRU-North sky coverage as of October 2017. The 7-beam pointings are represented in the actual size, with green areas denoting sky positions observed and processed in the FAST PIPELINE and gray areas – not observed positions. White areas correspond to the regions of the sky not visible from Effelsberg. The green horizontal lines constrain the low-lat region.

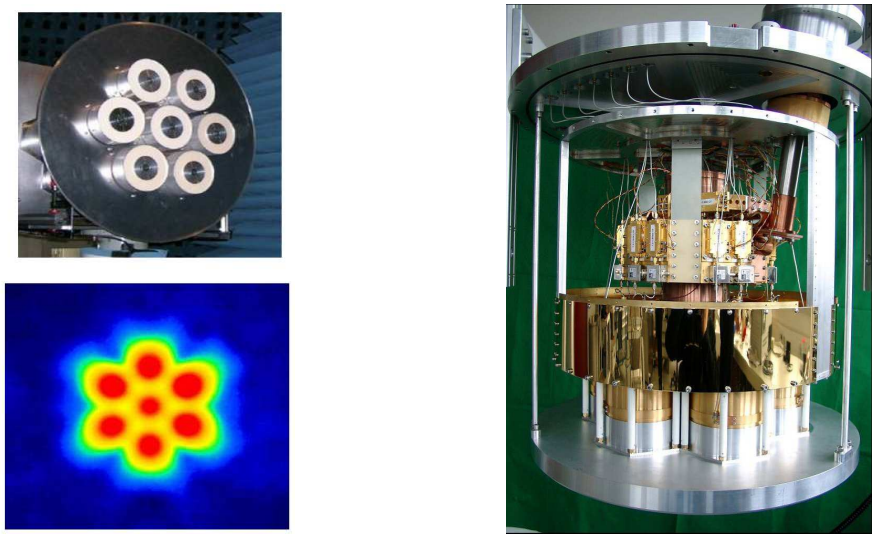

(a) (b)

Figure 3.5: The 7-pixel 21-cm receiver installed at the primary focus of the 100-m Effelsberg telescope: (a) the hexagonal beam pattern and (b) the view inside. Image credit: MPIfR.

3.4 Data processing

3.4.1 Pre-processing

Upon completion of observations, the 32-bit PFFTS data recorded to OBELIXes are converted to 8-bit filterbank files with the software `421`[3]. Apart from conversion, this program prepares the data for further processing, in particular, RFI removal. For this the data in each frequency channel are checked on the presence of strong spikes in the time domain: if the power in any time sample exceeds 3σ (standard deviations) above the normalized mean of this particular channel, this time sample is clipped (with assignment of a new value equal 3σ). The time–frequency map of "bad" data points identified during this process is written into a mask file (".mask"). Further, if the average power levels of some channels are greater than 3σ above the normalised mean across the 32-bit bandpass, these channels are flagged as "bad". The information about "bad" channels is also written into a separate (".badchannel") file. In addition, we store the original 32-bit bandpass. The resultant filtebank files, together with the additional files, are transferred to another machine called PANORAMIX (an on-site computer at Effelsberg) for offline processing and further archiving. At this step the original 32-bit PFFTS data can be deleted to free space for new observations.

[3]written by Kejia Lee

3.4.2 RFI mitigation

Since many spurious terrestrial signals are expected to be present in the recorded HTRU-North data in a variety of forms and manifestations, multi-level RFI excision should be performed prior to searching for the desired pulsar periodicities. This is done as follows. At the first step, the "bad" channels identified during the pre-processing stage are replaced with zeroes. The further RFI treatment exploits the benefits provided by the multibeam system. Unlike the majority of genuine pulsars[4], man-made interference often appears in more than one beam. This fact can be used to detect and mitigate against impulsive RFI that can be hard to spot by other techniques.

The seven servers of the PFFTS backend do not start recording simultaneously – as a result, this leads to random time offsets between the data sequences from different beams. To be able to use multibeam methods, it is necessary to get rid of these offsets. Thus, to determine the absolute starting point for these sequences, we cross-correlate the masks created for different beams. The efficiency of the cross-correlation is higher when a stronger multi-beam RFI feature is present in the data. After the time lags have been compensated for, each data point (in filterbank files) is inspected in the multibeam–time–frequency space. If a time sample has a significance equal to or exceeding 1.5σ in four or more beams, it is marked as "affected". A new value is assigned to this time sample (it will be replaced with Gaussian noise having characteristics of the surrounding "non-affected" data) and stored for further usage. Such analysis performed for all time samples in all frequency channels results in a multi-beam time–frequency map of "bad" points. Using this map, we modify the original data in the following way:

1) if a particular channel (in this map) has more than 0.2% "bad" time samples, it is zeroed;

2) if a particular time sample (in this map) "behaves bad" in more than 10% of channels, its value is replaced with Gaussian noise in all these channels (if not already zeroed at the previous steps).

In terminology of the HTRU-North processing this procedure is called multibeam masking and the resultant (modified) files are called masked files.

The next parameter space to be explored is the Fourier domain, where periodic terrestrial signals, sometimes called *birdies*, can be identified. For this the masked filterbank files (for all the beams) are dedispersed at 0 DM and the resultant time series are searched for periodicities. If some particular Fourier frequencies are found to be "active" in four or more beams (with power levels in the corresponding bins greater than or equal 2σ as calculated for the normalised data), these frequencies are considered to be RFI. The whole "flock" of discovered birdies is then written into a *zaplist* which will be applied to the data during the periodicity search, preventing the pipeline from outputting these frequencies as potential pulsar candidates.

[4]Very bright pulsars can sometimes be found in two or even three beams, mostly adjacent, depending on the exact position within the beam pattern.

3.4.3 FAST PIPELINE and candidate inspection

After passing through RFI excision, the data enter the so-called FAST PIPELINE[5] where they are processed according to a typical pulsar searching scheme described in Chapter 2, apart from acceleration search. Originally this pipeline was designed as a temporary solution for dealing with large amounts of 3-minute mid-latitude data almost in real time but with a presumably reduced sensitivity. However, it demonstrated a high efficiency and became the main processing tool for a few years when the available computational resources did not allow performing full (acceleration) search. To increase the processing speed, the pipeline operates on the low-resolution version of the data – downsampled by factors of four in time and two in frequency. These downsampled data are dedispersed at 406 trial DM values in the range 0–2975 pc cm^{-3}. The corresponding time series are further Fourier-transformed and the resultant power spectra are harmonically summed and searched for significant peaks[6]. The outcome lists of suspects are sifted based on S/N, DM and harmonic relations between the candidates. Of the sifted candidates, we fold (with `prepfold` utilite from `PRESTO`) the ones with significance greater than 8σ, as well as, the top 50 candidates with significance greater than 6σ. The final results are inspected visually using the graphical tool `QuickDirtyPlotter`[7] where candidates can be plotted in various parameter spaces (e.g. sigma–DM, sigma–period, period–DM, etc.), what enables a multi-faceted approach to elimination of spurious periodicities. As an additional ranking parameter, a euristic PEACE score (Lee et al., 2013) is calculated for each candidate: this is a linear combination of six numerical quality factors (the folded S/N, the pulse width, the topocentric period, the persistence of the signal in the radio frequency and time domains and the ratio between the pulse width and the DM smearing time) which characterize candidate's "pulsar-likeness". From our experience (of looking at a few hundred thousands `prepfold` plots), examining the PEACE score–sigma plane is the quickest way to identify pulsars among the noise and RFI. After visual inspection, the best suspects are manually folded, allowing for a slight optimisation of the discovery parameters. If the periodicity looks convincing, the corresponding pointing is included into the observing schedule for confirmation with the Effelsberg telescope.

3.4.4 Acceleration search

Apart from the FAST PIPELINE, two other (full) pipelines, with implemented acceleration search, were used for some portions of data. The first full pipeline was CPU-based and operated on the nodes of the VLBI computing cluster of the Max Planck Institute for Radio Astronomy. Probing 3240 DM values in the range (0,978) pc cm^{-3} and performing acceleration search in the range (−250,250) m s^{-2} by trying up to 27 drifted Fourier bins, it took up to one day to process 3–5 survey pointings using the

[5] developed by Ewan Barr (Barr, 2012)

[6] It should be noted that apart from periodicity search the FAST PIPELINE provides an opportunity for performing single-pulse search, however, this was not considered as a part of the present work.

[7] written by E. Barr

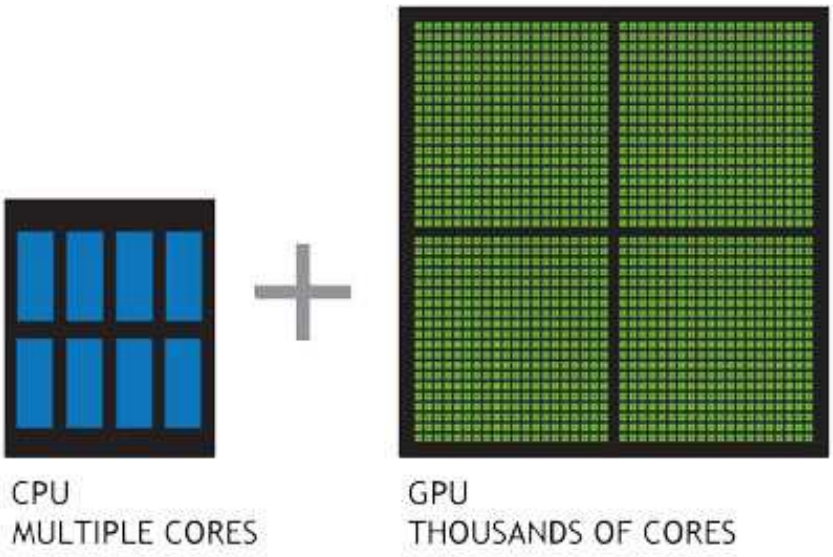

Figure 3.6: CPU vs GPU. Image credit: NVIDIA.

power of 12 nodes, if all of them were available. However, the performance of the nodes was not very stable. A few hundreds of mid-latitude pointings were processed with this pipeline (within this thesis project) before the reconstruction of the cluster made us suspend further work. At nearly the same time we started considering the possibility of changing direction from CPU to GPU[8] processing and making collaboration for developing a new, GPU-based full pipeline.

3.4.5 Acceleration search: a first try of GPU processing

For a long time the advances in data processing have been made at the expense of the increasing performance of CPUs. This was governed by a steady increase in transistor counts and processor frequencies. However, in recent years the CPU clock rate curve got close to its saturation level (being flattened out), declaring the necessity for another approach to keeping the throughput growing. The solution was found in adding extra cores to processor dies (integrated circuits). The success of multi-core CPU processors redirected the overall concept from sequential performance to multi-threading (and a more efficient use of resources). However, a real paradigm shift happened with the deployment of GPUs. Originally developed to off-load CPUs from resource-consuming 3D graphics computations, GPUs enclose thousands of cores enabling simultaneous performing of multiple tasks within a parallel architecture (see Fig. 3.6). Since a large number of computationally expensive problems, like, for example, Discrete Fourier Transform calculation, can be easily parallelised, the usage of GPU platforms offers incredible opportunities for speeding-up the results. In a particular case of pulsar searching whose specifics suggests plenty of room for multi-threaded computing the

[8] graphics processing units (GPU)

implementation of GPU-based pipelines not only promises achievement of over-real-time processing speeds but also empowers a more profound use of the data. Indeed, both dedispersion and acceleration search allow independent calculations for every trial value what means that having more jobs running in parallel, it is possible to try a wider range of DM and accelerations, thus, rising the survey sensitivity to exotic systems.

The counterpart HTRU-South survey was among the first to probe the potential of GPUs (Barsdell et al., 2010) with the development of the GPU-based version of dedispersion algorithm executed on NVIDIA's CUDA platform. The results of testing this new pipeline were reported by (Barsdell et al., 2012) emphasizing a reduced processing time: from 20 minutes to 2.5 minutes what for a 10 minute observation.

To explore the perspectives of using GPUs for the HTRU-North survey, in autumn 2014 we started a collaboration with the Jülich Research Centre hosting one of the largest supercomputers in Europe. Four GPU-nodes of the prototype cluster Juropa3, each equipped with two Kepler GPU cards, were allocated for the survey needs. A new pulsar searching software called `PEASOUP`[9] was written by Ewan Barr. With this software a search for periodicity was performed on masked filterbank data files trying 1400 DM values in the range of 0 to 3000 pc cm^{-3} and 64 possible acceleration values in the range of 0 to 1500 m/s^2. These numbers of trials were chosen to test the speed of processing and were used for most of the data though, in principle, the range of values can be tuned. Typically it took up to 6 minutes to process one beam on one node. In the result, for every "beam" of data the pipeline generated a list of 1000 candidates having the highest ranks. Every candidate was characterised by the spin period, DM and acceleration values, as well as the S/N at which this periodicity was detected. In the next step, the lists of candidates together with the corresponding full-resolution filterbank files were transferred to the VLBI cluster in Bonn (previously used for the FULL PIPELINE) where 75 most promising candidates were then chosen and folded with `prepfold` software using 20 CPU computing nodes. The final diagnostic plots were sifted through using the artificial intelligence technique of image pattern recognition PICS AI (Zhu et al., 2014) or/and viewed by eye.

In total, by June 2015, 17.1% of the available mid-latitude data (18444 beams out of 108024) comprising observations from 31 different MJD epochs have been processed with the GPU pipeline[10]. Despite the extremely fast processing rates, we had to suspend this project due to non-detection of several known pulsars. The pipeline demonstrated a good detection performance for the majority of known pulsars in the data, even for millisecond pulsars like PSR J1937+21 (Ashworth et al., 1983): in total, 54 known pulsars were redetected in PEASOUP processing. However, it seemed to be not sensitive to some weak long-period distant pulsars whose narrow profiles were still recognizable by eye on diagnostic plots created by the FAST PIPELINE. Since PEASOUP was successfully used in the southern hemisphere project SUPERB (Keane et al., 2018) on 2-bit filterbank files, the most plausible explanation for its limited effectiveness for the HTRU-North 8-bit data maybe related to the bit difference and

[9] https://github.com/ewanbarr/peasoup

[10] Here "GPU running days" are not equal to calendar days and the time for data transfer and maintaining works on the experimental cluster should be taken into account.

RFI environments. In particular, strong RFI affects search data differently depending upon the dynamic range (e.g. clipping and saturation). In order not to miss new discoveries, we decided to go back to CPU processing with the FAST pipeline because of its verified reliability and a sufficiently high sensitivity.

3.5 Survey's sensitivity analysis

A quantitative expression of the survey's sensitivity can be obtained in terms of the minimum detectable flux density, as given by the radiometer equation (see e.g. Lorimer & Kramer, 2012):

$$S_{\rm min} = \beta \frac{S/N_{\rm min} T_{\rm sys}}{G\sqrt{n_p t_{\rm obs} \Delta f}} \left(\frac{\delta}{1-\delta}\right)^{\frac{1}{2}}, \tag{3.1}$$

here $\beta = 1.05$ is the signal degradation due to 8-bit digitisation, $T_{\rm sys}$ is the system temperature of the receiver ($T_{\rm sys} = T_{\rm rec} + T_{\rm sky}$). In the case of the 7-beam receiver installed at the Effelsberg telescope $T_{\rm rec} = 21$ K for the central beam and $T_{\rm rec} = 21-30$ K for the outer beams[11]. G = 1.5 K Jy^{-1} is the antenna gain of the telescope at 1.36 GHz, δ is the pulse duty cycle, $t_{\rm obs}$ is the observation length, $\Delta f = 240$ MHz is the effective bandwidth of the receiver and $n_p = 2$ is the number of polarisations summed. The factor $S/N_{\rm min}$ is the minimum signal-to-noise ratio (S/N) sufficient for a confident detection[12]. In the idealised case of dominating white noise, the false alarm statistics calculations (see e.g. Lorimer & Kramer, 2012) give $S/N_{\rm min} = 8$. This value is widely used in theoretical estimates of sensitivities of different surveys. For example, the theoretical curves demonstrating the dependence of the minimum detectable flux density on the pulse period for the case of the HTRU-North mid-lat assuming $S/N_{\rm min} = 8$ are plotted in Fig. 3.7. However, in reality the presence of RFI and non-whiteness of the spectrum raise the threshold.

To estimate the true survey sensitivity, we performed an analysis of known pulsar redetections. For this we used the information from the `ATNF pulsar catalogue` to create a list of known pulsars that could potentially appear in the mid-lat data taken by that time (all 50%). A pulsar was put on the list if it had:

1) a reported reference pulse width (W50) and a flux density at 1400 MHz (S1400);

2) the sky position within one beamwidth from an observed pointing[13].

Using the radiometer equation Eq. 3.1, the HTRU-North parameters, the sky temperature model of Haslam et al. (1982) and the pulsar parameters from the `ATNF pulsar catalogue`, we calculated the expected S/Ns for the all the sources fulfilling the aforementioned requirements. To account for the flux density scaling with the

[11] The values of $T_{\rm rec}$ for different feed horns used in this work vary by 10–20% as they highly depend on environmental conditions, such as airmass (via elevation) and ground radiation (priv.com. with Benjamin Winkel).

[12] Using the terminology of pulsar astronomy, this is the "folded" S/N which is calculated in the time domain. It should be distinguished from the so-called "spectral" S/N which is determined by the amplitudes of harmonics in the power spectrum and usually used for building the candidates' hierarchy.

[13] Theoretically the beam pattern is assumed to be Gaussian within this distance. However, the beam shape may experience distortions from gaussianity further away from the beam centre.

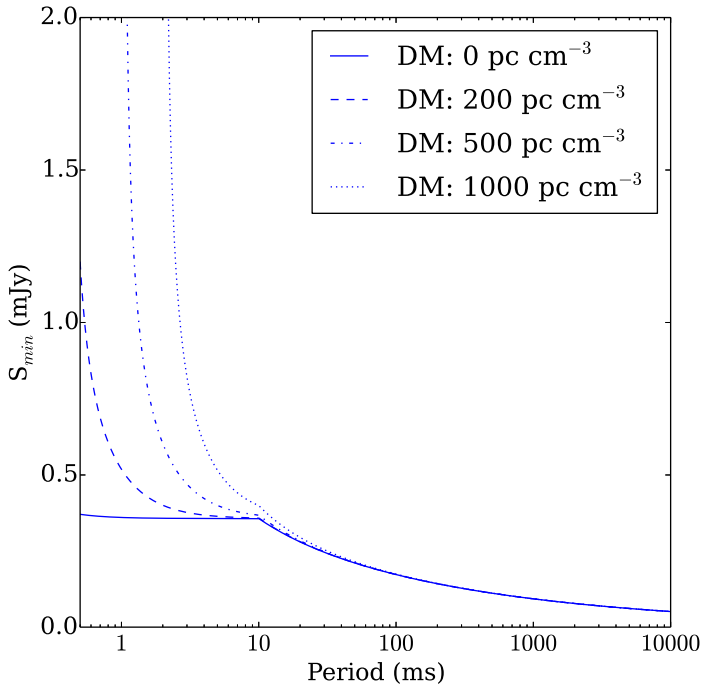

Figure 3.7: Theoretical dependence of minimum detectable flux density on spin period as calculated from Eq. 3.1 for the mid-latitude region. The curves correspond to different DM values: 0, 200, 500, 1000 pc cm^{-3}. Here we assume $T_{\rm sky} = 8$ K and $S/N_{\rm min} = 8$.

distance from the beam centre, the S/Ns were multiplied by an offset factor assuming a Gaussian beam shape. Of all possible redetections, we chose 202 pulsars with an expected S/Ns higher than 13. This S/N value was chosen empirically to account for possible detrimental influence of RFI.

Next, each survey pointing potentially containing a pulsar (or several pulsars) from the list was checked in two ways:

1) whether the pulsar/pulsars had been detected during the processing of the corresponding HTRU-North pointings with the FAST PIPELINE and, if detected, with which signal-to-noise ratio, "S/N FP";

2) whether the pulsar/pulsars had been detected after separately folding the original filterbank files with the best available ephemerides from the `ATNF pulsar catalogue` and, if detected, with which signal-to-noise ratio, "S/N refolded".

We summarize these results in two tables (see Table 3.2 and 3.3) and further analyze the confirmed redetections and non-detections separately.

3.5.1 Known pulsar redetections

A total of 165 known pulsars from the list were redetected in the survey. Among them, 41 pulsars were missed by the FAST PIPELINE (FP-missed) but showed up

in the refolding. The majority of these FP-missed pulsars demonstrated low refolded S/N values, mostly concentrated in the range from 5.7 to 14.2. Thus, in reality, they were either not sufficiently bright for being found in the periodicity search with the FAST PIPELINE and/or the data were of poor quality, with a high degree of RFI contamination. For such data the chances of detection were higher in the case of refolding since all the refolded files were visually inspected and manually cleaned with `pazi` utilite from `psrchive`[14], if necessary, whereas during the processing with the FAST PIPELINE only the built-in automatic algorithms of RFI rejection were used. These algorithms could be not sufficiently sensitive to some types of RFI.

A few "just-above-the-threshold" refolded S/N values (from 14.2 to 16.6) were obtained for long-period pulsars (PSR J1851−0053 with $P = 1.409$ s, PSR J1839-1238 with $P = 1.911$ s and PSR J1830−1135 with $P = 6.221$ s) whose detection in the Fourier domain searches may be hampered due to the presence of red noise. This might be one of the reasons why they have been missed despite looking potentially detectable. Another reason is that, for the case of long-period pulsars, a 180-second integration may contain less than a hundred pulses resulting in insufficient power per Fourier bin, if the pulse-to-pulse variability is taken into account. The same is probably true for two bright exceptions PSR J1837−0045 ($P = 0.617$ s) and PSR J1852−0635 ($P = 0.524$ s) that were missed by the FAST PIPELINE but showed up in the refolding with the S/N close to that expected.

Another 4 pulsars – PSR J1915+0738, PSR J1850−0026, PSR J1905+0616[15] and PSR J1839−0643 – were found with the FAST PIPELINE in their harmonics. The full list of the redetections' parameters, including the expected and obtained S/Ns (both for the FAST PIPELINE and refolding) are provided in Table 3.2. As can be seen, the "S/N FP" in most cases differs a lot from the "S/N expected". The lowest "S/N FP"= 4.59 is found for PSR J0540+3207 whereas its "S/N expected" is 15.87. Unsurprisingly, "S/Ns refolded", in general, match better to "S/Ns expected".

Since all seven beams hosted redetections, we decided to analyze the individual sensitivity provided by each feed horn. For each beam we plotted the ratio of the S/N expected to the S/N refolded (called $\mathrm{SNR_{exp}/SNR_{obs}}$ on the plots) as a function of the pulsar's positional offset from the beam centre. The plots of individual beams were combined into the Effelsberg 7-beam pattern (see Fig. 3.8). On these plots the black unit line, apparently, represents the one-to-one correspondence between $\mathrm{SNR_{exp}}$ and $\mathrm{SNR_{obs}}$. The dashed red line represents the weighted average of the ratio $\mathrm{SNR_{exp}/SNR_{obs}}$ calculated using the statistics from all redetections made in the corresponding beam. As can be seen, for beam 0 and beam 5 the weighted average is close to unity, thus, the sensitivity is close to the theoretically expected one. In the case of beam 1 and beam 4 the weighted average slightly deviates from unity, being around 1.25. For beam 6 it is 1.45. Beam 2 and beam 3 exhibit the highest deviation from the theoretically expected sensitivity with the weighted averages of 1.55 and 1.6 respec-

[14] http://psrchive.sourceforge.net/, (van Straten et al., 2012)

[15] The pulsar was detected in harmonics at the beam edge of one pointing, and it was also properly detected at fundamental frequency in another pointing where it was located slightly closer to the beam centre.

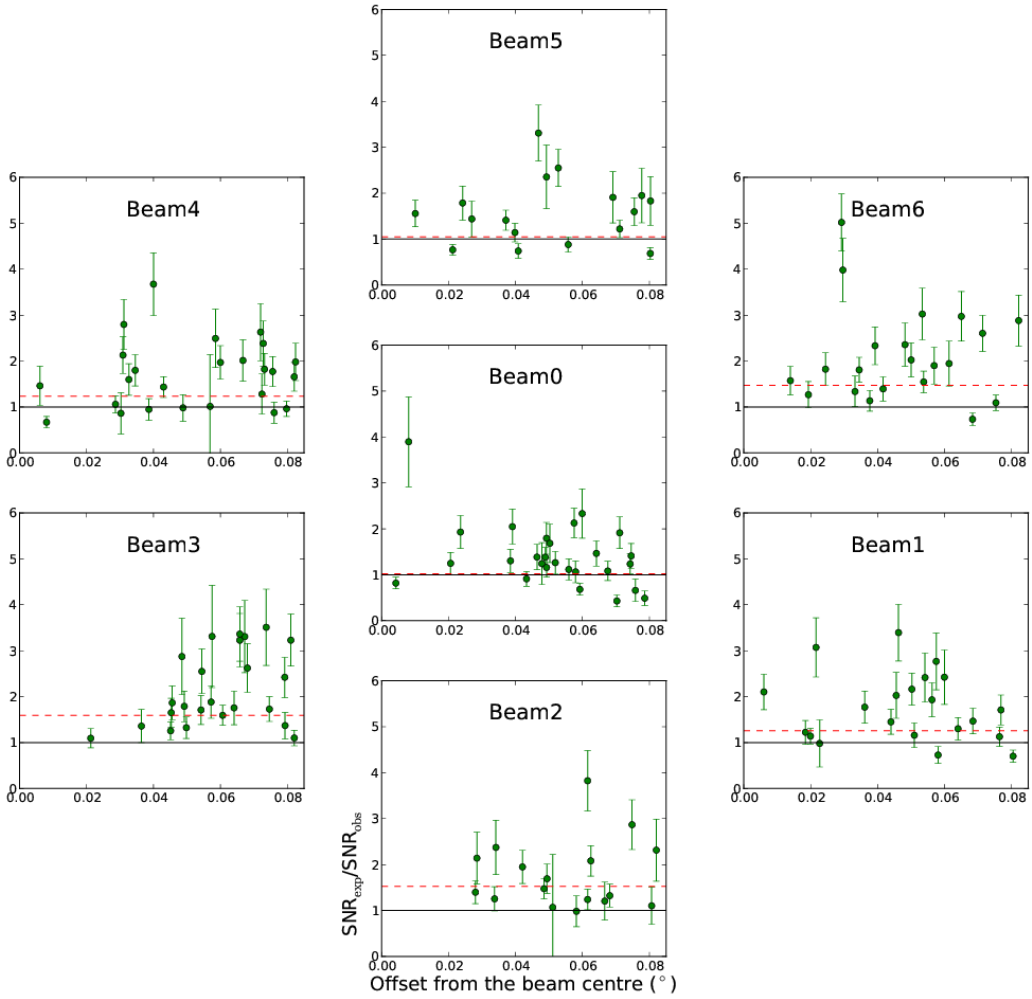

Figure 3.8: Comparison between the expected and obtained signal-to-noise ratios for a sample of known pulsars blindly redetected in the HTRU-North survey. Here SNR_{exp} is the expected S/N calculated according to Eq. 3.1, SNR_{obs} is the S/N obtained after refolding the survey filterbank files with the ephemeris from the `ATNF pulsar catalogue`. The ratio SNR_{exp}/SNR_{obs} is plotted for each beam of the HTRU-North 7-beam pattern (for a set of pulsars detected in that beam). In each beam plot: the black solid line represents unity, the red dotted line represents the weighted average of SNR_{exp}/SNR_{obs} calculated for the corresponding beam.

tively. Using all these values to calculate the average deviation in sensitivity for the whole system, we get $\mathrm{SNR}_{\mathrm{exp}}/\mathrm{SNR}_{\mathrm{obs}_{\mathrm{sys}}}$=1.3. Thus, we can conclude that our system is 1.3 times less sensitive than we expected.

3.5.2 Missed known pulsars

37 known pulsars were missed both in the FAST PIPELINE and further folding with the ephemeris from the `ATNF pulsar catalogue`. Table 3.3 contains the detailed information about this set of sources with a possible explanation for every non-detection. Most of these pulsars (29) appeared to be below our real sensitivity threshold: for some of them the expected S/N values, if taken with the uncertainties, may fall below 13. Moreover, the difficulties with determining T_{rec} and, consequently, T_{sys}, precisely for every observation imply underestimated uncertainties. Other reasons for non-detection are likely to be a strong RFI and red noise. These factors may be particularly responsible for missing long-period pulsars ($P > 1$ s) whose expected S/Ns exceed 20. A few pulsars with low DMs were not seen, most probably, due to scintillation. Finally, some "non-trivial" sources such as: X-ray pulsars PSR J1809−1943 and PSR J1832−0836, a young pulsar in a relativistic binary PSR J1906+0746 and PSR J1916+0748 known to exhibit giant pulses were not expected to show up in the (quick) periodicity search of this survey.

3.6 New discoveries and detection rate

Quick processing of 41% of the HTRU-North mid-lat data taken within this thesis project has resulted in detection of six new pulsars (see Fig. 3.9 for pulse profiles and Table 3.4 for measured parameters). One of them, PSR J2327+6241, also showed up in the 350-MHz data of the GBNCC survey (Stovall et al., 2014), nearly at the same time as it was detected in HTRU-North (from priv. com.). Also, when looking at the results produced by the FAST PIPELINE, we found a number of pulsars (see Table 3.5) that have been discovered and published by other surveys since the beginning of the HRTU-North. Though these sources were first discovered by other surveys and we did not follow them up, we include them in the overall HTRU-North yield to obtain a more complete picture of the survey's performance, giving a total of 15 newly and co-discovered pulsars.

Upon the discovery, the six "brand-new" pulsars were confirmed with the Effelsberg telescope. PSR J2045+3633 and PSR J2053+4650, appeared to be in binary systems (see Chapter 4 for a detailed study of these pulsars), while the other four were isolated. Further, to measure their spin and astrometric parameters more precisely, we performed follow-up timing observations using different telescopes: Effelsberg and Lovell – for all six pulsars, additionally Nançay and Arecibo – for the binaries. The results of timing are presented in Table 3.4 which contains the spin and astrometric parameters of new discoveries, as well as DM values and DM-derived distances calculated according to both the `NE2001` Galactic electron density model (Cordes & Lazio, 2002) and a newer `YMW16` model (Yao et al., 2017). As can be seen, all new discoveries

have high DMs, thus, confirming that the survey meets our original goal – to use the high frequency resolution to probe deeper into the Galaxy.

Out of six, two pulsars, PSR J0100+6427 and PSR J2053+4650 have profiles with interpulses. Follow-up of these pulsars with full polarisation observations may yield information about their spin geometry, thus, contributing to our understanding of the emission mechanism. PSR J1951+4721 has a relatively high $\dot{P}$ indicating that it is reasonably young ($\tau_c < 100$ kyr) and energetic ($\dot{E} = 4.4 \times 10^{33}\,\mathrm{erg\,s^{-1}}$). A fold of Fermi LAT data at this position did not show any γ-ray counterpart. However, the large estimated distance of 6–9 kpc (depending on the Galactic electron density model) and modest $\dot{E}$ make the detection at these high energies hard, thus, a non-detection is not constraining.

The results of the quick processing show that the survey is less sensitive than expected. The initial estimates obtained by Barr et al. (2013) with `PSRPOP`[16] software suggested that as many as 71 new non-MSPs and 20 MSPs would be discovered in a 50% mid-lat run[17]. The overall (including co-detections) HTRU-North yield to-date number 27 non-MSPs and 3 MSPs, with 50% of the mid-lat covered. Though the lack of MSP discoveries is expected for the case of "quick-only" processing, i.e. on down-sampled data and without performing proper acceleration search, the lower number of non-MSP discoveries can be probably explained by several factors: the lower survey sensitivity, RFI or/and incorrect initial model assumptions.

The calculations described in Section 3.5.1 already demonstrate that the survey sensitivity is lower by a factor of ~ 1.3. In order to overcome this deficit the integration time for future mid-lat observations will need to be increased from 3 minutes to 5 minutes. Considering the overall remaining observing time, it will take 2232 hours instead of previously planned 1340 hours to finish the rest 50% of mid-lat. To reduce the load on the Effelsberg telescope, some unobserved regions can be shared (within a recently established collaboration) with the newly commissioned 500-meter FAST telescope[18]. Due to its large collecting area, it has a much higher gain allowing for much shorter integrations. The HTRU-North mid-lat will prioritize the pointings beyond the FAST's visibility.

RFI also plays a significant role in the survey's detection rate. Not only does it increase the T_{sys} of the telescope, reduce the effective bandwidth and integration time, it also causes confusion. The number of spurious candidates and their harmonics can overwhelm the number of astronomical signals pushing them down in the candidate list. The results of the quicklook can be leveraged to provide a catalogue of likely present RFI that will enable future processing to determine if similar periodicities are seen in multiple locations on the sky – ruling them out as an astronomical signal. The variable nature of RFI periodicities makes this tricky to implement but the extensive statistics gathered with the FAST PIPELINE should allow such signals to be characterised, for

[16] Lorimer et al. (2006), http://psrpop.phys.wvu.edu/

[17] At the same time it should be noticed that the issue of potential discrepancy between the observed and simulated pulsar populations has already been mentioned at the previous stage of the HTRU-North survey by E. Barr.

[18] http://fast.bao.ac.cn/en/

example, using more advanced machine learning algorithms.

Finally, since the survey was designed, a new model of the electron content of the Galaxy, `YMW16`, has been published (Yao et al., 2017). It is based on the numerous surveys that have taken place since `NE2001` was originally developed. The `YMW16` model tends to place pulsars further away from the Earth than `NE2001`. This directly affects the number of potential HTRU-North discoveries and generally reduces the overall expected yield. New discoveries and independent distance measurements will determine whether this trend portrays the overall Galactic population.

With an increased integration time and more effective RFI mitigation further survey observations will be able to show if the reduced discovery rate reflects the underlying pulsar population or the telescope sensitivity. Future processing will also include a full acceleration search due to the newly available high performance computing resources. Although the number of systems that need such a search to be discovered is low, they are likely to be the most interesting.

3.7 Conclusion

Within this work, 41% of the HTRU-North mid-lat pointings have been observed and processed with the FAST PIPELINE, bringing the total survey mid-lat coverage to 50% and leaving the total area of the sky of $\sim 7620\,\mathrm{deg}^2$ encompassed. The current epoch of the HTRU-North survey has resulted in the discovery of 6 new pulsars and co-detection of 9 pulsars that have been already published by other (same-era) surveys. Combined with 15 discoveries made by (Barr et al., 2013) in the previous HTRU-North stage, this gives a total of 30 new and co-detected pulsars. Among them, PSR J2045+3633 and PSR J2053+4650 are especially interesting: they are mildly-recycled and have companions. PSR J1951+4721 is a relatively young pulsar with a characteristic age $\tau_c < 100$ kyr.

The lower-than-expected survey yield can be partially explained by the reduced survey sensitivity as seen in our redetections of known pulsars. RFI contamination also affects our sensitivity, particularly to those with periodicities close to that of RFI but also weak pulsars elsewhere in the spectrum. Thus, development of more advanced algorithms of RFI mitigation and implementation of longer integration times should help to solve this problem in future. Finally, the new electron model of the Galaxy `YMW16` places many pulsars more distant from the Earth reducing the expected yield.

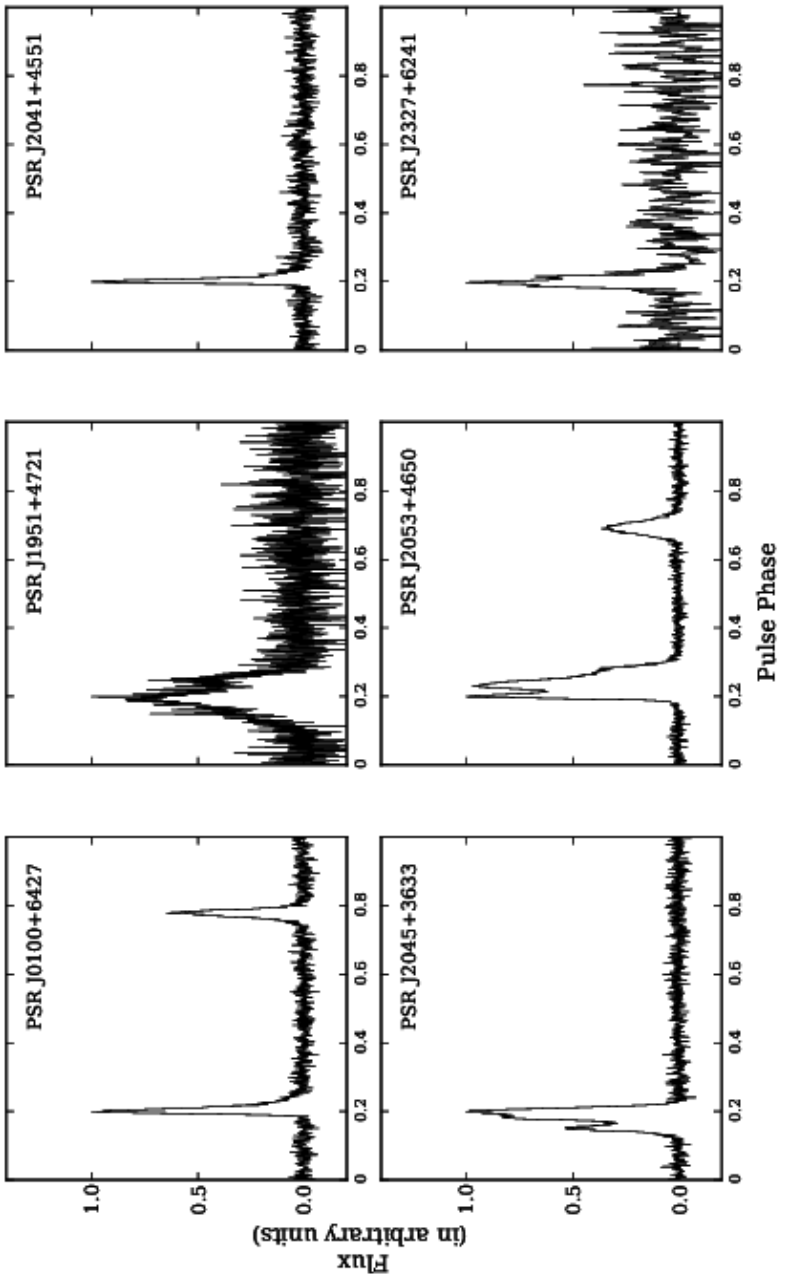

Figure 3.9: Pulse profiles for the six newly discovered pulsars of the HTRU-North survey.

Table 3.2: The HTRU-North survey redetections of 165 known pulsars. The presented parameters are: pulsar's J2000 name, spin period, dispersion measure, Galactic longitude and latitude, the name of the HTRU-North pointing where it was detected, mean flux density at 1400 MHz from the `ATNF pulsar catalogue`, pulse width at 50% of peak from the `ATNF pulsar catalogue`, expected signal-to-noise ratio (S/N) calculated according to Eq. 3.1, expected S/N error, the highest S/N obtained after refolding the observation with the best ephemeris from the `ATNF pulsar catalogue`, the offset of the correct pulsar position from the centre of the telescope beams. The corresponding units are given in the table.

PSR	Period (s)	DM (pc cm^{-3})	l (°)	b (°)	Pointing	S1400 (mJy)	W50 (ms)	S/N expected	S/Nerr expected	S/N refolded	S/N FP	Offset (°)
J0026+6320	0.318 358	230.31	120.176	0.593	Z120.3+00.8	0.057	8.1	40.57	13.64	12.25	7.49	0.057
J0040+5716	1.118 230	92.59	121.452	−5.567	G121.4−05.3	0.049	12.2	45.34	6.87	30.77	7.92	0.049
J0102+6537	1.679 160	65.85	124.080	2.773	Z124.1+02.7	0.060	89.7	33.37	7.67	14.31	8.88	0.060
J0108+6608	1.283 660	30.46	124.646	3.327	Z124.8+03.1	0.027	22.5	57.45	15.49	39.91	18.72	0.027
J0139+5814	0.272 451	73.78	129.216	−4.044	G129.3−04.1	0.074	5.2	194.95	34.17	157.83	63.15	0.074
J0141+6009	1.222 950	34.93	129.147	−2.105	Z129.0−02.4	0.058	34.9	172.51	43.59	60.59	34.39	0.058
J0147+5922	0.196 321	40.11	130.059	−2.723	Z130.1−02.5	0.079	7.0	53.17	11.22	38.79	7.93	0.079
J0147+5922	0.196 321	40.11	130.059	−2.723	Z130.0−03.0	0.073	7.0	58.56	12.36	27.74	9.40	0.073
J0406+6138	0.594 576	65.30	144.025	7.046	G144.1+06.8	0.052	18.4	119.61	20.38	72.35	32.50	0.052
J0454+5543	0.340 729	14.59	152.617	7.547	G152.5+07.7	0.039	8.1	717.67	198.92	150.73	162.52	0.039
J0502+4654	0.638 565	42.19	160.363	3.077	Z160.4+03.0	0.050	22.7	96.81	15.54	45.57	13.80	0.050
J0528+2200	3.745 540	50.94	183.856	−6.896	G184.1−06.9	0.037	185.5	346.14	94.34	230.20	69.04	0.037
J0540+3207	0.524 271	61.97	176.719	0.761	Z176.9+01.0	0.050	12.0	15.87	2.81	11.98	4.59	0.050
J0624−0424	1.039 080	70.83	213.792	−8.036	G213.6–08.2	0.049	52.0	68.57	35.95	9.05	Missed	0.049
J1709−1640	0.653 054	24.89	5.775	13.657	G005.5+13.6	0.023	10.8	294.59	153.99	299.98	279.85	0.023
J1801−1855	2.550 500	484.00	10.447	1.978	Z010.3+02.0	0.060	41.9	23.22	5.68	9.58	Missed	0.060
J1803−1857	2.864 340	392.00	10.730	1.428	Z010.6+01.2	0.061	25.6	26.43	6.62	13.59	Missed	0.061
J1805−1504	1.181 270	225.00	14.246	3.093	Z014.5+03.1	0.008	235.0	40.22	7.53	60.24	64.07	0.008
J1808−1517	0.544 549	205.00	14.472	2.239	Z014.4+02.5	0.028	21.8	14.52	2.58	10.40	Missed	0.028
J1809−1429	0.895 285	411.30	15.306	2.393	Z015.0+02.4	0.057	11.0	35.19	7.86	12.71	Missed	0.057
J1812−1733	0.538 341	518.00	12.904	0.387	Z012.9+00.4	0.049	63.0	67.91	13.07	37.86	39.36	0.049
J1814−1649	0.957 464	782.00	13.820	0.245	Z014.0+00.5	0.067	28.0	36.76	8.73	11.11	Missed	0.067
J1814−1744	3.975 910	792.00	13.021	−0.215	Z012.8–00.2	0.022	92.0	39.79	8.34	12.95	Missed	0.022
J1816−1729	0.782 313	525.50	13.433	−0.424	Z013.3–00.6	0.053	17.0	55.26	10.28	18.28	7.01	0.053
J1818−1422	0.291 489	622.00	16.405	0.610	Z016.4+00.6	0.039	19.0	221.16	41.19	108.00	69.44	0.039

J1819−0925	0.852 047	378.00	20.935	2.633	Z020.9+02.6	0.064	20.0	28.94	5.47	19.75	13.03	0.064
J1819−0925	0.852 047	378.00	20.935	2.633	Z020.9+02.9	0.075	20.0	24.23	4.58	8.45	Missed	0.075
J1819−1510	0.226 539	421.70	15.876	−0.086	Z015.6–00.1	0.054	6.9	22.79	5.06	9.43	Missed	0.054
J1820−0427	0.598 076	84.44	25.456	4.733	G025.4+04.9	0.062	11.0	306.18	55.59	247.34	232.27	0.062
J1820−1818	0.309 905	436.00	13.202	−1.720	Z013.0–01.7	0.077	16.0	23.80	4.54	13.91	11.53	0.077
J1824−1423	0.359 394	428.30	17.146	−0.796	Z017.3–00.9	0.080	9.9	22.61	6.59	12.35	6.17	0.080
J1824−1423	0.359 394	428.30	17.146	−0.796	Z017.3–01.1	0.069	9.9	26.78	7.81	14.03	8.57	0.069
J1824−1945	0.189 335	224.65	12.279	−3.106	Z012.1–03.3	0.030	2.9	322.34	55.63	80.98	66.04	0.030
J1825+0004	0.778 949	56.62	30.001	5.856	G030.3+05.8	0.006	10.3	34.62	10.13	23.71	8.76	0.006
J1825−0935	0.769 006	19.38	21.449	1.324	Z021.3+01.5	0.073	12.0	510.87	93.09	74.82	22.79	0.073
J1825−1446	0.279 187	357.00	16.805	−1.001	Z016.6–01.2	0.082	12.0	56.87	10.98	19.74	14.93	0.082
J1828−0611	0.269 415	363.20	24.780	2.279	Z024.9+02.5	0.049	10.0	43.71	8.19	24.42	13.32	0.049
J1828−1101	0.072 052	607.40	20.495	0.042	Z020.4+00.3	0.028	9.9	60.45	16.01	28.27	22.81	0.028
J1829−1751	0.307 133	217.11	14.604	−3.418	Z014.5–03.2	0.049	15.0	243.59	45.90	144.12	121.47	0.049
J1830−1059	0.405 043	161.50	20.812	−0.478	Z020.9–00.3	0.066	3.2	92.11	16.61	28.53	27.53	0.066
J1830−1135	6.221 550	257.00	20.193	−0.590	Z020.3–00.4	0.074	62.2	58.13	13.76	16.56	Missed	0.074
J1831−0823	0.612 133	245.90	23.211	0.548	Z023.4+00.7	0.054	14.0	43.09	8.20	16.90	15.53	0.054
J1832−0644	0.744 295	578.00	24.806	1.070	Z024.6+00.9	0.057	27.3	23.72	4.99	12.48	12.11	0.057
J1832−0827	0.647 293	300.87	23.272	0.298	Z023.4+00.6	0.066	7.1	117.50	20.64	34.93	15.01	0.066
J1832−0827	0.647 293	300.87	23.272	0.298	Z023.4+00.4	0.081	7.1	93.79	16.47	29.04	11.72	0.081
J1832−1021	0.330 354	475.70	21.587	−0.597	Z021.4–00.6	0.046	8.4	58.80	10.71	17.32	10.09	0.046
J1833−0559	0.483 459	353.00	25.514	1.321	Z025.3+01.4	0.051	41.4	13.84	3.24	11.93	Missed	0.051
J1833−0827	0.085 284	411.00	23.386	0.063	Z023.3–00.2	0.065	4.9	85.08	15.49	28.63	33.09	0.065
J1834−0602	0.487 914	445.00	25.640	0.965	Z025.8+00.8	0.049	16.8	30.36	8.91	12.90	Missed	0.049
J1834−1710	0.358 306	123.80	15.768	−4.206	G016.0–04.3	0.057	14.0	35.99	39.99	35.58	31.43	0.057
J1835−0643	0.305 830	472.90	25.093	0.552	Z025.1+00.6	0.046	32.0	29.32	5.83	21.17	16.18	0.046
J1836−1008	0.562 711	316.98	22.263	−1.415	Z022.4–01.6	0.047	8.7	216.03	39.83	65.29	32.63	0.047
J1837−0045	0.617 037	86.98	30.675	2.749	Z030.8+02.5	0.056	9.6	32.54	6.20	36.91	Missed: RFI	0.056
J1838−1046	1.218 350	208.00	21.862	−2.049	Z021.8–01.8	0.034	16.6	34.68	8.70	14.62	12.24	0.034
J1839−0643	0.449 548	497.90	25.547	−0.350	Z025.5–00.4	0.048	19.1	50.30	13.31	21.90	Harmonics	0.048
J1839−1238	1.911 430	169.80	20.347	−3.180	Z020.3–03.4	0.034	26.0	25.63	3.90	14.19	Missed	0.034

J1840−0559	0.859 368	321.70	26.345	−0.281	Z026.1–00.3	0.036	16.0	18.07	3.60	10.20	Missed	0.036
J1840−0809	0.955 672	349.80	24.441	−1.308	Z024.3–01.1	0.062	10.0	139.50	24.04	36.48	30.88	0.062
J1840−0815	1.096 440	233.20	24.314	−1.283	Z024.3–01.1	0.068	22.0	56.20	10.49	42.51	23.79	0.068
J1840−0840	5.309 380	272.00	24.010	−1.616	Z024.1–01.4	0.045	180.0	39.89	6.19	31.74	28.03	0.045
J1841−0157	0.663 321	475.00	30.099	1.216	Z029.9+01.2	0.064	21.0	27.15	5.15	20.85	7.19	0.064
J1841+0912	0.381 319	49.11	40.078	6.278	G040.3+06.4	0.080	7.9	61.80	10.13	24.15	37.70	0.080
J1842−0153	1.054 230	434.00	30.283	1.022	Z030.5+01.1	0.067	21.4	24.38	5.50	12.12	5.21	0.067
J1842−0359	1.839 940	195.98	28.347	0.174	Z028.5–00.1	0.041	285.0	79.72	16.80	107.46	82.09	0.041
J1842−0905	0.344 643	343.30	23.810	−2.136	Z024.0–02.1	0.076	7.7	27.44	5.10	15.49	9.02	0.076
J1843−0000	0.880 330	101.50	32.013	1.768	Z031.8+01.8	0.044	26.0	125.50	23.34	86.46	36.89	0.044
J1843−0211	2.027 520	441.70	30.084	0.768	Z030.4+00.7	0.060	24.0	54.18	10.04	27.52	21.29	0.060
J1844+00	0.460 503	345.54	32.624	1.880	Z032.4+01.9	0.006	12.0	478.88	88.42	227.66	182.02	0.006
J1844−0433	0.991 027	123.16	28.096	−0.548	Z028.4–00.6	0.040	13.0	74.46	13.92	20.27	18.94	0.040
J1844+1454	0.375 463	41.50	45.557	8.149	G045.3+08.2	0.058	9.3	67.43	17.01	92.44	20.20	0.058
J1845−0434	0.486 751	230.80	28.193	−0.785	Z028.4–00.6	0.057	17.0	55.44	10.42	29.44	17.26	0.057
J1846−0749	0.350 110	388.30	25.386	−2.431	Z025.1–02.5	0.020	7.4	20.77	3.06	18.20	7.04	0.020
J1847−0402	0.597 769	141.98	28.876	−0.939	Z028.9–01.0	0.071	22.0	123.93	22.47	64.78	58.42	0.071
J1847−0402	0.597 769	141.98	28.876	−0.939	Z029.0–00.6	0.079	22.0	107.26	19.45	44.28	16.57	0.079
J1847−0438	0.957 991	229.00	28.371	−1.268	Z028.3–01.5	0.033	11.3	37.49	9.39	28.07	6.77	0.033
J1847−0605	0.778 164	207.90	27.048	−1.867	Z027.0–01.7	0.082	13.1	28.45	8.32	12.30	Missed	0.082
J1848+0604	2.218 600	242.70	38.062	3.328	Z037.9+03.3	0.068	46.0	13.76	2.63	9.38	Missed	0.068
J1849+0127	0.542 155	207.30	34.034	1.043	Z034.0+01.1	0.050	17.0	18.94	4.72	11.24	Missed	0.050
J1849+0409	0.761 194	56.10	36.367	2.425	Z036.5+02.2	0.035	11.0	20.73	3.15	10.83	Missed	0.035
J1850−0026	0.166 634	947.00	32.407	0.066	Z032.6+00.0	0.076	13.0	30.72	4.65	15.92	Harmonics	0.076
J1850+0026	1.081 840	201.40	33.246	0.353	Z033.3+00.4	0.008	14.1	84.13	21.11	21.59	10.29	0.008
J1851−0029	0.518 721	510.00	32.542	−0.335	Z032.5–00.4	0.049	13.0	20.52	3.09	14.85	14.59	0.049
J1851−0053	1.409 070	24.00	32.100	−0.318	Z032.0–00.1	0.041	19.0	66.22	12.43	16.32	Missed	0.041
J1851+1259	1.205 300	70.61	44.513	5.932	G044.3+06.0	0.059	11.0	55.08	10.19	11.57	Missed	0.059
J1852+0013	0.957 751	545.00	33.282	−0.174	Z033.1−00.4	0.048	19.0	15.26	3.08	6.48	Missed	0.048
J1852−0127	0.428 979	431.00	31.706	−0.802	Z031.9–00.6	0.046	18.0	20.57	4.05	11.02	Missed	0.046
J1852−0635	0.524 151	171.00	27.225	−3.340	Z027.3–03.4	0.056	90.0	90.01	18.69	80.71	Missed: RFI	0.056

J1853−0004	0.101 436	438.20	33.086	−0.467	Z033.1–00.4	0.057	2.2	35.12	5.29	16.51	13.47	0.057
J1853+0505	0.905 137	279.00	37.650	1.956	Z037.6+01.9	0.079	100.0	15.58	5.00	31.86	30.25	0.079
J1853+0545	0.126 400	198.70	38.354	2.064	Z038.3+02.2	0.051	9.5	39.50	42.45	37.02	24.35	0.051
J1854+1050	0.573 197	207.20	42.887	4.223	G042.8+04.4	0.034	43.0	32.44	6.86	25.90	14.69	0.034
J1855+0527	1.393 480	362.00	38.227	1.642	Z038.1+01.4	0.029	3.0	41.35	5.08	8.24	Missed	0.029
J1857+0143	0.139 760	249.00	35.168	−0.571	Z035.4−00.6	0.049	15.7	14.99	4.43	15.29	13.65	0.049
J1857+0212	0.415 823	506.77	35.617	−0.390	Z035.5−00.2	0.042	14.0	65.46	12.15	33.61	22.85	0.042
J1857+0526	0.349 951	466.40	38.438	1.187	Z038.6+01.2	0.073	9.7	20.74	3.98	11.39	Missed	0.073
J1857+0526	0.349 951	466.40	38.438	1.187	Z038.6+01.0	0.075	9.7	20.04	3.85	12.55	Missed	0.075
J1859+00	0.559 634	420.00	34.401	−1.587	Z034.6−01.6	0.031	54.0	122.15	23.93	43.69	29.39	0.031
J1901+0156	0.288 219	105.39	35.818	−1.367	Z035.9−01.2	0.068	6.1	14.85	2.99	5.66	Missed	0.068
J1901+0254	1.299 690	185.00	36.643	−0.855	Z036.5−01.1	0.014	70.0	21.86	4.36	13.91	7.81	0.014
J1901+0331	0.655 450	402.08	37.213	−0.637	Z037.1−00.9	0.039	11.0	251.27	44.55	107.70	42.68	0.039
J1901+0716	0.643 999	252.81	40.569	1.056	Z040.4+01.0	0.076	11.0	34.73	6.52	30.76	17.42	0.076
J1902+0556	0.746 577	177.49	39.501	0.210	Z039.6+00.0	0.010	11.0	88.99	16.58	57.17	54.69	0.010
J1902+0615	0.673 503	502.90	39.814	0.336	Z039.6+00.3	0.080	24.0	27.32	5.17	38.79	8.55	0.080
J1902+0615	0.673 503	502.90	39.814	0.336	Z039.6+00.1	0.068	24.0	32.74	6.19	44.70	8.73	0.068
J1903+0135	0.729 304	245.17	35.727	−1.955	Z035.8−01.9	0.024	9.9	429.21	79.82	222.36	42.33	0.024
J1904+0004	0.139 525	233.61	34.450	−2.811	Z034.4−03.0	0.050	7.8	61.31	11.24	30.30	20.95	0.050
J1905+0600	0.441 210	730.10	39.838	−0.277	Z040.1−00.3	0.035	13.0	19.37	3.67	10.78	6.87	0.035
J1905+0616	0.989 706	256.05	40.069	−0.169	Z040.1−00.1	0.068	21.0	20.58	3.97	19.02	5.01	0.068
J1905+0616	0.989 706	256.05	40.069	−0.169	Z040.1−00.4	0.080	21.0	16.60	3.20	24.17	Harmonics	0.080
J1905+0709	0.648 040	245.34	40.944	0.065	Z040.8+00.1	0.056	39.0	47.46	9.08	24.56	10.49	0.056
J1906+0641	0.267 275	472.80	40.604	−0.304	Z040.8−00.1	0.021	18.0	55.29	10.57	50.49	38.11	0.021
J1907+0740	0.574 698	332.00	41.613	−0.102	Z041.9−00.1	0.039	13.2	21.05	5.21	22.24	10.47	0.039
J1908+0457	0.846 793	360.00	39.267	−1.468	Z039.4−01.3	0.045	42.0	30.36	5.79	18.39	9.77	0.045
J1908+0500	0.291 021	201.42	39.293	−1.403	Z039.4−01.2	0.054	3.9	45.76	8.47	26.76	6.01	0.054
J1908+0839	0.185 397	512.10	42.560	0.229	Z042.6+00.4	0.061	5.1	17.79	2.41	11.16	8.92	0.061
J1909+0254	0.989 831	171.73	37.605	−2.713	Z037.9−02.7	0.031	11.0	49.46	9.28	23.24	10.64	0.031
J1910+0225	0.337 855	209.00	37.229	−3.057	Z037.3−03.1	0.048	16.4	20.19	7.44	16.25	8.19	0.048
J1910+0358	2.330 260	82.93	38.606	−2.339	Z038.5−02.5	0.038	265.0	33.30	6.66	29.37	34.01	0.038

J1910+0714	2.712 420	124.06	41.520	−0.870	Z041.8−00.9	0.073	22.0	21.42	4.40	8.99	Missed	0.073
J1910+0714	2.712 420	124.06	41.520	−0.870	Z041.8−00.8	0.082	22.0	18.42	3.78	9.30	Missed	0.082
J1910+0728	0.325 415	283.70	41.740	−0.772	Z041.8−00.8	0.021	15.0	36.78	7.14	29.47	19.34	0.021
J1913−0440	0.825 936	89.39	31.307	−7.124	G031.3–07.1	0.059	7.5	337.85	63.83	495.60	16.03	0.059
J1913+0446	1.616 130	109.10	39.736	−2.790	Z039.6−03.0	0.024	16.0	41.45	8.14	22.75	7.70	0.024
J1913+1000	0.837 148	422.00	44.285	−0.194	Z044.3−00.2	0.038	32.0	22.05	4.24	16.92	6.51	0.038
J1913+1011	0.035 909	178.80	44.485	−0.167	Z044.3−00.2	0.046	2.1	14.49	3.56	7.15	Missed	0.046
J1914+0219	0.457 527	233.80	37.633	−4.037	G037.6−04.0	0.004	16.0	42.24	6.54	51.65	15.73	0.004
J1915+0227	0.317 306	192.60	37.825	−4.117	G037.6−04.3	0.075	7.3	20.31	3.08	18.63	7.54	0.075
J1915+0738	1.542 700	39.00	42.466	−1.803	Z042.8−01.8	0.034	11.0	32.72	6.26	20.64	Harmonics	0.034
J1915+0752	2.058 310	105.30	42.623	−1.614	Z042.8−01.8	0.024	24.0	16.72	3.48	9.36	Missed	0.024
J1916+0844	0.439 995	339.40	43.538	−1.493	Z043.4−01.7	0.042	8.3	24.29	4.55	17.43	5.49	0.042
J1916+0951	0.270 254	60.95	44.556	−1.019	Z044.6−01.0	0.075	9.6	25.30	4.82	17.93	13.27	0.075
J1920+1110	0.509 886	182.00	46.152	−1.199	Z046.4−01.2	0.059	10.2	17.71	4.53	7.11	Missed	0.059
J1921+1948	0.821 035	153.85	53.869	2.672	Z054.1+02.6	0.072	40.3	40.73	9.64	15.49	8.23	0.072
J1921+2153	1.337 300	12.44	55.777	3.501	G056.0+03.5	0.047	30.9	312.91	48.04	40.16	32.08	0.047
J1926+1434	1.324 920	211.41	49.923	−1.039	Z049.9−01.0	0.052	16.0	31.59	6.20	25.00	20.73	0.052
J1928+1923	0.817 330	476.00	54.281	1.016	Z054.4+01.2	0.082	30.9	15.02	2.33	13.64	6.75	0.082
J1928+1923	0.817 330	476.00	54.281	1.016	Z054.4+00.9	0.071	30.9	17.79	2.76	14.56	8.98	0.071
J1929+2121	0.723 599	66.00	56.117	1.751	Z056.3+01.5	0.021	15.0	13.85	2.12	18.07	8.44	0.021
J1931+1536	0.314 355	140.00	51.406	−1.599	Z051.5−01.8	0.037	11.0	15.08	2.34	10.69	Missed	0.037
J1932+1059	0.226 518	3.18	47.382	−3.884	G047.6−03.9	0.020	7.4	1892.28	360.78	866.89	573.26	0.020
J1932+2020	0.268 217	211.15	55.575	0.639	Z055.5+00.7	0.076	18.4	23.11	8.55	35.03	11.77	0.076
J1932+2020	0.268 217	211.15	55.575	0.639	Z055.5+00.8	0.081	18.4	21.06	7.79	19.12	10.55	0.081
J1932+2220	0.144 470	219.20	57.356	1.554	Z057.4+01.6	0.043	5.7	46.82	8.14	51.38	13.73	0.043
J1935+1616	0.358 738	158.52	52.436	−2.093	Z052.6−01.9	0.064	9.0	1586.58	332.19	903.43	106.78	0.064
J1935+2025	0.080 118	182.00	56.051	−0.053	Z055.9−00.3	0.054	3.7	16.35	2.48	10.58	Missed	0.054
J1938+2213	0.166 116	91.00	57.903	0.308	Z057.8+00.5	0.029	6.8	24.01	3.74	8.52	Missed	0.029
J1946+2535	0.515 167	248.81	61.809	0.283	Z061.8+00.1	0.071	8.6	20.18	3.05	7.75	Missed	0.071
J1948+2551	0.196 627	289.27	62.207	0.131	Z062.4+00.3	0.075	9.2	14.60	2.27	8.44	Missed	0.075
J1948+3540	0.717 311	129.07	70.702	5.047	G070.9+05.1	0.082	19.3	254.96	48.03	153.95	8.24	0.082

J1954+2923	0.426 677	7.93	65.924	0.772	Z066.0+00.9	0.075	6.0	348.88	141.16	58.09	37.65	0.075
J1955+5059	0.518 938	31.97	84.793	11.553	G085.0+11.8	0.077	6.0	204.59	59.81	137.27	25.26	0.077
J2002+3217	0.696 761	142.21	69.261	0.879	Z069.5+00.8	0.080	17.5	36.14	6.32	37.62	37.18	0.080
J2002+3217	0.696 761	142.21	69.261	0.879	Z069.5+00.9	0.062	17.5	46.57	8.14	37.77	38.31	0.062
J2002+4050	0.905 067	131.33	76.611	5.288	G076.8+05.1	0.053	24.8	221.85	35.38	87.04	58.11	0.053
J2004+3137	2.111 260	234.82	69.011	0.021	Z068.8+00.1	0.050	21.3	126.81	20.43	58.62	11.33	0.050
J2010+2845	0.565 369	112.47	67.210	−2.472	Z067.1−02.3	0.062	13.6	16.95	2.72	8.15	Missed	0.062
J2018+2839	0.557 953	14.20	68.099	−3.983	G068.0−03.8	0.065	14.9	1192.60	548.49	362.21	8.06	0.065
J2022+5154	0.529 197	22.65	87.862	8.380	G087.9+08.4	0.021	7.4	2327.80	852.77	1095.14	675.99	0.021
J2023+5037	0.372 619	33.02	86.863	7.544	G087.1+07.5	0.035	4.7	173.31	47.33	29.23	4.67	0.035
J2029+3744	1.216 800	190.66	76.898	−0.727	Z076.8−00.9	0.019	22.3	38.78	8.76	30.63	12.87	0.019
J2037+3621	0.618 715	93.56	76.746	−2.840	Z077.0−02.8	0.030	10.7	50.42	26.35	58.51	52.24	0.030
J2055+3630	0.221 508	97.31	79.133	−5.589	G079.4−05.6	0.043	7.2	118.34	18.84	82.55	32.27	0.043
J2108+4441	0.414 871	139.83	86.909	−2.012	Z087.0−02.2	0.040	27.2	159.39	28.17	139.56	61.14	0.040
J2113+4644	1.014 690	141.26	89.003	−1.266	Z088.9−01.4	0.036	32.1	845.36	138.26	272.79	402.85	0.036
J2149+6329	0.380 140	128.00	104.254	7.412	G104.0+07.4	0.018	18.1	126.04	26.38	102.91	36.15	0.018
J2150+5247	0.332 206	148.93	97.521	−0.915	Z097.8−00.9	0.033	11.1	88.55	19.08	55.45	27.51	0.033
J2208+5500	0.933 161	101.03	100.939	−0.751	Z100.8−00.5	0.067	8.6	15.80	5.42	13.13	Missed	0.067
J2208+5500	0.933 161	101.03	100.939	−0.751	Z101.3−00.8	0.072	8.6	14.58	5.00	11.39	Missed	0.072
J2217+5733	1.056 840	162.75	103.472	0.599	Z103.4+00.9	0.058	13.0	15.19	5.21	15.48	14.56	0.058
J2219+4754	0.538 469	43.50	98.385	−7.598	G098.3−07.4	0.052	7.5	192.87	29.30	51.10	14.10	0.052
J2225+6535	0.682 542	36.08	108.637	6.846	G108.5+06.6	0.056	21.1	81.75	20.67	20.51	9.99	0.056
J2240+5832	0.139 935	263.50	106.566	−0.111	Z106.6−00.1	0.070	10.0	55.40	16.87	129.10	123.67	0.070
J2240+5832	0.139 935	263.50	106.566	−0.111	Z106.6−00.3	0.078	10.0	48.48	14.77	24.88	13.80	0.078
J2257+5909	0.368 246	151.08	108.831	−0.575	Z108.9−00.6	0.049	14.8	336.71	62.00	290.59	5.23	0.049
J2308+5547	0.475 068	46.54	108.729	−4.206	G108.8−04.3	0.058	26.9	57.97	12.99	54.51	16.48	0.058
J2321+6024	2.256 490	94.59	112.095	−0.566	Z112.4−00.6	0.029	131.1	407.98	73.33	385.87	305.56	0.029
J2325+6316	1.436 310	197.37	113.418	2.013	Z113.5+02.2	0.049	131.2	47.94	13.89	16.68	8.57	0.049
J2326+6113	0.233 652	122.61	112.946	0.003	Z113.1+00.0	0.076	14.7	86.99	22.58	99.33	64.17	0.076
J2337+6151	0.495 370	58.41	114.284	0.233	Z114.4+00.4	0.036	14.5	64.70	17.09	47.61	32.62	0.036

Table 3.3: The HTRU-North survey non-detections of 37 known pulsars. The presented parameters are the same as those given in Table 3.2 with the exception of "S/N refolded" and "S/N FP". Instead we provide possible reasons for non-detection.

PSR	Period (s)	DM (pc cm^{-3})	l (°)	b (°)	Pointing	Beam	S1400 (mJy)	W50 (ms)	S/N expected	S/Nerr expected	Offset (°)	Why missed?
J0725−1635	0.424 311	98.98	231.473	−0.330	Z231.4−00.6	4	0.200	4.1	25.93	5.00	0.040	below sensitivity
J1758−1931	0.692 552	207.00	9.544	2.353	Z009.8+02.4	6	0.208	21.0	15.07	3.06	0.052	below sensitivity
J1809−1943	5.540 740	178.00	10.727	−0.158	Z011.0−00.2	6	0.351	150.0	27.00	11.50	0.057	isolated X-ray pulsar
J1810−1820	0.153 716	452.20	12.064	0.289	Z012.3+00.5	1	0.365	13.6	14.96	4.91	0.056	below sensitivity
J1811−1835	0.557 464	761.00	11.909	0.049	Z011.6+00.0	3	0.216	16.7	15.69	3.81	0.057	below sensitivity
J1815−1910	1.249 920	547.80	11.810	−0.963	Z012.0−00.9	6	0.151	25.4	13.43	3.24	0.064	below sensitivity
J1818−1556	0.952 709	230.00	15.087	−0.227	Z015.0−00.5	4	0.195	26.0	14.94	2.30	0.076	below sensitivity
J1823−1807	1.636 790	330.00	13.636	−2.164	Z013.5−02.4	4	0.277	34.6	24.20	6.19	0.007	RFI, below sensitivity
J1832−0836	0.002 719	28.18	23.109	0.257	Z023.3+00.1	5	0.696	0.1	28.01	0.57	0.035	X-ray pulsar
J1833−1055	0.633 640	543.00	21.231	−1.140	Z021.4−00.9	1	0.240	24.2	15.42	3.90	0.063	below sensitivity
J1842−0415	0.526 682	188.00	28.086	0.111	Z028.0+00.4	2	0.191	11.0	16.77	3.20	0.052	below sensitivity
J1843−0355	0.132 314	797.60	28.484	0.056	Z028.5+00.1	0	0.544	16.7	19.34	5.81	0.021	below sensitivity
J1844−0310	0.525 049	836.10	29.343	0.036	Z029.1+00.0	3	0.290	20.4	18.37	3.49	0.052	below sensitivity
J1845−0545	1.092 350	315.90	27.150	−1.337	Z027.1−01.3	0	0.277	18.0	29.18	5.79	0.042	long-period pulsar, below sensitivity
J1847−0130	6.707 050	667.00	31.147	0.167	Z030.9+00.1	3	0.222	205.0	16.08	3.16	0.024	RFI, below sensitivity
J1848−0023	0.537 624	30.60	32.267	0.447	Z032.1+00.7	2	0.279	17.7	19.43	10.17	0.065	scintillating,below sensitivity
J1849−0317	0.668 408	42.90	29.834	−1.173	Z030.0−01.4	5	0.416	23.2	28.17	5.95	0.043	scintillating,below sensitivity
J1850−0006	2.191 500	570.00	32.764	0.093	Z032.6+00.3	2	0.531	139.0	26.21	4.20	0.027	below sensitivity
J1852+0031	2.180 190	787.00	33.523	0.017	Z033.8+00.1	6	1.123	235.0	41.49	7.93	0.058	RFI
J1852+0305	1.326 150	320.00	35.804	1.160	Z035.8+01.4	2	0.320	15.6	37.55	10.96	0.076	below sensitivity
J1855+0422	1.678 110	438.00	37.314	1.052	Z037.5+01.1	6	0.197	42.7	15.62	3.94	0.070	below sensitivity
J1856+0404	0.420 252	341.30	37.128	0.745	Z037.4+00.7	6	0.320	6.6	32.19	4.76	0.026	not detected
J1857+0057	0.356 929	82.39	34.417	−0.805	Z034.3−00.6	2	0.422	22.0	21.16	4.09	0.066	below sensitivity
J1859+0601	1.044 310	276.00	39.245	0.903	Z039.1+00.7	4	0.186	24.3	15.48	3.14	0.037	below sensitivity
J1901+0320	0.636 584	393.00	36.999	−0.613	Z037.1−00.9	5	0.554	47.2	25.12	4.95	0.037	below sensitivity
J1901+0413	2.663 080	352.00	37.806	−0.232	Z037.9+00.0	1	0.546	83.5	38.95	9.30	0.060	long-period nulling pulsar
J1901+0510	0.614 757	429.00	38.737	0.025	Z039.0+00.1	6	0.378	56.9	15.20	3.11	0.047	below sensitivity
J1906+0414	1.043 360	349.00	38.478	−1.510	Z038.8−01.5	6	0.156	22.0	13.68	2.09	0.022	below sensitivity
J1906+0746	0.144 073	217.75	41.598	0.147	Z041.4+00.1	3	0.354	0.6	52.89	14.65	0.032	young relativistic binary
J1907+0534	1.138 400	524.00	39.717	−0.988	Z040.0−00.9	6	0.183	8.9	26.10	6.31	0.058	long-period, below sensitivity
J1908+0734	0.212 353	11.10	41.585	−0.270	Z041.9−00.3	6	0.328	2.8	36.32	6.81	0.040	scintillating
J1913+0904	0.163 246	95.30	43.502	−0.684	Z043.6−00.4	1	0.140	2.9	13.28	1.98	0.034	below sensitivity
J1914+0631	0.693 811	58.00	41.352	−2.071	Z041.5−02.2	5	0.138	12.6	13.06	5.40	0.054	below sensitivity
J1916+0748	0.541 752	304.00	42.772	−2.047	Z042.6−02.3	4	1.582	80.0	48.78	10.05	0.048	giant pulses expected
J1920+1040	2.215 800	304.00	45.784	−1.590	Z045.6−01.9	4	0.221	45.0	19.74	3.87	0.078	long-period pulsar, below sensitivity
J1923+1706	0.547 209	142.50	51.707	0.965	Z052.0+00.9	6	0.228	19.0	15.45	2.40	0.050	below sensitivity
J1955+2908	0.006 133	104.50	65.839	0.443	Z066.0+00.7	1	0.701	1.8	13.66	3.71	0.034	below sensitivity

Table 3.4: Parameters obtained for six HTRU-North discoveries made in this work. The subsequent columns list pulsar names, J2000 equatorial coordinates with right ascension (R.A.) and declination (Decl.), their Galactic coordinates with longitude (l) and latitude (b), spin periods (P) with their first derivatives ($\dot{P}$) (if available), dispersion measures (DM) and DM-derived distances according to the `NE2001` and `YMW16` models.

PSR	R.A. (hh:mm:ss.ss)	Decl. (° ′ ″)	l (°)	b (°)	P (ms)	$\dot{P}$ (s/s)	DM (pc cm^{-3})	Distance (NE2001) (kpc)	Distance (YMW2016) (kpc)
J0100+6427	01:00:45.53(2)	+64:27:50.2(7)	123.94	1.61	153.65055	—	229.3	> 44.77	6.31
J1951+4721	19:51:32	+47:21:37	81.25	10.32	181.92548	$1.26230956 \times 10^{-12}$	106.758	6.44	9.65
J2041+4551	20:41:39.67(7)	+45:51:43(1)	84.76	2.32	1159.808064	—	311.5	13.78	9.02
J2045+3633[a]	20:45:01.5050(1)	+36:33:01.4033(8)	77.83	−3.93	31.681843248536(10)	$5.883(3) \times 10^{-19}$	129.5458(2)	5.51	5.63
J2053+4650[a]	20:53:52.62804(7)	+46:50:51.7181(4)	86.86	1.30	12.586275314350(2)	$1.7229(8) \times 10^{-19}$	98.0828(6)	4.12	3.81
J2327+6241[b]	23:27:35.30	+62:41:53.5	113.48	1.37	266.1445	—	196.811	8.82	4.68

[a] See Chapter 4. Numbers in parentheses represent the nominal 1-σ uncertainties in the last digit determined by `TEMPO2`
[b] Co-discovery with the GBNCC survey (Stovall et al., 2014)

Table 3.5: Parameters of the "same-era" detections. The subsequent columns contain the pulsar name, spin period (P), dispersion measure (DM), Galactic coordinates with longitude (l) and latitude (b), the name of the survey where the pulsar was detected, the date of discovery in that survey, the date of discovery in the HTRU-North, the name of the pointing and beam for the HTRU-North detections.

PSR	Period (s)	Dispersion measure (pc cm^{-3})	l (°)	b (°)	Survey	Disc. date[a]	HTRU-NORTH disc. date	Pointing	Beam
J1922+1733	0.236 171	238	52.08	1.23	pksngp,palfa	2013	16/08/2011	Z052.1+01.4	1
J1929+1955	0.257 832	281	54.879	1.018	pksngp,palfa	2013	16/08/2011	Z055.0+01.2	1
J0519+54	0.340 194	43	155.893	9.768	gbncc	2014	12/29/2012	G152.5+07.9	2
J1850+15	1.383 96	24.7	46.688	7.292	pkssw	2010	07/03/2016	G046.9+07.4	1
J2240+5832	0.139 935	263.5	106.566	−0.111	misc	2011	06/26/2014	Z106.6−00.3	5
J0248+6021	0.217 094	370	136.903	0.697	misc	2011	08/24/2015	Z137.1+00.4	5,6
J1928+1923	0.817 33	476	54.281	1.016	pksngp,palfa	2013	04/05/2015	Z054.4+00.9	5
J1929+2121	0.723 599	66	56.117	1.751	pksngp	2013	01/02/2016	Z056.3+01.5	5
J0136+63	0.717 895	286	127.844	1.254	gbncc	2014	09/17/2015	Z127.9+01.2	4

[a] As reported in the `ATNF pulsar catalogue`

Chapter 4

The discovery of two mildly recycled binary pulsars in the Northern High Time Resolution Universe pulsar survey

---

This chapter is a reproduction of:

***Berezina M.**, Champion D. J., Freire P. C. C., Tauris T. M., Kramer M., Lyne A. G., Stappers B. W., Guillemot L., Cognard I., Barr E. D., Eatough R. P., Karuppusamy R., Spitler L. G., Desvignes G., "The discovery of two mildly recycled binary pulsars in the Northern High Time Resolution Universe pulsar survey", Monthly Notices of the Royal Astronomical Society, 2017, Vol. 470, Is. 4, pp. 4421–4433.*

In this work I was principally responsible for the discovery, follow-up observations, timing analysis and writing the paper.

4.1 Abstract

We report the discovery and the results of follow-up timing observations of PSR J2045+3633 and PSR J2053+4650, two binary pulsars found in the Northern High Time Resolution Universe pulsar survey being carried out with the Effelsberg radio telescope. Having spin periods of 31.7 ms and 12.6 ms respectively, and both with massive white dwarf companions, $M_c > 0.8\,M_\odot$, the pulsars can be classified as mildly recycled. PSR J2045+3633 is remarkable due to its orbital period (32.3 days) and eccentricity $e = 0.01721244(5)$ which is among the largest ever measured for this class. After almost two years of timing the large eccentricity has allowed the measurement of the rate of advance of periastron at the 5-σ level, $0.0010(2)^\circ\ \mathrm{yr}^{-1}$. Combining this with a detection of the orthometric amplitude of the Shapiro delay, we obtained the following constraints on the component masses (within general relativity): $M_p = 1.33^{+0.30}_{-0.28}\,M_\odot$, and $M_c = 0.94^{+0.14}_{-0.13}\,M_\odot$. PSR J2053+4650 has a 2.45-day circular orbit inclined to the plane of the sky at an angle $i = 85.0^{+0.8}_{-0.9}$ deg. In this nearly edge-on case the masses can

be obtained from the Shapiro delay alone. Our timing observations resulted in a significant detection of this effect giving: $M_p = 1.40^{+0.21}_{-0.18}\,M_\odot$, and $M_c = 0.86^{+0.07}_{-0.06}\,M_\odot$.

4.2 Introduction

The discovery rate of binary pulsars has been rapidly increasing over the last decade and the population currently includes ∼250 systems (Manchester et al., 2005). There is a large diversity among the nature of the companion stars and the characteristics of both the pulsars and their orbits (e.g. Tauris, 2011). The companion stars detected so far are either non-degenerate main-sequence stars, semi-degenerate (and hydrogen rich) dwarfs, helium white dwarfs (He WDs), carbon-oxygen (CO) or oxygen-neon-magnesium (ONeMg) WDs, or neutron stars (NSs). Some pulsars are found with planets (e.g. PSR B1257+12, Wolszczan & Frail, 1992), and some are members of a triple system (e.g. PSR J0337+1715, Ransom et al., 2014).

The vast majority of the observed binary radio pulsars have been recycled via accretion of mass and angular momentum from a companion star (Bhattacharya & van den Heuvel, 1991; Tauris & van den Heuvel, 2006), often leading to formation of a millisecond pulsar (MSP). Accreting pulsars are observable in X-rays (Bildsten et al., 1997) as low- (LMXB), intermediate- (IMXB) or high-mass X-ray binaries (HMXB), depending on the mass of the donor star. The initial mass of the donor star has an impact on the duration and stability of the mass-transfer phase and, hence, the efficiency of the recycling process. This, in turn, determines the main properties of the recycled pulsar, in particular its spin period and spin-down rate, as well as the final orbital configuration. This can clearly be seen when examining these properties as a function of the compact companion type in the known MSP population (Tauris et al., 2012). (In the following, we discard binary pulsars observed in dense environments like globular clusters since these binaries are possibly formed via exchange encounters (e.g. Verbunt & Freire, 2014) and therefore have a different formation history compared to binary pulsars in the Galactic disk.) For example, MSPs with low-mass He WD companions are often fully recycled (with spin periods, $P < 10$ ms, and period derivatives, $\dot{P} \lesssim 10^{-20}$), whereas MSPs with massive CO/ONeMg WDs are often only mildly recycled with $10 < P < 100$ ms and $10^{-20} < \dot{P} < 10^{-18}$. The most massive donor stars are found in HMXBs. If such systems remain bound after the second supernova (SN) explosion, they produce double NS systems. In wide-orbit HMXBs, the effective mass-transfer phase is so short that the first born NS only becomes a marginally recycled pulsar (Tauris et al., 2015), in some cases with a spin period exceeding 100 ms. A prime example of such a system is the double NS system PSR J1930−1852 (Swiggum et al., 2015) which hosts a mildly recycled pulsar with $P = 185$ ms and has an orbital period of 45 days.

Pulsars with a compact star companion represent the end-point of binary stellar evolution. Thus, we can use the observed characteristics of these systems as fossil records to learn about stellar evolution and binary interactions in their progenitor systems (Lazarus et al., 2014). MSPs with He WD companions, and which have been

recycled via stable Roche-lobe overflow (RLO) in LMXBs, possess a unique correlation between the mass of the WD and the orbital period (e.g. Tauris & Savonije, 1999; Istrate et al., 2014). Furthermore, for these systems the orbital eccentricities are also correlated with the orbital period (Phinney, 1992; Phinney & Kulkarni, 1994), such that binaries with short orbital periods are more circular in general. For double NS systems, it is even possible to put constraints on the properties of the second SN explosion (Wex et al., 2000; Ferdman et al., 2013, 2014; Tauris et al., 2015).

Recycled pulsars with CO/ONeMg WD companions (also known as intermediate-mass binary pulsars, IMBPs) were first recognized as a separate class by Camilo (1996). Initially, it was thought that all such binaries form via common-envelope (CE) evolution. This idea was based on the formation scenario for PSR J2145−0750 (Bailes et al., 1994) which was put forward by van den Heuvel (1994). However, it was later demonstrated (Tauris et al., 2000) that such intermediate-mass binary pulsar systems can also be formed without the need for CE evolution, in cases when the observed orbital period is larger than 3 days. For these wider systems, the formation process was most likely dynamically stable RLO in an IMXB.

Although some consensus in our understanding of binary pulsars is emerging, it is important to keep finding new systems that will challenge current ideas and bring forward new lines of research. The discovery of PSR J1614−2230 (Demorest et al., 2010), which is the first example of a fully recycled MSP with a CO WD companion – and the first NS with a precisely measured mass close to 2.0 $M_{\odot}$ – came somewhat as a surprise. Subsequently, detailed modelling by Lin et al. (2011) and Tauris et al. (2011), suggested that this system is the first known example of an IMXB system which produced a radio pulsar evolving via Case A RLO (i.e. mass transfer initiated while the donor star is still burning hydrogen in its core). Hence, a third possibility for producing a recycled pulsar with a CO/ONeMg WD is now accepted.

The number of pulsar binaries with CO/ONeMg WDs now exceeds 30 systems. Their orbital eccentricities can vary from the order of 10^{-6} to 10^{-2}. This large spread in eccentricity suggests different formation paths. With only a small number of such systems known with precisely measured masses of the stellar components (apart from: PSR J1614−2230 (Ransom et al., 2014), PSR J1802−2124 (Ferdman et al., 2010) and PSR J0621+1002 (Splaver et al., 2002)), it is difficult to speculate more precisely about their previous evolution. The discovery of new NSs with massive WD companions, which allow for mass determinations, would help shed new light on the formation process. Furthermore, precise knowledge of the present pulsar mass – in combination with other system parameters available from pulsar timing and theoretically computed binary models – will make it possible to estimate the amount of accreted material (and hence to infer the birth mass of the NS), determine which binary interactions were at work, and, consequently, try to deduce the formation history of the system as a whole. As an additional bonus, precise mass measurements can also serve for constraining the equation-of-state of cold dense matter within NSs (Özel & Freire, 2016).

Here, we present the discovery and follow-up timing of two new mildly recycled MSPs which appear to be promising for the aforementioned purposes. They were discovered in June 2014 in the Northern High Time Resolution Universe survey (Barr

et al., 2013). The structure of the paper is as follows: In Section 2, we introduce the survey and the discoveries; in Section 3, we describe our timing campaigns; in Section 4, we present the results of timing and polarisation analysis, discuss the details of the performed mass measurements and speculate about the eccentricity-binary period relation for IMBPs, and, finally, in Section 5, we summarize our work.

4.3 MSP discoveries in the HTRU-North Survey

4.3.1 HTRU-North

The Northern High Time Resolution Universe survey for pulsars and fast transients is being conducted with the 100-m Effelsberg radio telescope in Germany. It makes use of the 21-cm seven-pixel multibeam receiver and the polyphase filterbank backend providing a time resolution of 54 μs and a 300-MHz passband centred around 1.36 GHz and split into 512 channels.

Being a counterpart of the Southern survey (HTRU-South; Keith et al., 2010), it follows the same observing convention with the sky split into three regions (the only difference is the integration time): low Galactic latitudes – $|b| < 3.5^\circ$ where each sky pointing is observed for 25 minutes, medium Galactic latitudes – $|b| < 15^\circ$ with the integration time of 3 minutes and high Galactic latitudes – $|b| > 15^\circ$ with 1.5 minute integrations. Pointings located in and near the Galactic plane are expected to harbour the highest yield of interesting PSR-WD or DNS systems (or even exotic systems with black hole companions; e.g. Belczynski et al., 2002) that can be used for such scientific purposes as studying stellar evolution, testing general relativity, constraining the equation-of-state of supra-nuclear matter (e.g. Lorimer, 2008). For this reason, we are currently concentrating on the mid-latitude region with 3-minute integration times as a shallow survey of the plane can speed up the discovery and further studies of the brightest pulsars.

The northern part of the plane (as well as the whole northern sky) visible from Effelsberg has not yet been investigated in the L-Band, except for some regions of overlap with other 21-cm surveys like PALFA (e.g. Cordes et al., 2006; Lazarus, 2013), whose declination range is limited leaving large areas of the Galaxy uncovered, or with the southern surveys (HTRU-South, PMPS - see, for example, (Lorimer et al., 2006)). A high observing frequency reduces the impact of interstellar medium effects (such as dispersion and scattering) allowing the Galactic plane to be probed more deeply for distant objects. This depth of scanning distinguishes the HTRU-North from and, at the same time, makes it complementary to the low-frequency Northern-sky surveys such as the 350-MHz GBNCC (Stovall et al., 2014), GBT drift-scan (Karako-Argaman et al., 2015) or the 140-MHz LOFAR pulsar surveys (Coenen et al., 2014) and the all-sky Arecibo 327 MHz drift survey (Deneva et al., 2013a) which use the steep spectral index observed in most pulsars to detect nearby weak sources. The full description of the survey and previous discoveries can be found in Barr et al. (2013, 2017).

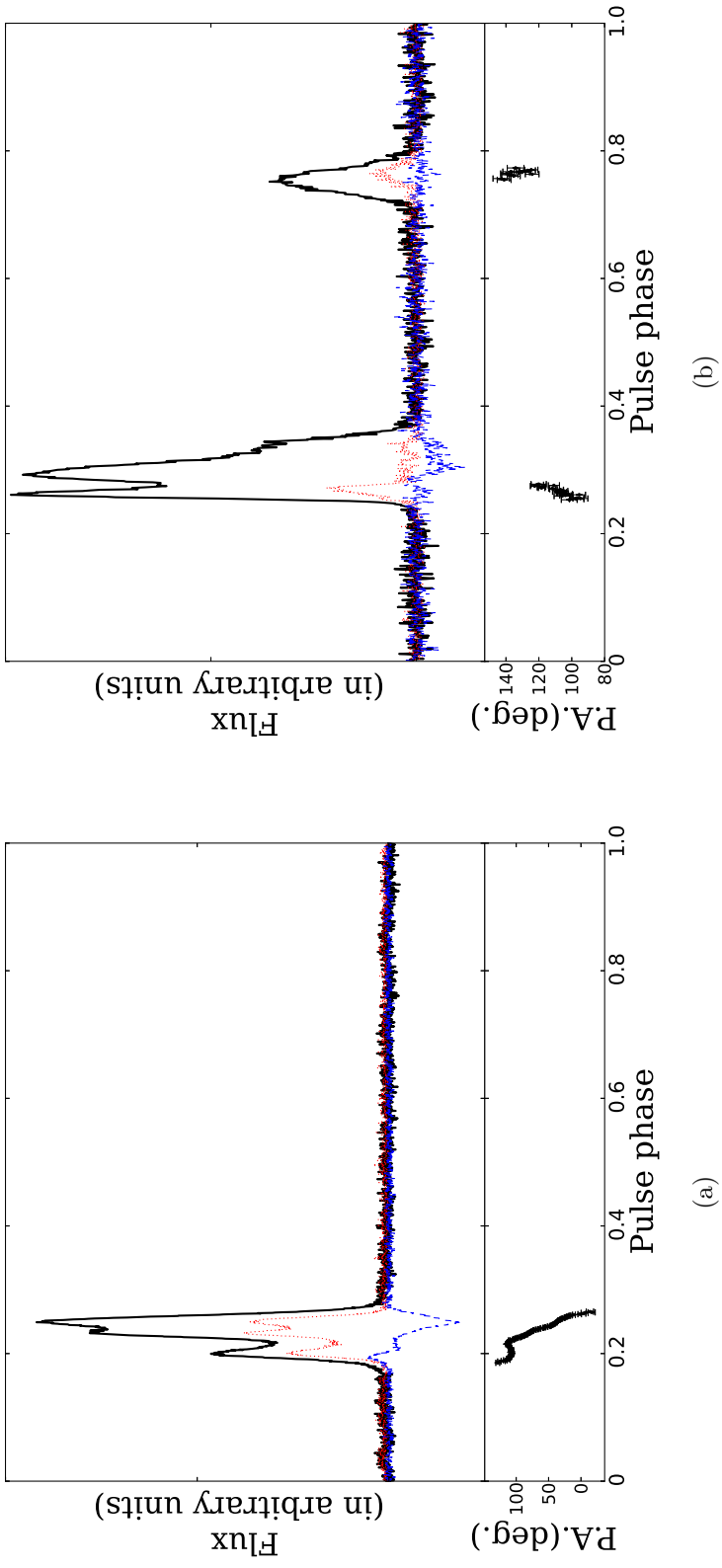

Figure 4.1: *Top* - Average pulse profiles with total intensity (black solid), linear (red dotted) and circular (blue dashed) polarisation vs. pulse phase for (a) PSR J2045+3633 obtained with the Arecibo telescope at 1430.8 MHz and (b) PSR J2053+4650 obtained with the Effelsberg telescope at 1347.5 MHz. *Bottom* - Position angle of linear polarisation vs. pulse phase.

4.3.2 Discoveries, initial timing and first scientific goals

Each of the two new bright binary MSPs, PSR J2045+3633 and PSR J2053+4650 (see Fig. 4.1a, 4.1b), with spin periods 31.68 ms and 12.58 ms, respectively, was found in 3-minute integration filterbank data down-sampled by factors of four in time and two in frequency, as is usual for survey processing with the quick-look pipeline. This pipeline (see Barr et al., 2013) is intended to discover the brightest sources as soon as possible, almost in real time. For this reason it operates on the low-resolution version of the data. This pipeline is based on the Fourier transform routines that are typical in pulsar searching. Before searching for periodic candidates, it performs dedispersion with 406 dispersion measure (DM) trials in the range of 0–2975 pc cm^{-3} in order to correct for *a priori* unknown dispersive smearing caused by the propagation of the possible pulsar signal through the ionised interstellar medium. This procedure is sufficient to find most solitary pulsars. In case of pulsars in binary systems whose signals can be modulated by orbital acceleration, to recover the original signal, an additional step of trying many possible acceleration values may be necessary. This is especially crucial for highly relativistic systems in short orbits. As this task is time-consuming and computationally intensive, the quick-look pipeline does not perform it, thus, limiting our detectability of highly accelerated systems but it still remains sensitive to non-relativistic pulsar binaries with relatively high DMs, like PSR J2045+3633 and PSR J2053+4650 (129.5 pc cm^{-3} and 98.08 pc cm^{-3}, respectively).

Confirmation observations for both pulsars were performed with the Effelsberg telescope soon after the discovery. Data taken in search and baseband modes for five minutes on several occasions within two weeks after the confirmation showed Doppler-shift variations of the spin period caused by the orbital motion. The fitorbit[1] program was used to produce robust initial parameter estimations prior to commencement of pulsar timing observations. Having the ephemeris allowed us to carry out observations in coherent-dedispersion real-time folding mode provided by the PSRIX (Lazarus et al., 2016) backend. From these data the times-of-arrivals (TOAs) were produced with `psrchive`[2] tools for pulsar analysis by doing standard procedures of cross-correlating the corresponding profile (obtained by fully integrating the archive file in time and frequency) with a template generated with `paas`. The initial timing model was fit to the data with `TEMPO` [3] software resulting in a phase-coherent timing solution.

These first results showed that both pulsars are in binary orbits (with periods of 32.3 days for PSR J2045+3633 and 2.45 days for PSR J2053+4650) with massive companions. Moreover, both systems looked promising for precise measurements of the masses of the components through determination of post-Keplerian parameters (Taylor & Weisberg, 1982). PSR J2045+3633 has revealed an eccentricity $e = 0.0172$, making possible a measurement of the rate of periastron advance. PSR J2053+4650 seemed to be in a circular, but highly-inclined orbit allowing the possible detection of the Shapiro delay (Shapiro, 1964) caused by the propagation of the pulsar signal in the

[1] https://github.com/gdesvignes/fitorbit/
[2] http://psrchive.sourceforge.net/
[3] http://sourceforge.net/

gravitational field of the companion (the effect is most noticeable when the orbit is close to being visible edge-on, i.e. the orbital inclination angle $i \approx 90^\circ$). The low root-mean-square (rms) of the first timing residuals (30 to 40 μs for each pulsar) indicated that significant measurements of these parameters could be made on a short-term basis (within a few years).

4.4 High precision timing and analysis

Regular timing was started in September 2014. The general timing strategy (i.e., excluding special campaigns – see 4.4.1 and 4.4.2) for both pulsars was similar: they were systematically followed up with the Lovell, Effelsberg and – (since March 2015) – Nançay radio telescopes, with an observation lasting, on average, 30–60 minutes. At Jodrell Bank, the pulsars were observed almost daily during the first three weeks and later – once in 10–20 days, at Effelsberg – almost monthly since December 2014 until November 2015, at Nançay the cadence varied from every day to once in a few months. Observational parameters and the details of the recording systems are presented in Table 4.1.

The overall preparation procedure was the same for the data from all the observatories: using `psrchive` tools, the data from each telescope were cleaned of RFI, fully integrated in time and integrated in frequency to keep a number of subbands from one to four (depending on the observatory – see Table 4.1) and cross-correlated with a telescope-specific template to create TOAs. For the Lovell and Effelsberg observations we used an analytic template fit to the high signal-to-noise data created with the `paas` routine from `psrchive`. For Nançay the template was produced by adding 10 high signal-to-noise profiles for each pulsar, and the results from these additions were then smoothed. For the highest-quality Arecibo data the template was constructed from the average Arecibo pulse profiles over observed epochs. In our timing analysis we used `TEMPO2` software package (Hobbs et al., 2006) refining the timing model by least-square fitting the parameters of the system. The TOAs from different observatories were converted to the Solar System barycentre using the DE421 ephemeris. The details of fitting and models used are described in Section 4.5.3.

Given the eccentricity of PSR J2045+3633 and the fortuitous orbital inclination of PSR J2053+4650, we initiated special timing campaigns aiming to improve the measurement of the rate of advance of periastron and, possibly, the Shapiro delay for PSR J2045+3633, and the Shapiro delay for PSR J2053+4650, with a goal of constraining the masses of the pulsar and companion in both systems.

Table 4.1: Timing observations of PSRs J2045+3633 and J2053+4650 with four telescopes

Telescope	Effelsberg	Jodrell Bank	Nançay	Arecibo
Backend	PSRIX	ROACH	NUPPI	PUPPI
Centre frequency (MHz)	1347	1520	1484	1430
Effective bandwidth (MHz)	240	384	512	600
Integration time (min)	30	30	10	11
Observation Parameters for PSR J2045+3633				
Number of TOAs	274	75	214	30
Number of frequency subbands (for producing TOAs)	4	1	4*	1
Weighted RMS of post-fit Timing Residuals (μs)	5.388	4.356	7.541	1.110
EFAC	1.297	1.033	1.245	2.757
Date span (MJD)	56996–57284	56911–57538	57097–57506	57258–57294
Observation Parameters for PSR J2053+4650				
Number of TOAs	121	79	600	—
Number of frequency subbands (for producing TOAs)	2	1	4*	—
Weighted RMS of post-fit Timing Residuals (μs)	3.078	3.128	5.189	—
EFAC	1.318	1.208	1.145	—
Date span (MJD)	56996–57145	56911–57538	57097–57490	—

* In most cases we kept four subbands but for some epochs the TOAs with uncertainties larger than 8 μs were excluded from the analysis resulting in two or three TOAs per epoch.

4.4.1 Special campaigns: PSR J2045+3633

For PSR J2045+3633 we conducted two full-orbit campaigns: one with the Effelsberg telescope and, in order to maximise our sensitivity, one with Arecibo.

The 32-day Effelsberg campaign took place in April–May 2015 and consisted of 10 four-hour observations at a central frequency of 1.4 GHz spread across the orbit. The data were recorded with the PSRIX (Lazarus et al., 2016) backend in its coherent-dedispersion real-time folding mode (the same system that is used for regular timing). The average TOA error was 3 μs.

The Arecibo campaign was held in August–September 2015 with the use of the L-band wide receiver. The data were coherently folded in real time with the PUPPI (Puerto Rico Ultimate Pulsar Processing Instrument) backend (Table 4.1). We performed 6 full-transit (55-minute) observations covering a part of the orbit. Due to some issues with the receiver, it was not possible to cover the whole orbit as planned but the data obtained (combined with all the other TOAs) still allowed us to measure the rate of advance of periastron ($\dot{\omega}$) at 5-σ level: $0.0010(2)^\circ\mathrm{yr}^{-1}$ – and an indication of the Shapiro delay with 3- and 2-σ measurement of its orthometric amplitude and ratio: $h_3 = 1.0(3)$ μs and $\varsigma = 0.6(3)$ respectively (see Section 4.5.3).

The average TOA error from this campaign was 0.29 μs for the 11-minute observations fully scrunched in time and frequency. The higher precision of these TOAs compared to the ones from other telescopes made them overweighted in the overall timing analysis. For this reason, TOA uncertainties for a set of data from every observatory were multiplied by a factor (EFAC) between 1.033 and 2.757 (see Table 4.1) to achieve reduced $\chi^2 = 1$. EFACs of Jodrell Bank, Effelsberg and Nançay TOAs, slightly differing from unity, can be explained by the presence of RFI in the data whereas a much larger EFAC of much more precise Arecibo TOAs is probably an evidence of the intrinsic pulsar red noise. The overall timing residuals as a function of MJD and orbital phase are presented in Fig. 4.2.

4.4.2 Special campaign: PSR J2053+4650

For PSR J2053+4650 we performed two successive full-orbit campaigns with the Effelsberg telescope in the course of five days (April 29th–May 3rd 2015). On the first four days we observed it for four hours every day, and on the fifth day we took a twelve-hour session near the superior conjunction. This campaign helped to make a very significant Shapiro delay detection. Combined with the other TOAs (see Fig. 4.3), this resulted in the 22- and 66-σ measurement of the orthometric amplitude and orthometric ratio respectively: $h_3 = 3.23(15)$ μs and $\varsigma = 0.918(14)$ (see Section 4.5.3).

4.5 Results and discussion

The resulting best-fit timing parameters for both pulsars are presented in Table 4.2. These include spin, astrometric and orbital parameters, as well as the derived masses of the components of the systems.

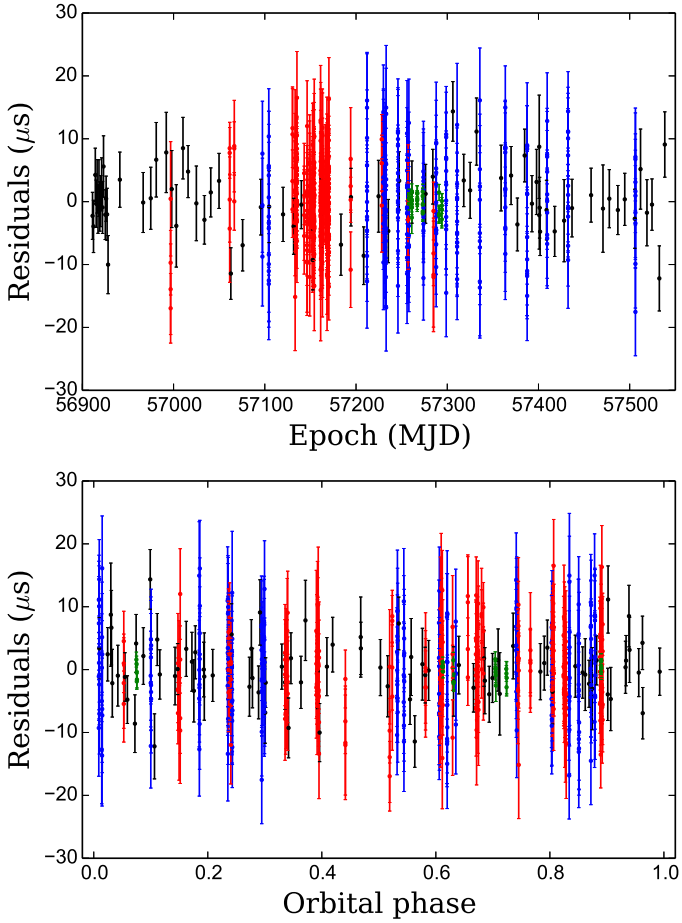

Figure 4.2: The top plot shows the post-fit timing residuals for PSR J2045+3633 as a function of MJD, the bottom plot – as a function of orbital phase. The residuals obtained from the data taken with different telescopes are marked with different colours: Jodrell Bank – black, Nançay – blue, Effelsberg – red, Arecibo – green. The error bars represent the 1-σ uncertainties of TOA measurements.

Table 4.2: Timing parameters for PSRs J2045+3633 and J2053+4650

Pulsar name	PSR J2045+3633	PSR J2053+4650	
Binary model	DDH	DDH	DD
Solar System ephemeris	DE421	DE421	DE421
Spin and astrometric parameters			
Right ascension, α (J2000)	20:45:01.50504(12)	20:53:52.62804(7)	
Declination, δ (J2000)	+36:33:01.4033(8)	+46:50:51.7181(4)	
Proper motion in RA, μ_α (mas yr^{-1})	−2.1(1.4)	−2.8(8)	
Proper motion in DEC, μ_δ (mas yr^{-1})	−2.3(8)	−5.4(5)	
Total proper motion, $\mu_{\rm tot}$ (mas yr^{-1})	3.1(1.1)	6.1(5)	
Galactic longitude, l	77.83	86.86	
Galactic latitude, b	−3.93	1.30	
Pulse frequency, ν (s^{-1})	31.56382007686(1)	79.45162290069(1)	
First derivative of pulse frequency, $\dot{\nu}$ (s^{-2})	$-5.861(4)\times10^{-16}$	$1.0875(6)\times10^{-15}$	
Spin period P (ms)	31.68184324854(1)	12.586275314350(2)	
Observed period derivative, $\dot{P}$ (10^{-19} s s^{-1})	5.883(3)	1.7229(8)	
Dispersion measure, DM (pc cm^{-3})	129.5477(17)	98.0828(6)	
Rotation measure, (rad m^{-2})	−266(10)	−174(11)	
Binary Parameters			
Orbital period, P_b (days)	32.297845(1)	2.4524990114(2)	
Projected semi-major axis of the pulsar orbit, x (lt-s)	46.941885(11)	8.8042995(11)	8.8042996(11)
Epoch of periastron, T_0 (MJD)	57496.75108(3)	56911.113(3)	
Orbital eccentricity, e	0.01721244(5)	0.0000089(1)	
Longitude of periastron, ω (°)	320.7822(3)	266.7(4)	
Relativistic parameters and masses			
Rate of advance of periastron, $\dot{\omega}$ (°yr^{-1})	0.00105(14)	—	—
Orthometric amplitude, h_3 (μs)	1.0(3)	3.23(15)	—
Orthometric ratio, ς	0.6(3)	0.918(14)	—
Orbital inclination, i (°)	62^{+5}_{-6}	$85.0^{+0.8}_{-0.9}$	$85.1^{+0.9}_{-0.7}$
Mass function, f (M$\odot$)	0.1064621(2)	0.12182741(4)	
Total mass, M (M$\odot$)	2.28(45) (derived from $\dot{\omega}$)	—	2.23(24)[a]
Pulsar mass, m_p (M$\odot$)	$1.33^{+0.30}_{-0.28}$[b]	$1.40^{+0.21}_{-0.18}$[b]	1.38(18)[a]
Companion mass , m_c (M$\odot$)	$0.94^{+0.14}_{-0.13}$[b]	$0.86^{+0.07}_{-0.06}$[b]	0.85(6)[a]
Derived parameters			
DM-derived distance (NE2001)[c], d (kpc)	5.51	4.12	
DM-derived distance (YMW16)[d], d (kpc)	5.63	3.81	
Shklovskii's correction to period derivative, $\dot{P}$ (10^{-21} s s^{-1})	4.2(3.1)	6.4(2.2)	6.4(2.2)
Shklovskii-corrected period derivative, $\dot{P}$ (10^{-19} s s^{-1})	5.84(3)	1.66(2)	1.66(2)
Surface magnetic field strength, B_0 (10^9 Gauss)	4.1	1.4	1.4
Characteristic age, τ_c (Gyr)	0.85	1.15	

[a] The pulsar and companion masses are calculated assuming GR from the range and shape of the Shapiro delay. The total mass is then calculated by summing these values.
[b] The pulsar and companion masses derived from the Bayesian mapping (see sections about mass measurements).
[c] We assume the uncertainty on the distance to be 25–30 %, what is commonly accepted when using the `NE2001` model (Cordes & Lazio, 2002), though these numbers represent a very average estimate and in general depend on the line of sight.
[d] We assume the uncertainty on the distance to be 20–40 %, though it may be significantly underestimated (Yao et al., 2017).
Figures in parentheses are the nominal 1-σ TEMPO2 uncertainties in the least-significant digits quoted.

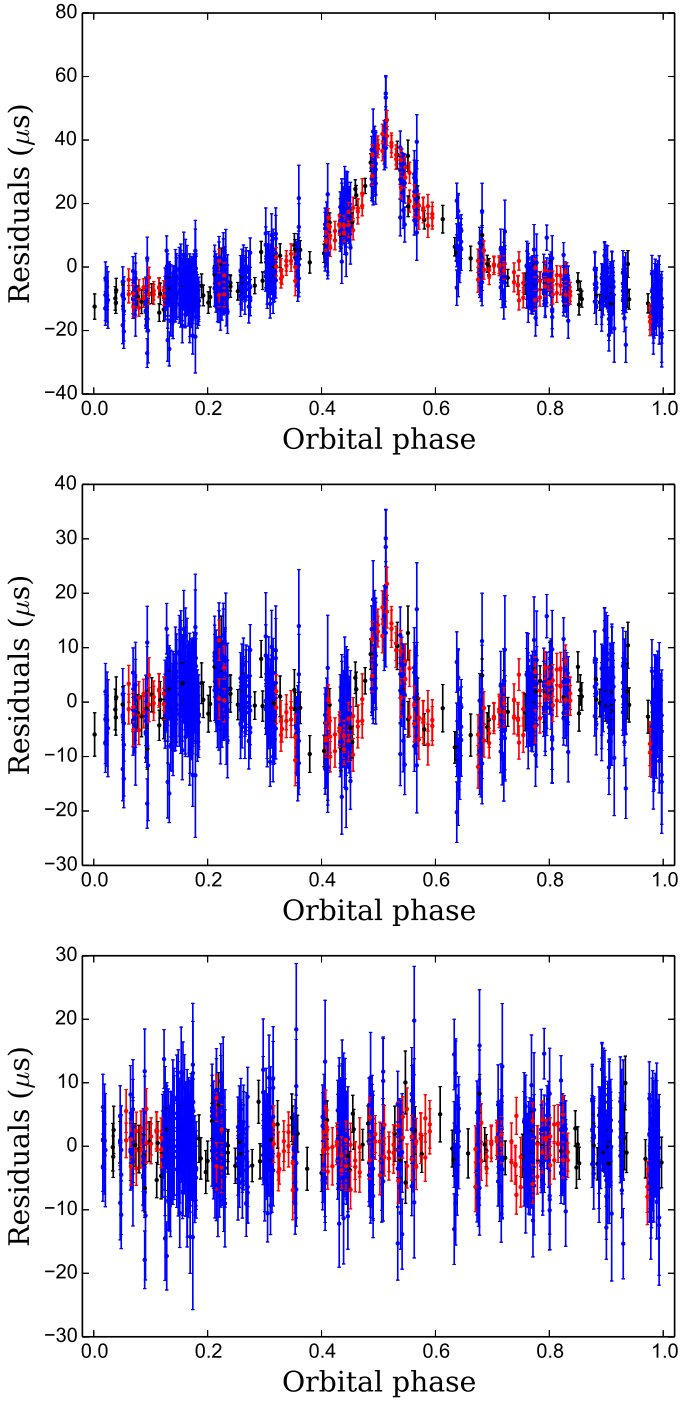

Figure 4.3: Timing residuals for PSR J2053+4650 as a function of orbital phase: the top plot shows residuals before fitting for Shapiro delay parameters, the bottom plot – after fitting. The middle plot shows timing residuals after fitting for Keplerian parameters: a part of the Shapiro delay is absorbed by this fit. The residuals obtained from the data taken with different telescopes are marked with different colours: Jodrell Bank – black, Nançay – blue, Effelsberg – red. The error bars represent the 1-σ uncertainties of TOA measurements.

4.5.1 Polarisation studies

At Effelsberg and Arecibo we performed a polarisation calibration observation with the noise diode prior to every pulsar observation. The diode signal was injected into the receiver feed horn at an angle of 45° to both polarisation probes when the telescope was 0.5° off source. These observations were used to calibrate the pulsar data with `pac` from `psrchive`. Several calibrated observations were then integrated to obtain a low-noise polarisation profile (Fig. 4.1a, 4.1b: for PSR J2045+3633 we present the Arecibo profile as it has much higher signal-to-noise ratio than the one from Effelsberg). The data for both pulsars were corrected for Faraday rotation with the values of rotation measure determined using `rmfit` from `psrchive` (see Table 4.2).

PSR J2045+3633 shows a significant degree of both linear and circular polarisation (Fig. 4.1a). Interpreted in the framework of polarisation features found in non-recycled pulsars (e.g. Lorimer & Kramer, 2012), the change from a weak positive circular polarisation to significant negative polarisation suggests a central line of sight through the beam. This is consistent with the observed steep position angle (PA) swing. Despite the flat PA values in the leading part of the PA swing, it can be well described by a standard rotating vector model (RVM) fit, which in principle allows us to constrain the viewing geometry (e.g. Lorimer & Kramer, 2012). The resulting χ^2 values from a least-squares fit of the RVM to the PA swing produce the contours in the magnetic inclination angle (α) and viewing angle (i.e. angle between the spin axis and the observer's direction, ζ) plane shown in Fig. 4.4.

The correlation between α and ζ is not surprising and is well known; note that $\zeta = \alpha + \beta$, where β is the impact angle, i.e. the angle between magnetic axis and observer at the closest approach. In order to constrain the geometry further, we can utilize the constraints on the orbital inclination angle from pulsar timing, since for a pulsar beam of angular radius ρ to be visible to the observer, we find $|i - \zeta| <\sim \rho$. The constraints on i and $180° - i$ are correspondingly plotted in the upper panel of Fig. 4.4 as horizontal strips with a width identical to their uncertainties. For a pulsar with a filled emission beam, the observed pulse width w is a function of α, ζ and ρ (e.g. Lorimer & Kramer, 2012). For non-recycled pulsars, we find $\rho = k/\sqrt{P}$, where P is the pulse period and value of k depending weakly on frequency. The exact value differs between different authors, but for a width measured at a 10% intensity level k is typically about 6.3° (Kramer et al., 1994). Adopting this relationship and measuring a width of $w = 36°$ we performed Monte Carlo simulations, where we drew ρ from a normal distribution centred on $k = 6.3°$ with a width of 0.63° as a typical uncertainty reflecting both the uncertainty in k and the measured width. We also drew α from a flat distribution between 0 and 180°, while using another flat distribution for $|\beta| \leq \rho$ (i.e. the condition for the observer to register the beam). Testing 10 million combinations, we recorded those values of α where the observed width was consistent with the simulated values. This distribution of α is shown in the bottom panel of Fig. 4.4. Two preferred ranges of solutions near 50° and 130° are clearly visible. Dashed vertical lines indicate a ±34% range around the median value. Interestingly, the solutions for smaller α are more consistent with the joint constraints from the

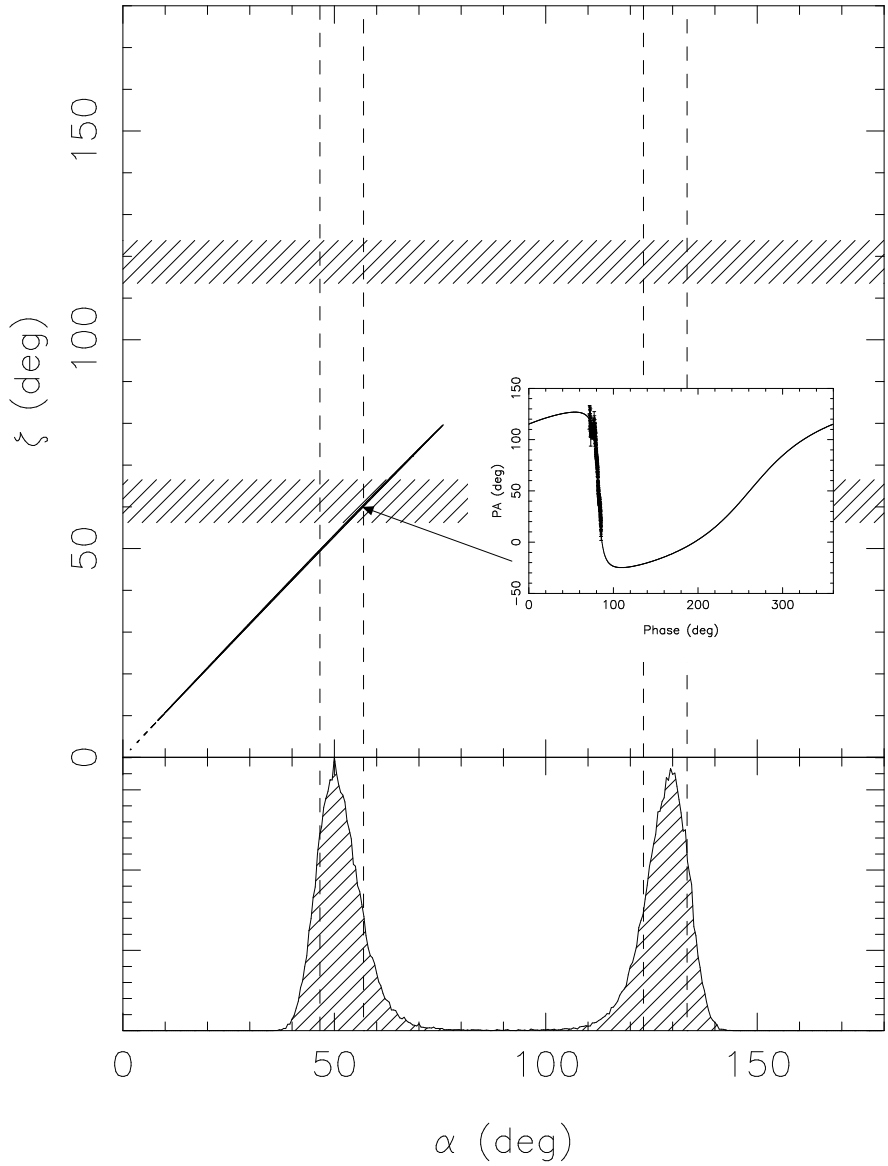

Figure 4.4: System geometry for PSR J2045+3633 as derived from a least-squares-fit of the Rotating Vector Model (RVM) to the position angle (PA) of the linearly polarised emission. The top panel shows the χ^2 contours from minimizing χ^2 by stepping through values of the magnetic inclination angle (α) and viewing angle ζ while simultaneously minimizing reference phase Φ_0 and reference position angle Ψ_0 of the RVM at each grid point. In order to constrain the geometry further in the presence of the correlation between α and ζ, we mark the constraints on the orbital inclination angle as horizontal strips (see text for details). Also, assuming a filled emission beam, we derive a distribution of magnetic inclination angles (lower panel) that is consistent with the observed pulse width (see text for details). The vertical dashed lines indicate a $\pm 34\%$ range around the median value of the two preferred solutions. The solutions for smaller α are more consistent with the joint constraints from the RVM fit and radio timing, indicating that the true underlying orbital inclination angle is $i \sim 60^\circ$ (rather than $180^\circ - 60^\circ = 120^\circ$). A corresponding RVM fit for $\alpha = 57^\circ$ and $\zeta = 60^\circ$ is shown in the small insert in the middle of the figure.

RVM fit and radio timing, indicating that the true underlying orbital inclination angle is $i \sim 60°$ (rather than $180° - 60° = 120°$). A corresponding RVM fit for $\alpha = 57°$ and $\zeta = 60°$ is shown in the small insert in the middle of the figure. In summary, radio timing, PA swing, and profile width data can all be explained in a self-consistent geometric model, making assumptions that were derived from normal (non-recycled) pulsars.

We repeat the same procedure of fitting the RVM model for PSR J2053+4650. We can identify two main groups of significant PA values, clustering around longitudes of 100° and 280°, respectively (see insert in Fig. 4.5). We applied the same method as described above, but allow for the possibility that the two main clusters of PA values are separated by phase offsets of ±90° and ±180°. This leads to various "islands" in the shown χ^2 plot. The indicated best fit solution that is consistent with a measurement of the orbital inclination angle (Table 4.2) is derived for zero offset between the two PA clusters. If we ignore the big "island" outside the alpha range, then the smaller inclination angle (87.5°) is slightly preferred but it is much less clear than in the case of PSR J2045+3633. What is clear from the given constraints is that the best solution is that of an orthogonal rotator, which is also consistent with the observation of an interpulse. Given this nearly orthogonal viewing geometry of the pulsar, it is to be expected that both solutions for the inclination should indeed have nearly equal probability.

4.5.2 Astrometric parameters

High-precision timing observations conducted for both binaries for almost 21 months gave us an opportunity to measure their proper motions. As can be seen from Table 4.2, for PSR J2045+3633 the proper motion is poorly constrained at $\mu_{\rm tot} = 3.1 \pm 1.1\,{\rm mas\,yr^{-1}}$. For PSR J2053+4650 the significance is higher at $\mu_{\rm tot} = 6.1 \pm 0.5\,{\rm mas\,yr^{-1}}$. Knowing the total proper motion, we can derive the transverse velocity from:

$$\frac{v_{\rm t}}{\rm km\,s^{-1}} = 4.74 \times \left(\frac{\mu_{\rm tot}}{\rm mas\,yr^{-1}}\right) \times \left(\frac{\rm d}{\rm kpc}\right), \tag{4.1}$$

where d is the distance to the pulsar. According to the `NE2001` model described in Cordes & Lazio (2002), assuming the 25-30 % uncertainty on the DM-derived distance (although it should be noted that these uncertainties may be underestimated, see Deller et al., 2009), we obtain $v_{\rm t} = 80 \pm 40\,{\rm km\,s^{-1}}$ for PSR J2045+3633 and $v_{\rm t} = 120 \pm 40\,{\rm km\,s^{-1}}$ for PSR J2053+4650. Using the newer YMW20016 model (Yao et al., 2017) and assuming an average distance error of 40 % (though for individual sources it may be significantly larger), we get $v_{\rm t} = 82 \pm 40\,{\rm km\,s^{-1}}$ for PSR J2045+3633 and $v_{\rm t} = 110 \pm 50\,{\rm km\,s^{-1}}$ for PSR J2053+4650. The values obtained within the both models are consistent with each other and with the transverse velocities observed for the general population of binary MSPs (Hobbs et al., 2005; Gonzalez et al., 2011; Desvignes et al., 2016).

As demonstrated by Shklovskii (1970), the apparent period derivative of a pulsar

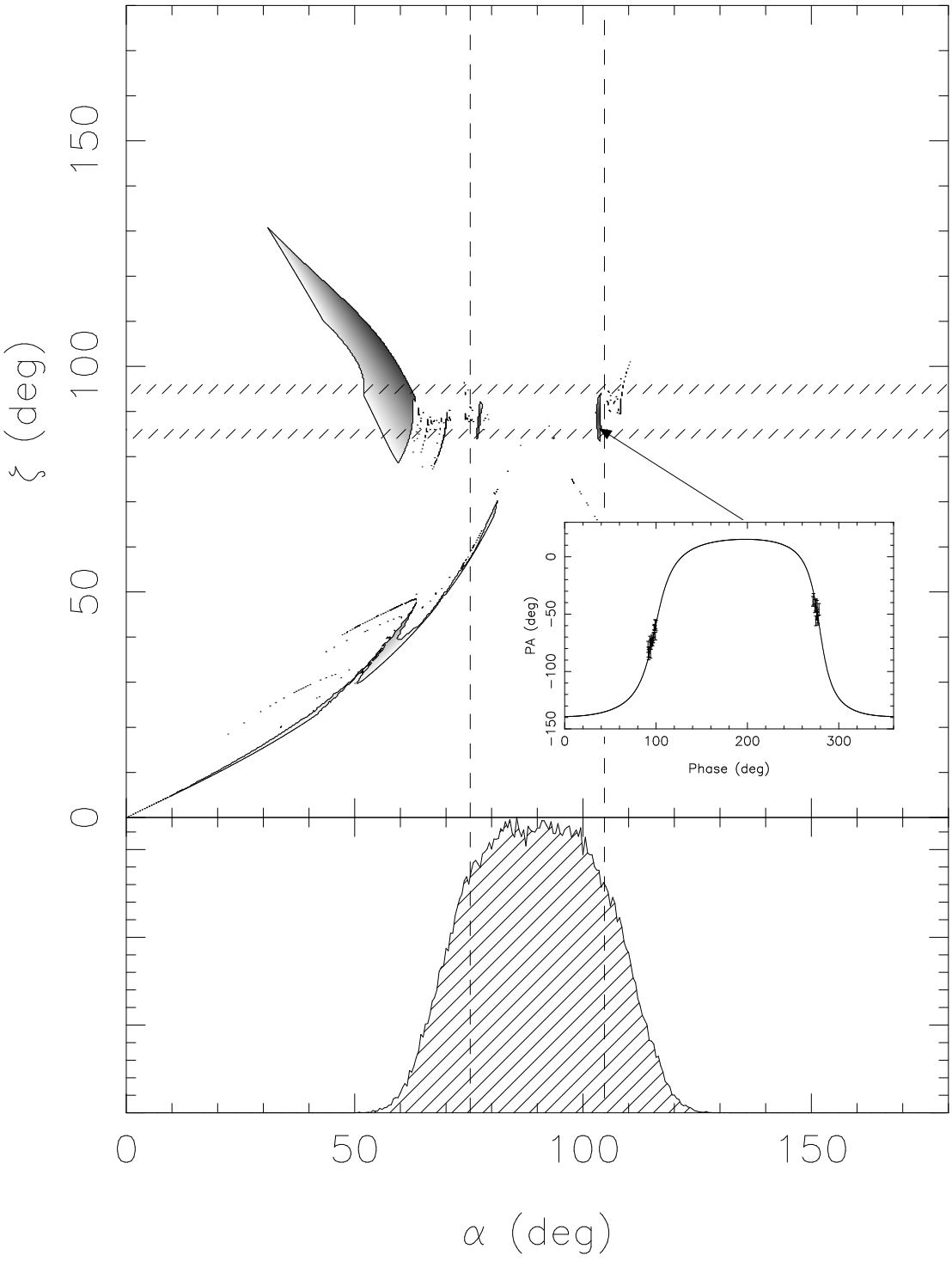

Figure 4.5: System geometry for PSR J2053+4650 as derived from least-squares-fit of the Rotating Vector Model to the position angle of the linearly polarised emission. See Figure 4.4 and text for details.

is affected by its transverse motion as:

$$\frac{\dot{P}}{P} = \frac{1}{c} \times \frac{v_{\rm t}^2}{d}\,, \tag{4.2}$$

where c is the speed of light. As can be seen from Table 4.2, currently the precision of the determined Shklovskii contribution is low for both MSPs: almost 1σ for PSR J2045+3633 and 3σ for PSR J2053+4650. However, they are two orders of magnitude below ($\sim 10^{-21}$ s) the observed $\dot{P}$ values ($\sim 10^{-19}$ s), so they do not affect $\dot{P}$ significantly. Nevertheless, we used the corrected values for estimating the magnetic field strengths and the characteristic ages.

4.5.3 Mass measurements and the nature of the companions

The masses of the components of the system are related to each other and to the Keplerian parameters of the orbit through the mass function (e.g. Lorimer & Kramer, 2012):

$$f(M_p, M_c) = \frac{(M_c \sin i)^3}{(M_p + M_c)^2} = \frac{4\pi^2}{T_\odot}\frac{x^3}{P_b^2}, \tag{4.3}$$

where M_p and M_c are the pulsar and companion masses in units of a solar mass, i is the orbital inclination, x is the projected semi-major axis of the orbit in light seconds and $\mathrm{T}_\odot \equiv \mathrm{GM}_\odot \mathrm{c}^{-3} = 4.9254909476412675\,\mu$s is a solar mass in time units (in the latter expression c is the speed of light and G is Newton's gravitational constant). If two more equations with the same three unknown variables, M_p, M_c and $\sin i$, become available, it is possible to determine the masses of the pulsar and its companion. These equations can be found within the so-called Post-Keplerian (PK) formalism where a set of relativistic additions to the classical Keplerian parameters can be parameterised in a theory-independent way in various timing models.

If we assume GR to be the correct theory of gravity, then these Post-Keplerian (PK) parameters (such as the orbital period derivative $\dot{P}_b$, the advance of periastron $\dot{\omega}$, the gravitational redshift γ and the range r and shape s of the Shapiro delay) relate the component masses and the Keplerian parameters (see Taylor & Weisberg 1982), thus, providing extra equations complementing Eq. 4.3. If two PK parameters are available, we can determine the component masses, if more PK parameters are available we can test the self-consistency of GR and other theories of gravity.

The total mass of the system can be obtained from the measurement of the periastron advance, $\dot{\omega}$, according to:

$$M_{\rm tot} = \frac{1}{T_\odot}\left[\frac{\dot{\omega}}{3}(1-e^2)\right]^{\frac{3}{2}}\left(\frac{P_{\rm b}}{2\pi}\right)^{\frac{5}{2}}. \tag{4.4}$$

The component masses come from the measurement of the Shapiro delay. In the DD parameterisation (Damour & Deruelle, 1985, 1986), this is described by the "Range" $r = T_\odot M_c$ and "Shape" $s = \sin i$ parameters. In DDH parameterisation (Freire & Wex, 2010), we have the orthometric ratio and amplitude, respectively:

$$\varsigma = \frac{\sin i}{1+\cos i},\; h_3 = r\,\varsigma^3. \tag{4.5}$$

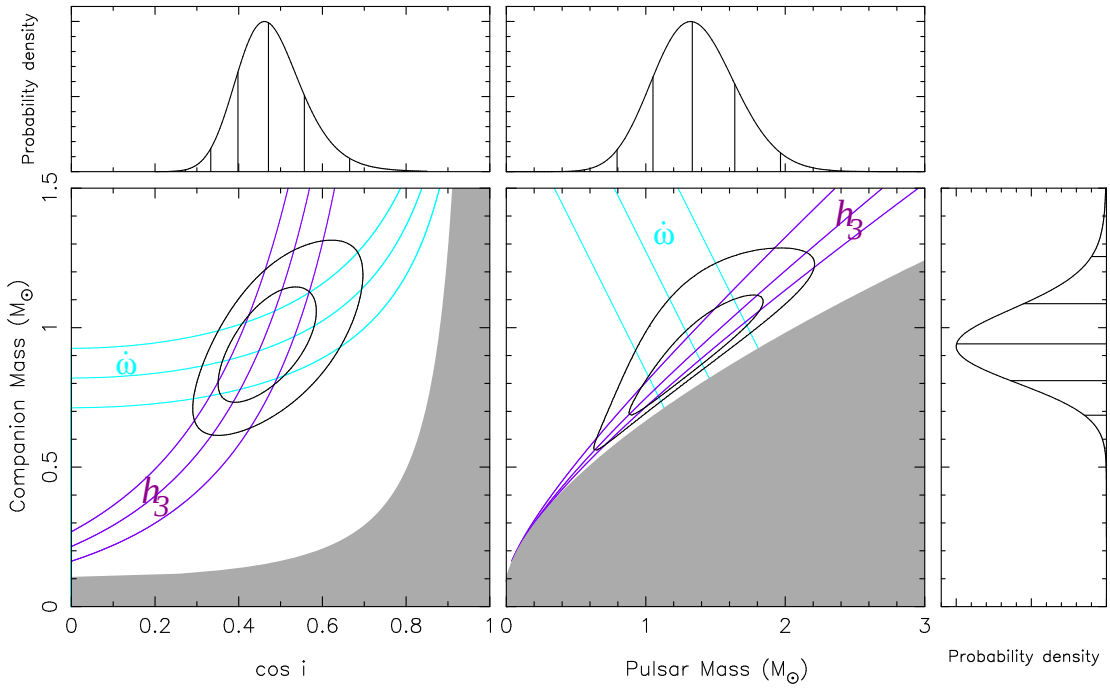

Figure 4.6: Constraints on the masses of the components and the orbital inclination angle for PSR J2045+3633. Each triplet of lines corresponds to the median values and $\pm 1\sigma$ uncertainties of the post-Keplerian parameters obtained within the DDH model: the rate of advance of periastron $\dot{\omega}$ (cyan) and the orthometric amplitude of the Shapiro delay, h_3 (purple) (the triplet for the orthometric ratio of the Shapiro delay ς is removed from the figure for better visual perception as it covers a wide region which includes both regions for $\dot{\omega}$ and h_3) The contour levels contain 68.27 and 95.45% of the 2-D probability density functions (pdfs) derived from the quality of the timing solution at each point on the M_c - $\cos i$ plane using the Shapiro delay together with an assumption that $\dot{\omega}$ can be fully described by general relativity to constrain the masses. The left plot shows the M_c - $\cos i$ plane with the gray region excluded by the physical constraint $M_p > 0$. The right plot shows M_c - M_p plane with the gray region excluded by the mathematical constraint $\sin i \leq 1$. The top plots depict probability density functions for $\cos i$, M_p and the right marginal plot - for M_c, derived from marginalizing the 2-D pdf in the main panel for these quantities.

The latter parameterisation has the advantage of a smaller correlation between the parameters and also better describes the regions of the $M_c - \sin i$ plane where the parameters of the system are. For this reason, when other PK effects are also known, then this parameterisation provides a better test of GR.

4.5.3.1 PSR J2045+3633

For PSR J2045+3633 we have used the DDH model to measure the PK parameters $\dot{\omega}$, h_3 and ς. From the measurement of $\dot{\omega}$ we derived the total mass $M_{\rm tot} = 2.28(45)\,M_\odot$ using Eq. 4.4.

We can estimate approximately the masses of the individual components from the

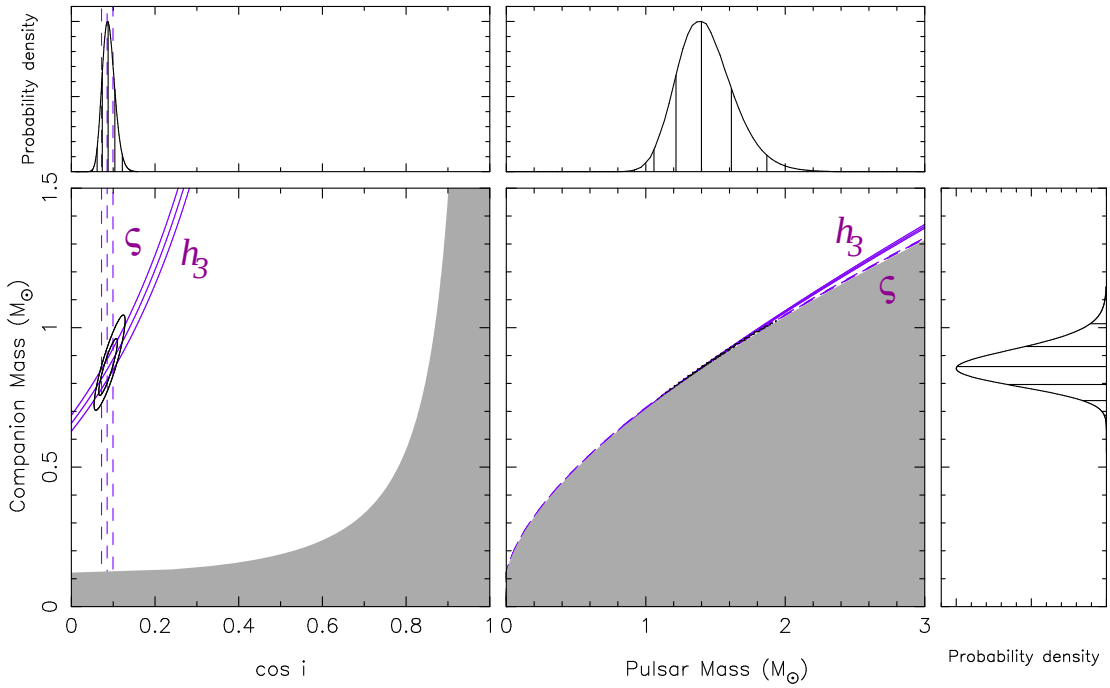

Figure 4.7: Constraints on the masses of the components and the orbital inclination angle for PSR J2053+4650 in the same manner as in Fig. 4.6. The only difference is in the PK parameters used to constrain the masses: in this case the orthometric amplitude h_3 (solid purple) and the orthometric ratio of the Shapiro delay ς (dashed purple).

intersection of the h_3 and $\dot{\omega}$ curves[4] in Fig. 4.6. To do this robustly, we performed a Bayesian χ^2 analysis in the $M_c - \cos i$ plane in the fashion described in Splaver et al. (2002). For each point in this plane, we calculated the Shapiro delay parameters and the rate of advance of periastron using the specifications of general relativity. Keeping these fixed, we fitted for the spin, astrometric and Keplerian parameters tracking the post-fit χ^2 (see Fig. 4.6). From this χ^2 map we derived a 2-D probability distribution function (pdf) that was then translated into a 2-D pdf in the $M_c - M_p$ plane using Eq. 4.3. We then marginalize the 2-D pdfs to derive 1-D pdfs for M_c, $\cos i$ and M_p.

As can be seen from Table 4.2 and Fig. 4.6, the current precision of the Shapiro delay measurement, even combined with $\dot{\omega}$, does not allow us to constrain the masses precisely. This is a consequence of the orbit not being highly inclined, with $i = 62^{+5}_{-6}{}^{\circ}$. The best-fit mass values within 1σ-band are: $M_p = 1.33^{+0.30}_{-0.28}\,M_\odot$, $M_c = 0.94^{+0.14}_{-0.13}\,M_\odot$. The mass of the pulsar is not yet precise enough for any conclusions, however, it is clear that the companion is either a heavy CO or ONeMg WD, as implied by the large mass function of the system.

Continued timing with a special focus on observations near the superior conjunction will greatly improve the precision of the Shapiro delay detection, but even greater improvements will arise from the fast-improving measurement of $\dot{\omega}$, for which the

[4]Note that this is not possible in the r-s parameterisation, where constraints from the measurement of $\sin i$ and M_c are too wide to give any useful mass constraints.

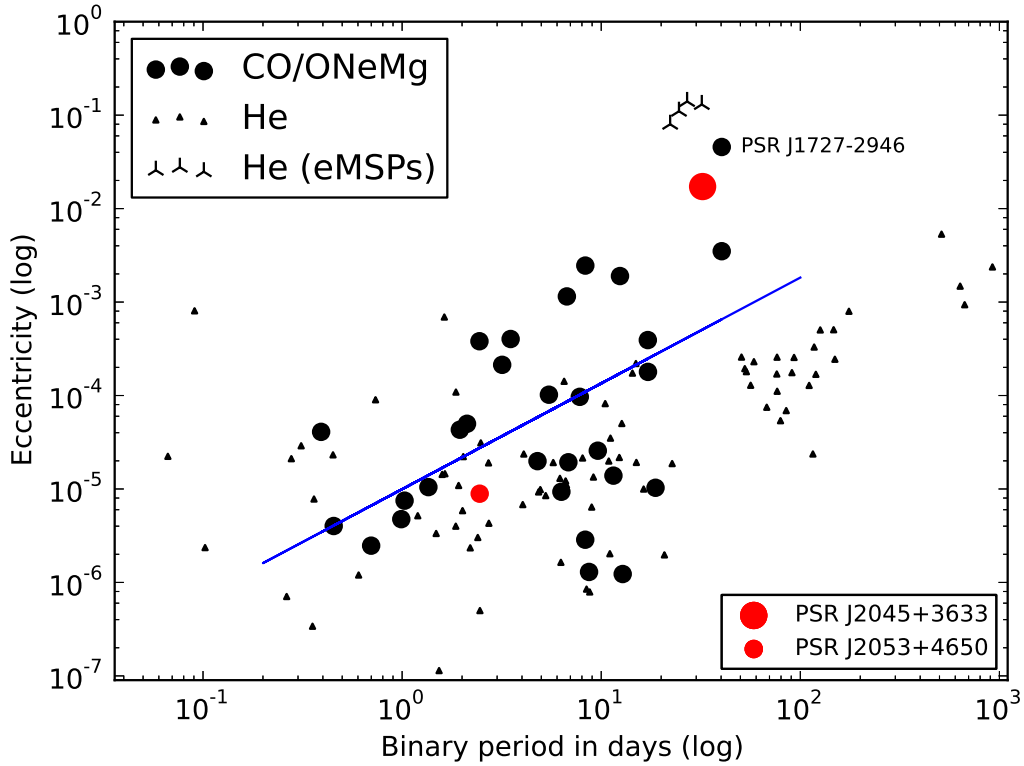

Figure 4.8: Location of the two new MSPs on the $P_b - ecc$ diagram for the population of binary pulsars with WD companions and spin periods < 100 ms. The blue line is a linear regression fit for IMBPs (CO/ONeMg WD companions).

uncertainty is proportional to $T^{-3/2}$ (where T is the temporal span of the timing data).

Given the large orbital period of PSR J2045+3633 ($P_b = 32.3$ days), this system probably did not evolve via CE (if so, the envelope of the WD progenitor star must have been very weakly bound at the onset of the CE because of the small degree of orbital in-spiral). This system might instead have formed by stable Case B RLO in an IMXB system (Tauris et al., 2000). It is worth noting that the orbital configuration is also compatible with theoretical modelling of IMXBs producing pulsars with massive WDs. However, the large orbital period could possibly be accounted for by changing the assumptions of the specific orbital angular momentum carried away by the material lost from the system during RLO.

4.5.3.2 PSR J2053+4650

For this system, the high orbital inclination and large companion mass yield a strong signature of the Shapiro delay (Fig. 4.3) allowing mass measurements from this effect alone. We fitted the timing data with both DD and DDH models. The masses

derived from the range and shape parameters measured within the DD model are consistent with the values obtained from a Bayesian analysis (Fig. 4.7) similar to that described in Section 4.5.3.1 performed within the DDH model: $M_p = 1.40^{+0.21}_{-0.18}\,M_\odot$, $M_c = 0.86^{+0.07}_{-0.06}\,M_\odot$. The companion is most likely a heavy CO WD, or possibly an ONeMg WD. For this system, although we will not be able to measure any other PK parameters in the near future (a couple of years); it is possible that $\dot{\omega}$ might be measurable in the distant future (tens of years).

The combination of a short orbital period ($P_b = 2.45$ days) and a massive WD companion suggests that this system formed via CE evolution from an IMXB with a donor star on the asymptotic giant branch, e.g. following the scenario suggested by van den Heuvel (1994).

4.5.4 Eccentricity of PSR J2045+3633

For the majority of known IMBPs observed, eccentricities range from 10^{-6} to 10^{-3} (see Fig. 4.8). This is certainly the case for one of our new binary systems, PSR J2053+4650. However, some systems have larger eccentricities, one of them being PSR J0621+1002 (Splaver et al., 2002) which has $e = 0.00245744(5)$. In 2015, a presumed IMBP, PSR J1727−2946, was discovered with an orbital period of 40 days and an eccentricity of $e = 0.04562943(16)$ (see Lorimer et al., 2015), even larger than that of PSR J2045+3633 ($e = 0.01721244(5)$).

Looking at Fig. 4.8, based on the data from the ATNF catalogue[5], we could in principle say that the relatively high orbital eccentricities of PSR J2045+3633 and PSR J1727−2946 are the result of a smooth trend of increasing orbital eccentricity with orbital period among the systems with massive WD companions. Indeed, the correlation shown as a blue line in Fig. 4.8 was obtained as a result of a linear regression fit to the observed data (in logarithmic scale) with $R^2 = 0.515$, $p = 0.003$ and $stderr = 0.35$. This low significance for the regression is not surprising if we take into account the large spread in eccentricities for a given orbital period.

Given the three different formation channels proposed for IMBPs (see Section 1), the scatter in Fig. 4.8 could simply reflect different origins of these systems.

It is interesting to note that the orbital periods of PSR J2045+3633 and PSR J1727−2946 are close to those of the anomalously eccentric MSP–He WD systems (eMSPs): PSR J1946+3417 (Barr et al., 2013, 2017), PSR J2234+0611 (Deneva et al., 2013b; Antoniadis et al., 2016b), PSR J1950+2414 (Knispel et al., 2015) and PSR J0955−6150 (Camilo et al., 2015). Very few (if any) circular systems are observed in this orbital period range (sometimes dubbed the "Camilo gap" first noticed in Camilo, 1996). Although we cannot see any common physical mechanism, it is possible that for IMBPs there might also be an eccentricity anomaly at these orbital periods. This would be very surprising: all of the scenarios put forward to explain the eccentric MSP–He WD systems with orbital periods between 22 and 32 days (Freire & Tauris, 2014; Antoniadis, 2014; Jiang et al., 2015) make those predictions for low-mass He WD companions only.

[5] http://www.atnf.csiro.au/people/pulsar/psrcat/; Manchester et al. (2005)

Further discoveries of IMBPs with these orbital periods and larger will be necessary for determining whether IMBPs follow a smooth trend in the $P_b - ecc$ diagram, or whether there possibly is a universal eccentricity anomaly for all binary pulsars with orbital periods between 20 and 40 days.

4.6 Summary and conclusions

We have presented two binary MSPs discovered in the Northern High Time Resolution Universe pulsar survey. As shown by the timing solutions, we have added two new members to the population of intermediate-mass binary pulsars. While PSR J2053+4650 is a standard representative of this population, PSR J2045+3633, with its relatively large eccentricity $e = 0.0172$, appears to be atypical (there are only a few other systems with eccentricities of the same order) and especially interesting for studying stellar evolution.

Both systems are promising for precise mass measurements of their components. Current constraints on the pulsar masses are $1.33^{+0.30}_{-0.28}\,M_\odot$ for PSR J2045+3633 and $1.40^{+0.21}_{-0.18}\,M_\odot$ for PSR J2053+4650 where the median values are in agreement with the assumption that the masses of mildly recycled pulsars should be close to their birth values $\sim$1.35 $M_\odot$ since they accreted little matter from their massive companions. The precision of measurements will be improved with further timing. Moreover, in the case of PSR J2045+3633, three post-Keplerian parameters (the periastron advance and two Shapiro delay parameters) can be measured with high precision in the near future providing additional constraints. The low rms of timing residuals and sharp profiles of both pulsars suggest that they may be useful for pulsar timing arrays.

Chapter 5

Further projects with the Effelsberg telescope

In this chapter I present the work on two other projects: I contributed to timing of PSR J1946+3417 and follow-up of FRB 150418 with the Effelsberg telescope.

5.1 Timing of PSR J1946+3417

This section is devoted to the study of PSR J1946+3417, a millisecond pulsar in an unusually eccentric orbit with an intermediate mass He WD companion. My main contribution here was the acquisition, reduction and analysis of high-quality timing data using the Effelsberg radio telescope. I briefly introduce the system explaining why it is interesting in Section 5.1.1, describe my work in Section 5.1.2 and give the main scientific results that followed from it in Section 5.1.3.

The full author list of the paper "A massive millisecond pulsar in an eccentric binary" published in Monthly Notices of the Royal Astronomical Society, 2017, Vol. 465, Is. 2, pp. 1711–1719, is:
Barr E. D., Freire P. C. C., Kramer M, Champion D. J., ***Berezina M.****, Bassa C. G., Lyne A. G., Stappers B. W.*

5.1.1 The mystery of PSR J1946+3417

PSR J1946+3417 (see Fig. 5.1) was the first MSP (P = 3.17 ms) discovery of the Northern High Time Resolution Universe pulsar survey (HTRU-North) (see Barr et al. (2013) and Chapter 3). After a series of follow-up timing observations it became clear that the pulsar was in a relatively eccentric ($e \sim 0.13$) 27-day binary orbit. The mass function (Eq. 4.3) suggested that the companion was light, with a minimum mass of only 0.21 $M_\odot$.

The origin of such a significant eccentricity was immediately puzzling. Unlike globular clusters where eccentric MSPs are quite common due to high stellar densities that enable N-body interactions deforming the orbit, the Galactic disk is expected to mostly host MSP binaries with low eccentricities. According to the commonly accepted model of MSP formation (Alpar et al., 1982; Bhattacharya & van den Heuvel, 1991;

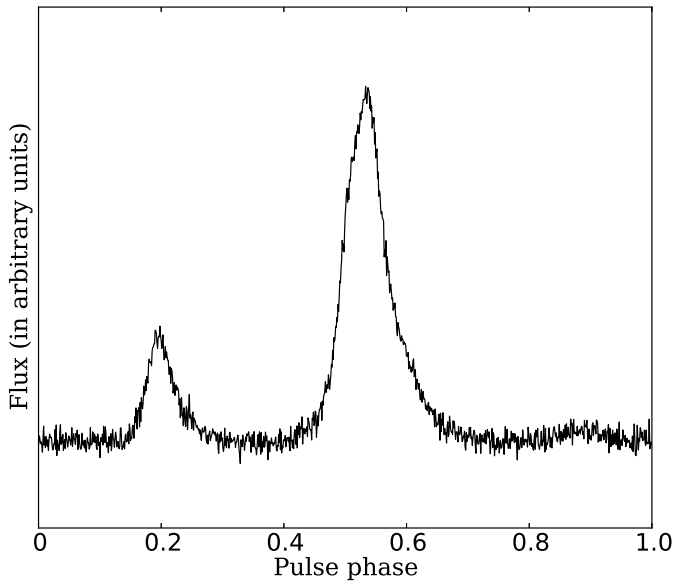

Figure 5.1: The average pulse profile of PSR J1946+3417 obtained by adding the integrated pulse profiles for 28 observations (each of 30-minute duration) performed with the Effelsberg telescope at 1347 MHz.

Tauris & van den Heuvel, 2006), this is a consequence of recycling through the transfer of angular momentum and mass from a companion star in the long period of accretion when tidal forces circularise the orbit to $e \sim 10^{-6}$. For the first time this model was challenged by the discovery of PSR J1903+0327, a 2.15-ms pulsar orbiting a Solar-mass main-sequence star with $e = 0.44$ (Champion et al., 2008). To explain the large eccentricity of PSR J1903+0327, Freire et al. (2011); Zwart et al. (2011); Pijloo et al. (2012) proposed a hypothesis of its formation in a hierarchical triple that was dynamically unstable and where the gravitational interaction between the components has elongated the orbit and ejected the lowest-mass companion.

One of the earliest attempts to explain the puzzle of PSR J1946+3417 involved the same hypothesis of a hierarchical triple. However, this scenario predicted various possible orbital configurations for the leftover binary. After a few similar systems were discovered: PSR J2234+0611 (Deneva et al., 2013b; Antoniadis et al., 2016b), PSR J1950+2414 (Knispel et al., 2015) and PSR J0955−6150 (Camilo et al., 2015), it became clear that their anomalous eccentricities ($e \sim 0.08$–0.14), in combination with a very narrow range of values for the orbital and spin periods (22–32 days and 3–4 ms, correspondingly) and minimum companion masses of ~ 0.19–$0.25\ M_{\odot}$, seem to be more likely a rule than an exception and can not be interpreted (explained) as a result of a chaotic triple system's disruption.

Three main scenarios were proposed to explain the formation of the aforementioned eccentric systems.

1. Such an MSP could be a product of the rotationally-delayed, accretion-induced

collapse (RD-AIC) of a super-Chandrasekhar mass WD. Here the binary orbit acquires its eccentricity due to the sudden release of gravitational binding energy and mass ejection into a disc (Freire & Tauris, 2014).

2. The orbital eccentricity could be caused by the dynamical interaction of the binary with a circumbinary disk resulting from the material expelled by the donor star during hydrogen flash episodes (Antoniadis, 2014).

3. If the neutron star was sufficiently massive and fast spinning at the end of or after the accretion stage, its core density could reach the critical density threshold for quark deconfinement causing its transformation into a strange quark star (SS), and via virial theorem the resulting mass loss induced eccentricity in the orbit (Jiang et al., 2015).

Since all the hypotheses make predictions about the allowed masses of the components of the systems and their kinematic properties, a test of the proposed scenarios becomes possible if these can be determined precisely.

The high eccentricity of the system suggested a high potential for the mass measurement using a combination of the advance of periastron, $\dot{\omega}$, and the Shapiro delay (the same procedure as outlined in Section 4.5.3: for an eccentric orbit the advance of periastron can be easily detected, this gives the total mass of the system (Eq. 4.4) and the Shapiro delay parameters help to "separate" the masses). Aiming for this, systematic timing observations were performed with the Lovell and Effelsberg telescopes in the overall span of almost four years (2012–2016) and additional timing campaigns were done with the Arecibo telescope in June–July 2014 and March–April 2015.

Here we will describe the details of the Effelsberg timing.

5.1.2 Timing observations at Effelsberg and data analysis

A substantial amount of data for this work was collected with the Effelsberg telescope from 2012 to 2016. Timing observations of PSR J1946+3417 were conducted at a central frequency of 1.4 GHz or 1.36 GHz with the use of either the single-pixel 20-cm receiver or seven-pixel 21-cm multibeam receiver, depending on which was installed in the primary focus at any given time. The data in the format of 10-second archive[1] files were recorded with the PSRIX backend (Lazarus et al., 2016) in the coherent-dedispersion real-time folding mode. An approximately once-per-month observing cadence was kept during this period (depending on the availability of the telescope, with some breaks in 2014) with an average duration of a single observation of 30-60 minutes. Additionally, special full-orbit campaigns with more tightly scheduled observations took place in July–August 2013 and April–May 2015. The overall set of data comprised archive files from 95 observing epochs (MJDs 56105–57228). The processing of these files included preliminary preparation, manual RFI-cleaning and production of times-of-arrivals (TOAs).

[1] http://psrchive.sourceforge.net/

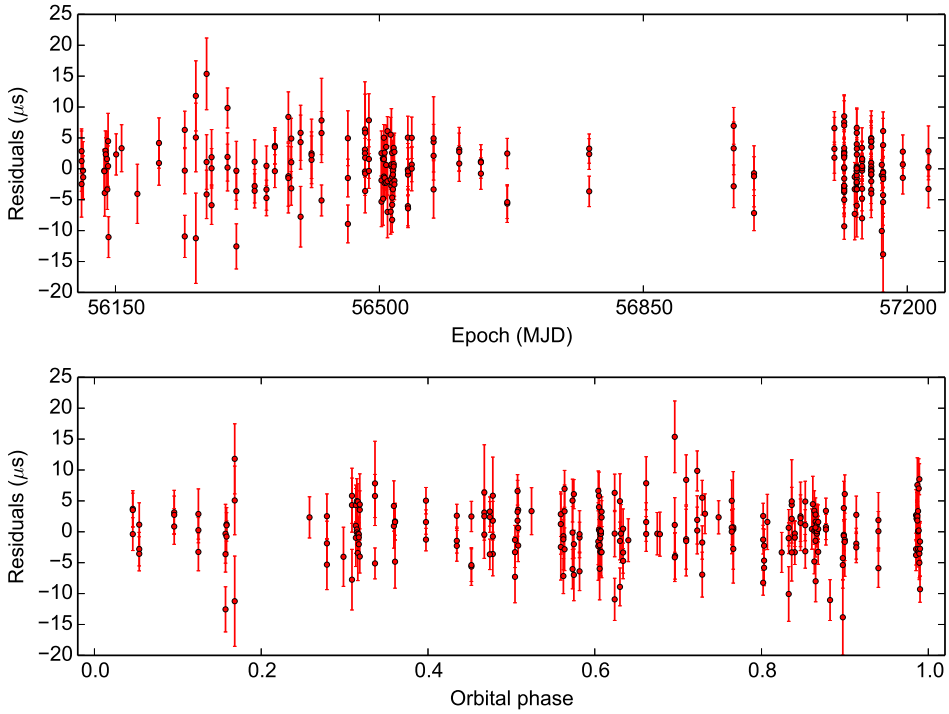

Figure 5.2: The top plot shows the post-fit timing residuals for PSR J1946+3417 as a function of MJD, the bottom plot – as a function of orbital phase. The residuals were obtained from the data taken with the Effelsberg telescopes at a central frequency of 1347 MHz. The errorbars represent the 1-σ uncertainties of TOA measurement.

The preliminary preparation was done with the automated `CoastGuard`[2] pipeline (created for the EPTA/IPTA projects and discussed in detail in Lazarus et al. (2016)) and consisted of the following steps: transferring the data to the local computers (at MPIfR), combining archive files corresponding to different subbands (as the overall available 200-MHz band is divided into eight 25-MHz sub-bands, and every subband is recorded to a separate machine *psrfbs*), performing the polarisation calibration (if possible) and some RFI-cleaning. Then the archive files were visually inspected and manually cleaned of the remaining RFI with the `psrchive` software (Hotan et al., 2004; van Straten et al., 2012). As the last step, every cleaned archive was fully integrated in time and integrated in frequency to leave four channels, and the resultant profiles were cross-correlated with a high-signal-to-noise template generated from the average pulse profile over all observed epochs in a standard way Taylor (1992) using `psrchive` in order to get TOAs. Several TOAs from the earliest and relatively low-signal-to-noise observations (with the TOA error higher than 8 μs) were excluded from the further analysis. This final set of Effeslberg TOAs was combined with the TOAs from the Lovell and Arecibo telescopes and fitting for the spin and orbital parameters was performed with the DD and DDGR models using `TEMPO` and `TEMPO2` .

[2]https://github.com/plazar/coastguard

In Fig. 5.2 we present the TEMPO2 timing residuals obtained by subtracting the time-of arrival values predicted by the DDH model from the measured TOAs for Effelsberg only to demonstrate the quality and spread of those separately. The weighted root-mean square of the residuals is 3.735 μs. As can be seen from the bottom plot, the orbital coverage is almost uniform and the residuals look to be normally distributed.

Though the Arecibo telescope, leading in gain and sensitivity, provided more precise TOAs necessary for precise measurements of the Shapiro delay, the large spread of the Effelsberg and Jodrell Bank observations made them particularly important for constraining the rate of periastron advance and the spin-down rate, as well as sky position and proper motion.

5.1.3 Results and discussion

The overall multi-telescope campaign resulted in a significant detection of the periastron advance and the Shapiro delay. This allowed us to obtain the total mass of the system and the companion mass after fitting for the timing parameters within the DDGR model: $M_{\rm t} = 2.094(22)\,M_\odot$, $M_c = 0.2656(19)\,M_\odot$. From these values the pulsar mass and the inclination angle of the orbit were calculated: $M_p = 1.828(22)\,M_\odot$ and $i = 76.4(6)^\circ$. With this precisely measured mass PSR J1946+3417 becomes the third most massive ($M_p > 1.8\,M_\odot$) pulsar known - after PSR J0348+0432 with $M_p = 2.01(4)\,M_\odot$ (Antoniadis et al., 2013) and PSR J1614−2230 with $M_p = 1.928(17)\,M_\odot$ (Fonseca et al., 2016). A total proper motion measured to be 8.35(21) mas yr^{-1} allowed us to constrain the transverse velocity: $v_t = 200 \pm 60$ km s^{-1}. This value is quite typical for MSPs and is consistent with the measured space velocities given in Hobbs et al. (2005); Gonzalez et al. (2011); Desvignes et al. (2016).

Based on these results, we can re-examine the proposed formation mechanisms:

1. Since the RD-AIC scenario predicts the final neutron star mass to lie within the range: $1.22 < M_p < 1.31\,M_\odot$) and the space velocity of the system to be $\lesssim 10$ km s^{-1}), it can be excluded from further consideration as this prediction is inconsistent with the measured values.

2. The measured values agree well with the prediction of the circumbinary disk model that the masses and velocities should be similar to those of circular binary MSPs. (The observed mass distribution for recycled pulsars recently reviewed by Antoniadis et al. (2016a) goes from 1.3655(21) $M_\odot$(PSR J1807−2500B; Lynch et al., 2012) to 2.01(4) $M_\odot$ (PSR J0348+0432; Antoniadis et al., 2013)) However, there still remain questions concerning the extent to which circumbinary disks can raise the eccentricity (see e.g. Rafikov, 2016).

3. Though the third hypothesis, that of phase transition from neutron star to strange quark star, makes similar predictions about the final mass and velocity distributions, and formally passes the test, it is unlikely to represent the common formation scenario for eccentric MSPs with HeWDs. If we calculate a pre-transition mass of PSR J1946+3417 assuming that the eccentricity was induced

solely due to the mass loss in the form of gravitational binding energy (Bhattacharya, 1991), we get $\sim 2.1\,M_\odot$. According to Jiang et al. (2015), this is high enough $> 1.8\,M_\odot$) to allow the NS-SS transformation. At the same time, a mass of $1.39(1)M_\odot$ has been recently measured for another eccentric MSP with a HeWD companion, PSR J2234+0611 (Antoniadis et al., 2016b), Assuming that PSR J2234+0611 is also the result of a phase transition, the implied post-transition mass would be $\sim 1.6\,M_\odot$. The large difference between the post-transition mass of J1946+3417 and the putative pre-transition mass of J2234+0611 suggests that phase transition can not account for the observed mass distribution unless there are significant differences in the equation of state for these pulsars.

Summing up, we can conclude that the circumbinary disk hypothesis is the only one proposed which is not in conflict with the currently available data. Nevertheless, with just a few systems in our sample, we can draw no strong conclusion as to whether this is the true or only formation channel. Having more such systems and more mass measurements coupled with more theoretical investigations should improve our understanding of their formation.

5.2 Effelsberg follow-up of FRB 150418

This section is devoted to the study of FRB 150418. My main contribution here was processing and analysis of the data taken with the Effelsberg telescope. The phenomenon of FRB is introduced in Section 5.2.1, the details of the original detection of FRB 150408 (based on Keane et al. (2016)) are given in Section 5.2.2, in Section 5.2.3 I describe my work and in Section 5.2.4 I briefly report the main scientific results of the whole project.

The full author list of the paper "The host galaxy of a fast radio burst" published in Nature, 2016, Vol. 530, Is. 7591, pp. 453–456, is:
E. F. Keane, S. Johnston, S. Bhandari, E. Barr, N. D. R. Bhat, M. Burgay, M. Caleb, C. Flynn, A. Jameson, M. Kramer, E. Petroff, A. Possenti, W. van Straten, M. Bailes, S. Burke-Spolaor, R. P. Eatough, B. W. Stappers, T. Totani, M. Honma, H. Furusawa, T. Hattori, T. Morokuma, Y. Niino, H. Sugai, T. Terai, N. Tominaga, S. Yamasaki, N. Yasuda, R. Allen, J. Cooke, J. Jencson, M. M. Kasliwal, D. L. Kaplan, S. J. Tingay, A. Williams, R. Wayth, P. Chandra, D. Perrodin, ***M. Berezina****, M. Mickaliger, C. Bassa*

5.2.1 FRBs

Fast Radio Bursts (FRBs) are a class of radio transients characterized by their bright (with peak flux density from 20 mJy to 128 ± 5 Jy (Ravi et al., 2016)) millisecond-duration pulses and extremely high dispersion measures (DM = 114–2600 $\mathrm{pc\,cm^{-3}}$)

often vastly exceeding those expected from the ionised interstellar medium in our Galaxy. The first FRB was found in 2007 at Parkes (Lorimer et al., 2007). After a few years without any further discoveries, four new FRBs reported by Thornton et al. (2013) opened the era of (more-or-less regular) new detections and, by mid-2018, the population of observed events has reached a few tens[3] and is constantly growing. Currently the Parkes radio telescope holds the record for the number of FRB detections (e.g. Keane et al., 2012; Thornton et al., 2013; Burke-Spolaor & Bannister, 2014; Ravi et al., 2015; Petroff et al., 2015; Champion et al., 2016; Keane et al., 2016). Among the other telescopes where such bursts were also caught are Arecibo (Spitler et al., 2014), Green Bank (Masui et al., 2015), UTMOST (see e.g. Caleb et al., 2017), ASKAP (Bannister et al., 2017; Shannon R. M. et al., 2018) and CHIME (Boyle & Chime/Frb Collaboration, 2018). The majority of FRBs were found at frequencies around 1.4 GHz, determined by the fact that the first discoveries were made within pulsar surveys performed at 21 cm. At the same time, subsequent specified FRB searches succeeded at lower frequencies: UTMOST (see e.g. Caleb et al., 2017) observed FRBs at 843 MHz and CHIME – at 400 MHz (Boyle & Chime/Frb Collaboration, 2018).

FRBs have different pulse widths and morphology: from smeared pulses with noticeable scattering tails to temporally resolved double-peaked structures (Champion et al., 2016). Hundreds of hours have been spent on re-observing the rough positions of known FRBs, aiming to spot more bursts. However, of all the recorded events, only FRB 121102 revealed a repetitive nature, with over a hundred erratic pulses of various temporal and spectral features observed at the same DM (Spitler et al., 2016; Scholz et al., 2016; Law et al., 2017). Unlike the one-time bursts whose coordinates can not be determined precisely within arcminute radio telescope beams, FRB 121102, due to its repetitiveness, allowed for precise localization (up to 100 mas), as well as for redshift measurement and identification of its host galaxy, which appeared to be a dwarf, in a series of observations with the Very Large Array (VLA) and the European VLBI Network (EVN) (Chatterjee et al., 2017; Marcote et al., 2017; Tendulkar et al., 2017). With the further progress in real-time FRB searches with interferometers like ASKAP (Bannister et al., 2017), pinpointing by a discovery pulse will become possible and, hopefully, will help to shed the light on the nature of FRBs.

Currently there is no generally accepted theory regarding what powers these bursts and where they originate from. Other open questions are: whether repeating and non-repeating FRBs represent different populations and whether non-repeating FRBs are truly one-off events or the lack of follow-up detections arises from insufficient sensitivity of our telescopes(Spitler et al., 2016), at least, for some bursts[4]. If non-repeating FRBs are a truly separate class of one-off events, then cataclysmic scenarios such as binary neutron star (or black hole) mergers (Totani, 2013; Mingarelli et al., 2015), collapses of supra-massive neutron stars (Falcke & Rezzolla, 2014) or binary white dwarf mergers

[3]By mid-October 2018, 49 FRBs are reported. The up-to-date list of detected FRBs can be found at http://www.frbcat.org, (Petroff et al., 2016).

[4]At the same time, though the latter can still be possible, the substantial efforts made in FRBs follow-up with different telescopes, hence, different sensitivities, should not be underestimated. Thus, the observed lack of repetitions might indeed prove the one-shot character of these events.

(Kashiyama et al., 2013) seem quite plausible. For the case of repetitiveness, there are models that relate FRBs to supergiant pulses from extragalactic neutron stars (Cordes & Wasserman, 2016) or magnetar flares (Popov & Postnov, 2010; Lyubarsky, 2014; Pen & Connor, 2015). For example, a young magnetar or a young rotating neutron star fueling a luminous PWN at the expenses of either magnetic or rotational energy respectively might be a correct interpretation for the observed persistent radio emission associated with FRB 121102 (Beloborodov, 2017; Kashiyama & Murase, 2017).

5.2.2 FRB 150418: burst and potential afterglow

FRB 150418 was detected within the SUrvey for Pulsars and Extragalactic Radio Bursts (SUPERB) project (Keane et al., 2018) at the Parkes radio telescope on April 18, 2015. The pulse had a peak flux density of 2.2 Jy, assuming the FRB at the centre of the beam, and dispersion measure of 776.2(5) $\mathrm{cm}^{-3}\,\mathrm{pc}$, which is 4.1 times greater than the maximum expected Galactic contribution. The observed pulse width, $w = 0.8(3)\,\mathrm{ms}$, seemed to mostly be a result of dispersive smearing across the 390.625-kHz channels (see Fig. 5.3b), with the intrinsic width not being resolved. The linear polarisation was $8.5 \pm 1.5\%$ and the circular polarisation was consistent with zero (see Fig. 5.3b, 5.3c).

Soon after the detection the SUPERB collaboration initiated a multi-wavelength follow-up in the hope of catching further bursts. Two hours after the FRB detection at Parkes, the observations at 5.5GHz and 7.5GHz were started with the Australia Telescope Compact Array (ATCA). Two variable compact sources were found within the field corresponding to the Parkes beam (FWHM = 14.1arcmin). One of them was identified as a known positive spectral index GHz-peaked spectrum source (Bell et al., 2015) and, thus, was excluded from further consideration. The other source, located 1.944 arcmin from the centre of the Parkes beam, did not seem to be observed at these frequencies or catalogued previously. During the next five observing epochs, it was again detected at 5.5 GHz decaying from 270(50) μJy/beam to 90(2) μJy/beam on timescales of $\sim$ 6 days and then settling around 90(2) μJy/beam. Furthermore, the source was also seen at 7.5 GHz at 180(30)μJy/beam on the first epoch, without showing up during the next epochs of observations (though the emission with flux density $< 80\mu$Jy/beam was not ruled out). Such transient-like behaviour of this source was suggestive of its relation to the FRB as an afterglow.

On 2015 April 19 and April 20, optical observations of the FRB field were carried out with the Subaru and Palomar Telescopes, resulting in identification of an elliptical galaxy WISE 0716−19 at a redshift $0.48 < z < 0.56$ close to the transient's position (within the ATCA's positional uncertainty). Since the transient's quiescence level was consistent with that expected from an early-type galaxy at a redshift $z \simeq 0.5$ (Brown et al., 2011), the galaxy WISE 0716−19 was claimed to be associated with that fading radio source (transient).

Subsequent radio follow-up observations at 1.4 GHz were performed at the Lovell, Effelsberg, Sardinia and Parkes radio telescopes within a few days after the FRB. All the campaigns detected no additional bursts, though not excluding regular emission

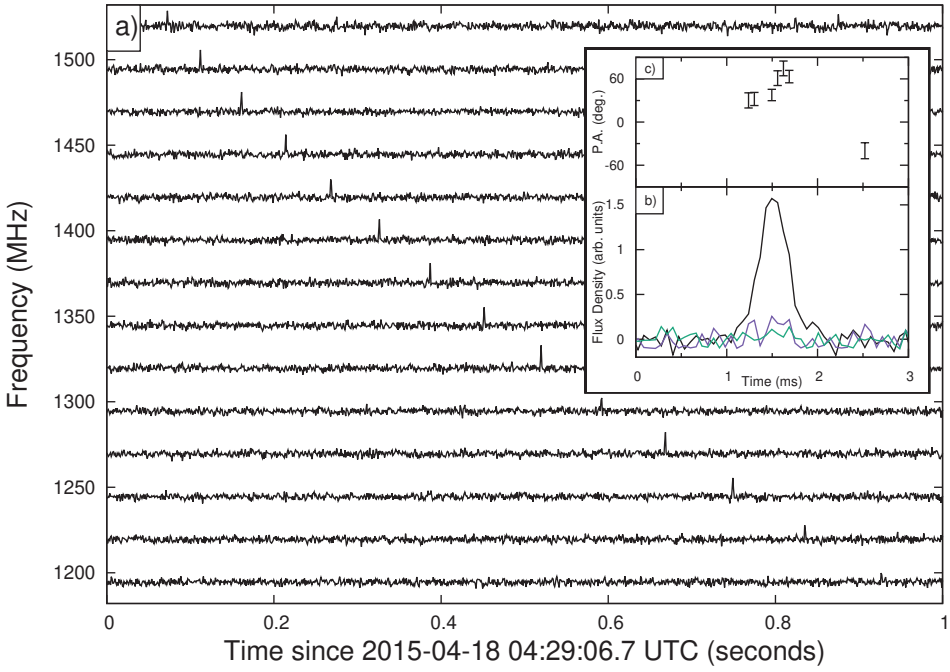

Figure 5.3: The radio signal from FRB 150418 as observed at Parkes on April 18, 2015: a) a waterfall plot of the FRB signal with 15 frequency sub-bands across the Parkes observing bandwidth, showing the characteristic quadratic time-frequency sweep; b) the pulse profile of the FRB signal with the total intensity, linear and circular polarisation shown as black, purple and green lines respectively; c) the polarisation position angle with $1-\sigma$ error bars, for each 64-μs time sample where the linear polarisation was greater than twice the uncertainty in the linear polarisation. The figure and caption are taken from Keane et al. (2016).

at a level much beyond the sensitivity limits. Additionally, the data from Fermi and Swift satellites taken on April 18 and a few months before were checked for possible high-energy counterparts, again with a negative result. As a next step, a longer term follow-up was initiated comprising radio imaging with ATCA and GMRT, high time resolution radio observations with the Lovell telescope, X-ray monitoring with Swift.

Later, in October-November 2015, optical photometry was performed with the Palomar telescope, coupled with optical spectroscopy with the Keck and Subaru telescopes. This helped to measure more precisely the galaxy's redshift: $z = 0.492 \pm 0.008$. The distance consistency between the FRBs's DM (within the uncertainty) and the galaxy's redshift supported the interpretation of the transient being the afterglow of the FRB and galaxy WISE 0716−19 being its host. Based on this assumption, the combination of the FRB's DM and the putative galaxy's redshift was used for estimating the density of ionised baryons in the intergalactic medium, thus, manifesting the first

attempt of direct application of FRBs to verify cosmological models. However, soon afterwards the relation between the FRB and the galaxy became a matter of heated debate (see Section 5.2.4).

5.2.3 FRB 150418: Effelsberg observations and data reduction

As a part of the global follow-up campaign, we observed the sky position of FRB 150418 (as detected at Parkes[5]) with the Effelsberg radio telescope. The observations were done with the use of the seven-beam system designed for the HTRU-North pulsar survey (see Chapter 3). They took place on April 20^{th} 2015 (starting at MJD 57132.706) and lasted for 2.3 hours.

The recorded data were converted from the raw 32-bit format into the 8-bit filterbank format. The resulting filterbank files were split into 6-minute chunks to perform multibeam masking using the corresponding part of the FAST PIPELINE (see Chapter 3.4.3), as for the HTRU-North survey data. This allowed us to remove a large number of spurious signals. Then the files were dedispersed at a wide range of DMs, including the discovery DM ($776.2(5)\,\mathrm{cm}^{-3}\,\mathrm{pc}$) and searched for single pulses both with the PRESTO CPU-based (single_pulse_search.py) and `heimdall` GPU-based software[6]. The example plot with our results from `heimdall` is presented in Fig. 5.4.

For a threshold detection S/N of 6, no dispersed bursts were found at the initially reported FRB position. Given this, we calculated the upper limit (for non-detection) on the intrinsic flux density using the expression similar to the radiometer equation (see Eq. 3.1) but derived by Cordes & McLaughlin (2003) for radio transients. This expression relates the intrinsic flux density, S_i (in Jy), of the pulse whose observed (broadened) width is W_b (in μs) with the detected signal-to-noise ratio $(S/N)_\mathrm{b}$ as:

$$S_\mathrm{i} = \frac{\beta (S/N)_\mathrm{b} (T_\mathrm{rec} + T_\mathrm{sky})}{G W_\mathrm{i}} \sqrt{\frac{W_\mathrm{b}}{n_\mathrm{p} \Delta\nu}}, \tag{5.1}$$

where $\beta = 1.05$ is the signal degradation due to digitisation for 8-bit data, $T_\mathrm{rec} = 21\,\mathrm{K}$ is the receiver temperature (of the central beam), $T_\mathrm{sky} = 11$ K is the sky temperature at the Galactic latitude $b = -3.2348(3)^\circ$ of the detection (scaled from the model of Haslam et al. (1982)), W_i is the intrinsic pulse width (in μs), $G = 1.5\,\mathrm{K\,Jy}^{-1}$ is the telescope gain, $n_\mathrm{p} = 2$ is the number of polarisations summed and $\Delta f = 240$ MHz is the effective bandwidth.

Calculating the broadened pulse width, W_b, according to Eq. 2.4 and assuming the intrinsic width of 832 μs and 54 μs (as restricted by our time resolution), we obtained the following values of the flux density limit for the Parkes FRB position: 0.3 Jy and 4.3 Jy respectively.

For the case of a true association of the FRB and the galaxy, these values should be scaled by ~ 1.11 accounting for the off-axis position of the galaxy within the telescope

[5]The coordinates of the centre of Effelsberg beam 0 (central beam) matched those of the centre of Parkes beam 4 where the burst was initially found. At the same time, the Effelsberg beam 0 is slightly smaller than the Parkes beam 4: 9.96 arcmin against 14.1 arcmin for the half-power beamwidth.

[6]http://sourceforge.net/projects/heimdall-astro/

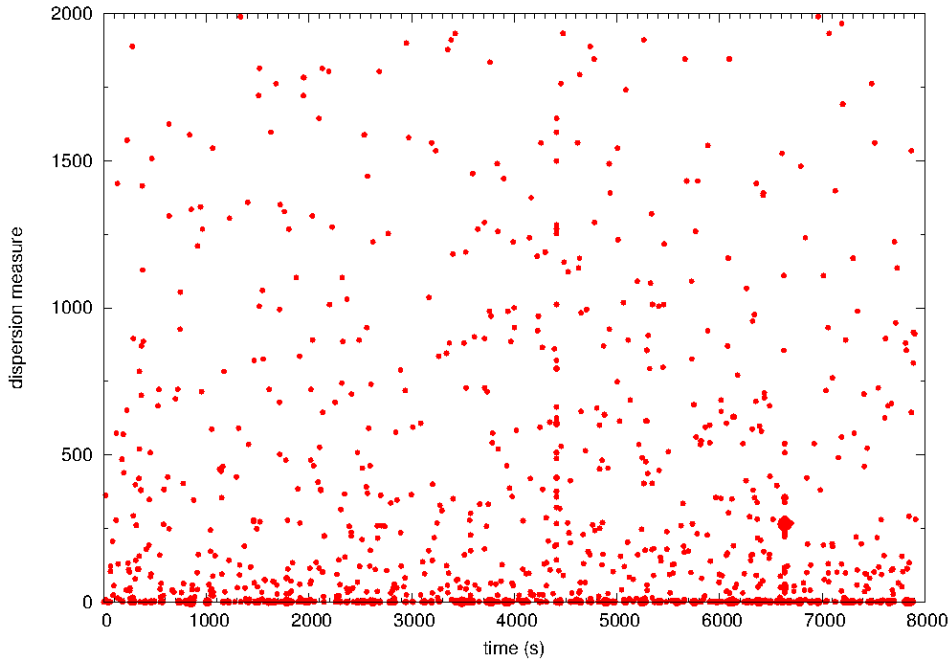

Figure 5.4: Results of the single-pulse search with heimdall software in a range of DMs from 0 to 2000 cm^{-3} pc. No significant events (with S/N > 6) can be identified around DM $= 776.2(5)\,\mathrm{cm}^{-3}$ pc during 8300 s of observations.

beam (0.0324963 deg from the beam centre) during our observations and assuming a Gaussian beam shape. Thus, the corrected flux density limits become 0.33 Jy and 4.7 Jy again for the intrinsic widths of 832 μs and 54 μs respectively.

5.2.4 Open question: discussion to be continued

Soon after its publication (and $\sim$ 10 months after the FRB detection), the position of the transient was observed by Williams & Berger (2016) resulting in a detection of a variable (0.105(21)–0.279(25) mJy at 5.5 GHz ; 0.067(19)–0.199(25) mJy at 7.5.GHz on the timescale of 25 days) radio source. It was claimed to be an active galactic nucleus (AGN) with the flux density variations caused by refractive interstellar scintillation of the Milky Way, and, thus, not related to the FRB. Moreover, the authors argued that the seeming agreement between the DM and redshift distance measurements can actually be preserved for a range of host galaxy redshifts: 0.42–0.65.

Further multi-frequency studies by (Bassa et al., 2016; Giroletti et al., 2016; Johnston et al., 2017) confirmed the presence of a variable compact radio source in the centre of the galaxy WISE J071634.59−190039.2. The observed flux densities were comparable to the later epochs reported in Keane et al. (2016) (see Fig. 5.5). Though the new data were indicative of the source likely being a weak AGN, the analysis done by Johnston et al. (2017) concluded that, despite the small-number statistics, the original 6-epoch light curve (see Keane et al., 2016) could be consistent with that of a

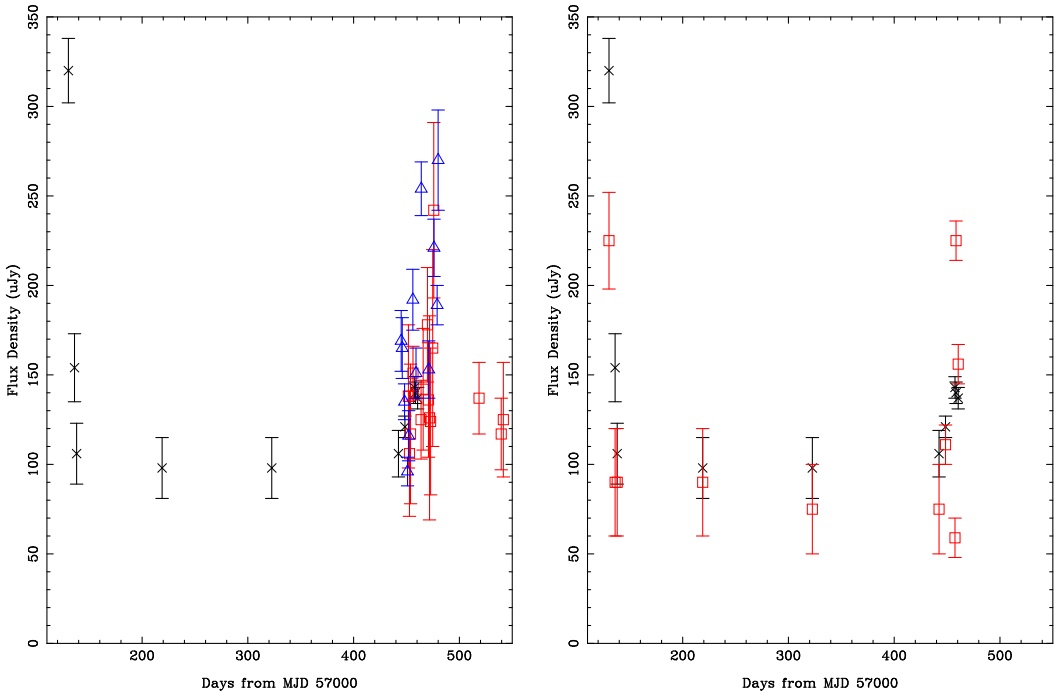

Figure 5.5: The radio light curve of WISE J071634.59−190039.2. Left panel: data taken at 5.5 GHz. Black crosses denote ATCA observations, blue triangles JVLA observations, and red squares VLBA, e-MERLIN and EVN. Right panel: the ATCA data at 5.5 GHz (black crosses) and 7.5 GHz (red squares). The first ATCA observation (on the day of FRB) corresponds to MJD=57130. The figure and caption are taken from Johnston et al. (2017).

fading radio transient. Furthermore, the flux density value, 320(18) mJy, seen in the first epoch (in the data taken two hours after FRB 150418 by ATCA) was "anomalously high" for being likely explained by interstellar scintillations.

The continued discussion around this topic, though casting a doubt on the originally claimed association, leaves the question still open. The lack of principal knowledge about the progenitors and populations of FRBs, as well as the forms of their afterglows, prevents us from ruling out the relation between WISE J071634.59−190039.2 and FRB 150418. Eventually, further monitoring of the FRB field and the galaxy position may bring more clarity.

Chapter 6

Conclusions

6.1 Summary

The major part of this thesis was devoted to exploring the Northern sky in search of pulsars and performing further timing of the discoveries. Thus, I reported on the next stage of the Northern High Time Resolution Universe survey (HTRU-North) for pulsars and fast transients carried out with the Effelsberg telescope, describing the survey's set-up, observations and data processing, and introduced the new pulsars.

During this stage of the survey, the main attention was given to scanning the region of medium Galactic latitudes ($|b| < 15°$), including the low Galactic latitudes ($|b| < 3.5°$), in a 3-minute integration regime. With more than 1100 hours spent on source during the timescale of this thesis, 41% of the total number of mid-latitude pointings were observed, bringing the overall HTRU-North mid-latitude coverage to 50%. The periodicity search with the FAST PIPELINE (without acceleration search) was performed on all the recorded data. In addition, a new, GPU-based pipeline, with implemented acceleration search, was tested on some portions of the data. Among 15 discoveries, all made with the FAST PIPELINE, there are especially useful ones: PSR J2045+3633 and PSR J2053+4650 are mildly-recycled pulsars in binary orbits with massive white dwarf companions, PSR J1951+4721 is a relatively young isolated pulsar. Nine discoveries also showed up in the beams of other surveys within a few years from the start of the HRTU-North. Although we did not perform further timing of these co-detections, we included them into the survey statistics in order to test the accordance between the modelled and the actually observed populations. Currently the total HTRU-North yield numbers 30 pulsars which does not agree with the estimates obtained for 50% of the mid-latitude region. The analysis of known pulsar redetections performed as part of this thesis work showed that our system is less sensitive than we expected, most probably, due to RFI. This could be one of the reasons for the shortage of new discoveries. Additionally, the discrepancy between the expected and observed yields could be a consequence of the inaccuracy in the models used for estimates – the Galactic pulsar population model and the Galactic electron density model `NE2001`. Namely, the recently published new Galactic electron density model `YMW16` places many known pulsars at larger distances from the Earth than does `NE2001`, thus, reducing the theoretical discovery rate for any sensitivity-limited survey.

The most interesting systems found during this stage of the HTRU-North, PSR J2045+3633 and PSR J2053+4650, demonstrated a high potential for measuring the component masses precisely. Aiming to "exploit" the advantageous orbital parameters of these binaries to obtain some post-Keplerian parameters (hence, masses) in a rela-

tively short time, we initiated multi-telescope timing follow-up. This resulted in a 5-σ measurement of the rate of periastron advance and a "hint" (3- and 2-σ measurement of the orthometric amplitude and ratio, respectively) of the Shapiro delay for PSR J2045+3633, and a significant detection of the orthometric amplitude and ratio of the Shapiro delay (22- and 66-σ, respectively) for PSR J2053+4650. Assuming general relativity is the correct theory of gravity, these measurements can be "translated" into the following constraints on the masses: $M_p = 1.33^{+0.30}_{-0.28}\,M_\odot$ and $M_c = 0.94^{+0.14}_{-0.13}\,M_\odot$ for PSR J2045+3633, and $M_p = 1.40^{+0.21}_{-0.18}\,M_\odot$, and $M_c = 0.86^{+0.07}_{-0.06}\,M_\odot$ for PSR J2053+4650. With the already achieved precision we were able to get a preliminary idea about the nature of companions and the evolutionary path for both systems. In a long-term timing perspective, the precision will increase and the new mass measurements will give an opportunity to investigate the formation history (for example, binary interactions during the process of accretion) in more detail.

As part of this thesis, I also presented two other projects carried out with the Effelsberg telescope. One of them involved further timing of the first HTRU-North MSP, PSR J1946+3417. This pulsar is a representative of the currently small-numbered and puzzling population of eccentric binaries with low-mass white dwarf companions. To clarify the eccentric origin of PSR J1946+3417 in particular and get a better understanding of the formation of such systems in general via mass measurements, a more than 4-year timing observations were conducted with different telescopes. Within this campaign, I participated in the Effelsberg observations and worked with the corresponding data. The joint efforts showed that PSR J1946+3417 is one of the most massive neutron stars known to date, with $M_p = 1.828(22)\,M_\odot$. This measurement also allowed us to rule out two of the three suggested evolutionary scenarios, though without making a strong conclusion whether the remaining one is true.

The second supplementary project dealt with one of the newest and most intriguing celestial phenomena – fast radio bursts (FRBs). To test the one-off nature of one particular such event – FRB 150418 originally detected at Parkes – we performed follow-up observations of the FRB field with the Effelsberg telescope as part of an international multi-telescope campaign. Successful detection of new bursts from the same location could also help determine the position of the source more accurately. However, the overall campaign (and the Effelsberg follow-up) did not reveal any additional bursts. At the same time, controversial results came from radio imaging which discovered a conceivably related fading high-frequency radio source (afterglow). The galaxy WISE 0716−19 hosting this afterglow was initially claimed to be the birthplace of FRB 150418, but later, with observations of further variability of the source, this claim was doubted. The work on the processing and analysis of the Effelsberg data, as well as the calculations of the upper limits on the flux density for non-detection, comprised the final scientific section of this thesis.

6.2 Future work

6.2.1 HTRU-North

In this section I will briefly describe the primary tasks for the near future of the HTRU-North survey which, most probably, will be devoted to acquisition and processing of more mid-latitude data (and re-processing of the already taken mid-latitude data).

The recent known pulsar redetections analysis revealed that the survey is less sensitive than expected. Although the reduced sensitivity can be compensated for by increasing the integration time (from 3 to 5 minutes) for the remaining 50 % of mid-latitude pointings, a more efficient RFI rejection still is the first question to be solved. One approach to achieving this is to reconsider the algorithms already in use. For example, the multibeam method can be effectively improved[1] by using a combination of varying thresholds and different numbers of beams. This will boost the detectability of weak spurious signals, as well as RFI coming from outside the telescope beam. Along with this, we can expect better performance of RFI mitigation techniques (both those currently in use and those under development) with the implementation of the new Effelsberg backend enabling synchronous recording of the data from all seven beams, resulting in a lack of time offsets. Another approach involves working with the candidate database acquired by the FAST PIPELINE. For example, these data (as a whole or in portions) could be used as a training set for more advanced machine learning algorithms to perform a more elaborate candidate sifting. Alternatively, analysing the overall (many-year) candidate statistics could allow us to create a "temporal map" of RFI in order to trace the changes in the RFI environment. Identifying periodicities persistent within some particular periods of time could be useful for producing dynamic epoch-dependent zaplists that could complement the usual ones.

To realize the full potential of the survey, it is necessary to include an acceleration search in the pipeline. Newly available computational facilities such as a high-performance CPU cluster (HERCULES) and a GPU Garching cluster will provide a powerful platform for full (but also quick!) processing. Although the FAST PIPELINE was able to find interesting binaries like PSR J1946+3417, PSR J2045+3633 and PSR J2053+4650, an acceleration pipeline will be sensitive to even more exotic systems.

6.2.2 Further timing of PSR J2045+3633 and PSR J2053+4650

Continued timing of PSR J2045+3633 and PSR J2053+4650 will improve the precision of their mass measurements. Currently the two MSPs are regularly observed with the Effelsberg, Nançay and Lovell radio telescopes. The new data taken since the publication of Berezina et al. (2017) already should give more significance to the results. Concerning some peculiar strategy, for PSR J2045+3633, we plan another Arecibo campaign with a special attention to the superior conjunction. Accounting for the time passed since the previous one, the new measurements will provide a ~ 5 times improvement, allowing the pulsar mass to be determined with a lower than $0.1\,M_{\odot}$

[1] A number of more advanced multi-beam methods are being tested as part of another PhD project

uncertainty. For PSR J2053+4650 we do not expect such a boost in precision within the next 5–7 years assuming the current level of technologies. However, it is possible that rapid technological advances (for example, implementation of ultra-broadband receivers) could potentially contribute to a faster progress, opening new parameter space for experiments, like, for example, testing theories of gravity.

6.2.3 FRB searches

Though searching for FRBs was not the main subject of this thesis, it is worth recalling that originally HTRU-North was designed as a hunt for both pulsars and transients (including FRBs). The main goals of FRB surveys are to increase the known FRB population and uncover the nature of these events. To meet the first goal, it is necessary to monitor large areas of sky simultaneously in order to increase the chances of witnessing a burst. To move towards the second goal, it is necessary to know the event's sky position precisely in order to identify its host galaxy.

First-generation surveys are/were limited by their small instantaneous fields of view and poor localisation capability. The situation is changing with the implementation of new observational facilities and techniques. A good example of state-of-the-art systems are phased array feeds (PAFs). PAFs have a much larger field of view and provide more opportunities for determining the position of the burst than single- or multi-beam feeds. This kind of receiver is already in use at next-generation telescopes like ASKAP[2] and traditional large single dishes like Effelsberg.

Among the instruments promising to make a breakthrough in the near future are the semi-cylindrical CHIME[3] telescope and the array telescopes MeerKAT[4] and SKA[5] (the Square Kilometre Array). Operating at low frequences, CHIME will not provide precise localisation, however, it does have an enormous field of view and will quickly increase the detected population of FRBs. SKA and its pathfinder MeerKAT will perform highly sensitive FRB surveys utilizing the core of the telescope. If a burst is triggered in real time, the raw data from the longest baselines can also be saved and used to localise the FRB with the full resolution of the array.

Future surveys will process and search the data in real time. In addition to the already mentioned array localisation, that allows triggering multi-frequency follow-up with the hope to observe related events at other frequencies, for example, afterglows. The detection of such events can be important for finding the key to the FRB mistery.

6.3 Closing remarks

The future of pulsar astronomy seems to be bright. With more advanced telescopes coming into play over the next ten years, new Galactic (and, possibly, extragalactic) horizons will be opened for exploration. Petabytes of new data will be taken to be

[2] https://www.atnf.csiro.au/projects/askap/index.html
[3] https://chime-experiment.ca/
[4] http://www.ska.ac.za/science-engineering/meerkat/
[5] https://skatelescope.org/

processed using innovative techniques and new computational resources. To deal with billions of candidates expected to be identified by processing pipelines, more comprehensive machine learning algorithms will be developed. In the final result, all these grandiose efforts will inevitably be rewarded with new discoveries, among which we will probably see many unexpected ones that will give a new impetus to the further progress of science.

Bibliography

Alpar M. A., Cheng A. F., Ruderman M. A., Shaham J., 1982, Nature, 300, 728 (Cited on page 101.)

Ambartsumyan V. A., Saakyan G. S., 1960, AZh, 37, 193 (Cited on page 1.)

Antoniadis J., 2014, ApJ, 797, L24 (Cited on pages 99 and 103.)

Antoniadis J., et al., 2013, Science, 340, 448 (Cited on page 105.)

Antoniadis J., Tauris T. M., Ozel F., Barr E., Champion D. J., Freire P. C. C., 2016a, preprint, (arXiv:1605.01665) (Cited on page 105.)

Antoniadis J., Kaplan D. L., Stovall K., Freire P. C. C., Deneva J. S., Koester D., Jenet F., Martinez J. G., 2016b, ApJ, 830, 36 (Cited on pages 99, 102 and 106.)

Archibald R. F., et al., 2016, ApJ, 819, L16 (Cited on page 7.)

Arons J., 1998, in Shibazaki N., ed., Neutron Stars and Pulsars: Thirty Years after the Discovery. Tokyo: Univ. Acad. Press, p. 339 (Cited on page 18.)

Arzoumanian Z., Gotthelf E. V., Ransom S. M., Safi-Harb S., Kothes R., Landecker T. L., 2011, ApJ, 739, 39 (Cited on page 7.)

Ashworth M., Lyne A. G., Smith F. G., 1983, Nature, 301, 313 (Cited on page 61.)

Baade W., Zwicky F., 1934, Proceedings of the National Academy of Science, 20, 259 (Cited on page 1.)

Backer 1970, Nature, 228, 42 (Cited on page 21.)

Bahcall J. N., Wolf R. A., 1965, ApJ, 142, 1254 (Cited on page 2.)

Bailes M., et al., 1994, ApJ, 425, L41 (Cited on page 81.)

Bannister K. W., et al., 2017, ApJ, 841, L12 (Cited on page 107.)

Barr E. D., 2012, PhD thesis, Rheinische Friedrich-Wilhelms-Universität Bonn, http://hss.ulb.uni-bonn.de/2013/3180/3180.htm (Cited on pages 54 and 59.)

Barr E. D., et al., 2013, MNRAS, 435, 2234 (Cited on pages 47, 52, 54, 67, 68, 81, 82, 84, 99 and 101.)

Barr E. D., Freire P. C. C., Kramer M., Champion D. J., Berezina M., Bassa C. G., Lyne A. G., Stappers B. W., 2017, MNRAS, 465, 1711 (Cited on pages 82 and 99.)

Barsdell B. R., Barnes D. G., Fluke C. J., 2010, MNRAS, 408, 1936 (Cited on page 61.)

Barsdell B. R., Bailes M., Barnes D. G., Fluke C. J., 2012, in Ballester P., Egret D., Lorente N. P. F., eds, Astronomical Society of the Pacific Conference Series Vol. 461, Astronomical Data Analysis Software and Systems XXI. p. 37 (arXiv:1112.0065) (Cited on page 61.)

Bassa C. G., et al., 2016, MNRAS, 463, L36 (Cited on page 111.)

Belczynski K., Kalogera V., Bulik T., 2002, ApJ, 572, 407 (Cited on pages 53 and 82.)

Bell Burnell S. J., 1977, in Papagiannis M. D., ed., Annals of the New York Academy of Sciences Vol. 302, Eighth Texas Symposium on Relativistic Astrophysics. p. 685, doi:10.1111/j.1749-6632.1977.tb37085.x (Cited on page 3.)

Bell M. E., Huynh M. T., Hancock P., Murphy T., Gaensler B. M., Burlon D., Trott C., Bannister K., 2015, MNRAS, 450, 4221 (Cited on page 108.)

Beloborodov A. M., 2017, ApJL, 843, L26 (Cited on page 108.)

Berezina M., et al., 2017, MNRAS, 470, 4421 (Cited on page 115.)

Beskin V. S., Gurevich A. V., Istomin Y. N., 1993, Physics of the pulsar magnetosphere. Cambridge, UK: Cambridge University Press (Cited on page 4.)

Beskin V. S., Istomin Y. N., Philippov A. A., 2013, Physics-Uspekhi, 56, 164 (Cited on page 4.)

Beskin V. S., Chernov S. V., Gwinn C. R., Tchekhovskoy A. A., 2015, Space Science Reviews, 191, 207 (Cited on page 5.)

Bhattacharya D., 1991, Physics Reports, 203, 1 (Cited on page 106.)

Bhattacharya D., 1995, JAA, 16, 217 (Cited on page 19.)

Bhattacharya D., van den Heuvel E. P. J., 1991, Physics Reports, 203, 1 (Cited on pages 80 and 101.)

Bhattacharya D., Wijers R. A. M. J., Hartman J. W., Verbunt F., 1992, A&A, 254, 198 (Cited on page 18.)

Bildsten L., et al., 1997, ApJS, 113, 367 (Cited on page 80.)

Boyle P. C., Chime/Frb Collaboration 2018, The Astronomer's Telegram, 11901 (Cited on page 107.)

Brown M. J. I., Jannuzi B. T., Floyd D. J. E., Mould J. R., 2011, ApJ, 731, L41 (Cited on page 108.)

Burke-Spolaor S., Bailes M., 2010, MNRAS, 402, 855 (Cited on page 20.)

Burke-Spolaor S., Bannister K. W., 2014, ApJ, 792, 19 (Cited on page 107.)

Burke-Spolaor S., et al., 2011, MNRAS, 416, 2465 (Cited on pages 20 and 21.)

Caleb M., et al., 2017, MNRAS, 468, 3746 (Cited on page 107.)

Cameron A. G., 1959, ApJ, 130, 884 (Cited on page 1.)

Cameron A. D., et al., 2018, MNRAS, 475, L57 (Cited on page 24.)

Camilo F., 1996, in Johnston S., Walker M. A., Bailes M., eds, Astronomical Society of the Pacific Conference Series Vol. 105, IAU Colloq. 160: Pulsars: Problems and Progress. p. 539 (Cited on pages 81 and 99.)

Camilo F., Lorimer D. R., Freire P., Lyne A. G., Manchester R. N., 2000, ApJ, 535, 975 (Cited on page 42.)

Camilo F., Ransom S. M., Halpern J. P., Reynolds J., Helfand D. J., Zimmerman N., Sarkissian J., 2006, Nature, 442, 892 (Cited on page 19.)

Camilo F., Ransom S. M., Halpern J. P., Reynolds J., 2007, ApJ, 666, L93 (Cited on page 20.)

Camilo F., Ransom S. M., Chatterjee S., Johnston S., Demorest P., 2012, ApJ, 746, 63 (Cited on page 7.)

Camilo F., et al., 2015, ApJ, 810, 85 (Cited on pages 99 and 102.)

Champion D. J., et al., 2008, Science, 320, 1309 (Cited on page 102.)

Champion D. J., et al., 2016, MNRAS, 460, L30 (Cited on page 107.)

Chandrasekhar S., 1935, MNRAS, 95, 207 (Cited on page 1.)

Chatterjee S., et al., 2017, Nature, 541, 58 (Cited on page 107.)

Chen K., Ruderman M., 1993, ApJ, 402, 264 (Cited on page 18.)

Chiu H.-Y., 1970, Publications of the Astronomical Society of the Pacific, 82, 487 (Cited on pages 5 and 12.)

Chiu H. Y., Canuto V., 1971, ApJ, 163, 577 (Cited on page 4.)

Chiu H.-Y., Salpeter E. E., 1964, Phys. Rev. Lett., 12, 413 (Cited on page 2.)

Coenen T., et al., 2014, A&A, 570, A60 (Cited on page 82.)

Cordes J. M., 1978, ApJ, 222, 1006 (Cited on page 8.)

Cordes J. M., Lazio T. J. W., 2002, ArXiv Astrophysics e-prints, (Cited on pages 12, 32, 66, 89 and 93.)

Cordes J. M., McLaughlin M. A., 2003, ApJ, 596, 1142 (Cited on page 110.)

Burke-Spolaor S., et al., 2011, MNRAS, 416, 2465 (Cited on pages 20 and 21.)

Caleb M., et al., 2017, MNRAS, 468, 3746 (Cited on page 107.)

Cameron A. G., 1959, ApJ, 130, 884 (Cited on page 1.)

Cameron A. D., et al., 2018, MNRAS, 475, L57 (Cited on page 24.)

Camilo F., 1996, in Johnston S., Walker M. A., Bailes M., eds, Astronomical Society of the Pacific Conference Series Vol. 105, IAU Colloq. 160: Pulsars: Problems and Progress. p. 539 (Cited on pages 81 and 99.)

Camilo F., Lorimer D. R., Freire P., Lyne A. G., Manchester R. N., 2000, ApJ, 535, 975 (Cited on page 42.)

Camilo F., Ransom S. M., Halpern J. P., Reynolds J., Helfand D. J., Zimmerman N., Sarkissian J., 2006, Nature, 442, 892 (Cited on page 19.)

Camilo F., Ransom S. M., Halpern J. P., Reynolds J., 2007, ApJ, 666, L93 (Cited on page 20.)

Camilo F., Ransom S. M., Chatterjee S., Johnston S., Demorest P., 2012, ApJ, 746, 63 (Cited on page 7.)

Camilo F., et al., 2015, ApJ, 810, 85 (Cited on pages 99 and 102.)

Champion D. J., et al., 2008, Science, 320, 1309 (Cited on page 102.)

Champion D. J., et al., 2016, MNRAS, 460, L30 (Cited on page 107.)

Chandrasekhar S., 1935, MNRAS, 95, 207 (Cited on page 1.)

Chatterjee S., et al., 2017, Nature, 541, 58 (Cited on page 107.)

Chen K., Ruderman M., 1993, ApJ, 402, 264 (Cited on page 18.)

Chiu H.-Y., 1970, Publications of the Astronomical Society of the Pacific, 82, 487 (Cited on pages 5 and 12.)

Chiu H. Y., Canuto V., 1971, ApJ, 163, 577 (Cited on page 4.)

Chiu H.-Y., Salpeter E. E., 1964, Phys. Rev. Lett., 12, 413 (Cited on page 2.)

Coenen T., et al., 2014, A&A, 570, A60 (Cited on page 82.)

Cordes J. M., 1978, ApJ, 222, 1006 (Cited on page 8.)

Cordes J. M., Lazio T. J. W., 2002, ArXiv Astrophysics e-prints, (Cited on pages 12, 32, 66, 89 and 93.)

Cordes J. M., McLaughlin M. A., 2003, ApJ, 596, 1142 (Cited on page 110.)

Cordes J. M., Wasserman I., 2016, MNRAS, 457, 232 (Cited on page 108.)

Cordes J. M., et al., 2006, ApJ, 637, 446 (Cited on pages 47 and 82.)

Crawford F., Gaensler B. M., Kaspi V. M., Manchester R. N., Camilo F., Lyne A. G., Pivovaroff M. J., 2002, in Slane P. O., Gaensler B. M., eds, Astronomical Society of the Pacific Conference Series Vol. 271, Neutron Stars in Supernova Remnants. p. 41 (arXiv:astro-ph/0111391) (Cited on page 7.)

Damour T., Deruelle N., 1985, Ann. Inst. Henri Poincaré Phys. Théor., 43, 107 (Cited on pages 22 and 95.)

Damour T., Deruelle N., 1986, Ann. Inst. Henri Poincaré Phys. Théor., 44, 263 (Cited on pages 22 and 95.)

Damour T., Esposito-Farèse G., 1998, Phys. Rev. D, 58, 042001 (Cited on page 24.)

Deller A. T., Tingay S. J., Bailes M., Reynolds J. E., 2009, ApJ, 701, 1243 (Cited on page 93.)

Demorest P. B., Pennucci T., Ransom S. M., Roberts M. S. E., Hessels J. W. T., 2010, Nature, 467, 1081 (Cited on page 81.)

Deneva J. S., Stovall K., McLaughlin M. A., Bates S. D., Freire P. C. C., Martinez J. G., Jenet F., Bagchi M., 2013a, ApJ, 775, 51 (Cited on page 82.)

Deneva J. S., Stovall K., McLaughlin M. A., Bates S. D., Freire P. C. C., Martinez J. G., Jenet F., Bagchi M., 2013b, ApJ, 775, 51 (Cited on pages 99 and 102.)

Deshpande A. A., Rankin J. M., 1999, ApJ, 524, 1008 (Cited on page 9.)

Dessart L., Burrows A., Ott C. D., Livne E., Yoon S.-C., Langer N., 2006, ApJ, 644, 1063 (Cited on page 25.)

Desvignes G., Cognard I., Champion D., Lazarus P., Lespagnol P., Smith D. A., Theureau G., 2013, in van Leeuwen J., ed., IAU Symposium Vol. 291, IAU Symposium. pp 375–377 (arXiv:1211.3936), doi:10.1017/S1743921312024179 (Cited on page 47.)

Desvignes G., et al., 2016, MNRAS, 458, 3341 (Cited on pages 93 and 105.)

Duncan R. C., Thompson C., 1992, ApJ, 392, L9 (Cited on page 20.)

Eatough R. P. et al., 2013, Nature, 501, 391 (Cited on page 20.)

Eatough R. P., Molkenthin N., Kramer M., Noutsos A., Keith M. J., Stappers B. W., Lyne A. G., 2010, MNRAS, 407, 2443 (Cited on page 44.)

Eatough R. P., Kramer M., Lyne A. G., Keith M. J., 2013, MNRAS, 431, 292 (Cited on page 42.)

Fairhead L., Bretagnon P., 1990, A&A, 229, 240 (Cited on page 22.)

Falcke H., Rezzolla L., 2014, A&A, 562, A137 (Cited on page 107.)

Ferdman R. D., et al., 2010, ApJ, 711, 764 (Cited on page 81.)

Ferdman R. D., et al., 2013, ApJ, 767, 85 (Cited on page 81.)

Ferdman R. D., et al., 2014, MNRAS, 443, 2183 (Cited on page 81.)

Fonseca E., et al., 2016, ApJ, 832, 167 (Cited on page 105.)

Freire P. C. C., Tauris T. M., 2014, MNRAS, 438, L86 (Cited on pages 25, 99 and 103.)

Freire P. C. C., Wex N., 2010, MNRAS, 409, 199 (Cited on page 95.)

Freire P. C. C., et al., 2011, MNRAS, 412, 2763 (Cited on page 102.)

Friedman H., Byram E. T., Chubb T. A., 1967, Science, 156, 374 (Cited on page 2.)

Giacconi R., Gursky H., Paolini F. R., Rossi B. B., 1962, Phys. Rev. Lett., 9, 439 (Cited on page 2.)

Ginzburg V. L., 1964, Soviet Physics Doklady, 9, 329 (Cited on page 2.)

Ginzburg V. L., Ozernoi L. M., 1965, Soviet physics, JETP, 20, 689 (Cited on page 2.)

Ginzburg V. L., Zhelezniakov V. V., 1975, ARA&A, 13, 511 (Cited on page 4.)

Ginzburg V. L., Zheleznyakov V. V., Zaitsev V. V., 1969, Soviet Physics Uspekhi, 12, 378 (Cited on page 3.)

Giroletti M., Marcote B., Garrett M. A., Paragi Z., Yang J., Hada K., Muxlow T. W. B., Cheung C. C., 2016, A&A, 593, L16 (Cited on page 111.)

Gold T., 1968a, Nature, 218, 731 (Cited on page 3.)

Gold T., 1968b, Nature, 218, 731 (Cited on page 5.)

Goldreich P., Julian W. H., 1969, ApJ, 157, 869 (Cited on pages 4 and 5.)

Gonzalez M. E., et al., 2011, ApJ, 743, 102 (Cited on pages 93 and 105.)

Gunn J. E., Ostriker J. P., 1969, Nature, 221, 454 (Cited on page 5.)

Gunn J. E., Ostriker J. P., 1970, ApJ, 160, 979 (Cited on page 52.)

Haberl F., 2004, Advances in Space Research, 33, 638 (Cited on page 25.)

Han J. L., Demorest P. B., van Straten W., Lyne A. G., 2009, ApJS, 181, 557 (Cited on page 10.)

Hankins T. H., Rickett B. J., 1975, in Alder B., Fernbach S., Rotenberg M., eds, Vol. 14, Methods in Computational Physics. pp 55–129 (Cited on page 36.)

Haskell B., Melatos A., 2015, International Journal of Modern Physics D, 24, 1530008 (Cited on page 7.)

Haslam C. G. T., Salter C. J., Stoffel H., Wilson W. E., 1982, A&AS, 47, 1 (Cited on pages 62 and 110.)

Hessels J. W. T., Ransom S. M., Stairs I. H., Freire P. C. C., Kaspi V. M., Camilo F., 2006, Science, 311, 1901 (Cited on page 17.)

Hewish A., Bell S. J., Pilkington J. D. H., Scott P. F., Collins R. A., 1968, Nature, 217, 709 (Cited on page 3.)

Hinata S., 1976, ApJ, 206, 282 (Cited on page 4.)

Hobbs G., Lorimer D. R., Lyne A. G., Kramer M., 2005, MNRAS, 360, 974 (Cited on pages 93 and 105.)

Hobbs G. B., Edwards R. T., Manchester R. N., 2006, MNRAS, 369, 655 (Cited on page 85.)

Hotan A. W., van Straten W., Manchester R. N., 2004, PASA, 21, 302 (Cited on page 104.)

Hulse R. A., Taylor J. H., 1975, ApJ, 195, L51 (Cited on pages 3 and 23.)

Istomin Y. N., Semerikov I. A., 2016, MNRAS, 455, 1938 (Cited on page 19.)

Istrate A. G., Tauris T. M., Langer N., Antoniadis J., 2014, A&A, 571, L3 (Cited on page 81.)

Jiang L., Li X.-D., Dey J., Dey M., 2015, ApJ, 807, 41 (Cited on pages 99, 103 and 106.)

Johnston S., Hobbs G., Vigeland S., Kramer M., Weisberg J. M., Lyne A. G., 2005, MNRAS, 364, 1397 (Cited on page 11.)

Johnston S., et al., 2017, MNRAS, 465, 2143 (Cited on pages 111 and 112.)

Kaplan S. A., Tsytovich V. N., 1973, Nature Physical Science, 241, 122 (Cited on page 4.)

Karako-Argaman C., et al., 2015, ApJ, 809, 67 (Cited on pages 20 and 82.)

Kardashev N. S., 1964, AZh, 4, 1807 (Cited on page 2.)

Kashiyama K., Murase K., 2017, ApJL, 839, L3 (Cited on page 108.)

Kashiyama K., Ioka K., Mészáros P., 2013, ApJ, 776, L39 (Cited on page 108.)

Keane E. F., Kramer M., 2008, MNRAS, 391, 2009 (Cited on page 25.)

Keane E. F., Stappers B. W., Kramer M., Lyne A. G., 2012, MNRAS, 425, L71 (Cited on page 107.)

Keane E. F., et al., 2016, Nature, 530, 453 (Cited on pages 106, 107, 109 and 111.)

Keane E. F., et al., 2018, MNRAS, 473, 116 (Cited on pages 61 and 108.)

Keith M. J., et al., 2010, MNRAS, 409, 619 (Cited on pages 33, 47, 51 and 82.)

King A. R., Beer M. E., Rolfe D. J., Schenker K., Skipp J. M., 2005, MNRAS, 358, 1501 (Cited on page 19.)

Klein B., Hochgürtel S., Krämer I., Bell A., Meyer K., Güsten R., 2012, A&A, 542, L3 (Cited on page 55.)

Knispel B., et al., 2015, ApJ, 806, 140 (Cited on pages 99 and 102.)

Komesaroff 1970, Nature, 225, 612 (Cited on page 4.)

Kramer M., Wielebinski R., Jessner A., Gil J. A., Seiradakis J. H., 1994, A&AS, 107 (Cited on page 91.)

Kramer M., Xilouris K. M., Lorimer D. R., Doroshenko O., Jessner A., Wielebinski R., Wolszczan A., Camilo F., 1998, ApJ, 501, 270 (Cited on page 37.)

Kramer M., Lyne A. G., O'Brien J. T., Jordan C. A., Lorimer D. R., 2006a, Science, 312, 549 (Cited on page 7.)

Kramer M., et al., 2006b, Science, 314, 97 (Cited on page 24.)

Krishnakumar M. A., Mitra D., Naidu A., Joshi B. C., Manoharan P. K., 2015, ApJ, 804, 23 (Cited on page 15.)

Lai X.-Y., Xu R.-X., 2011, Research in Astronomy and Astrophysics, 11, 687 (Cited on page 25.)

Landau L. D., 1932, Phys. Zs. Sowjet. (English and German), 1, 285 (Cited on page 1.)

Lang K. R., 1971, ApJ, 164, 249 (Cited on page 15.)

Large M. I., Vaughan A. E., Mills B. Y., 1968, Nature, 220, 340 (Cited on page 3.)

Lattimer J. M., 2012, Annual Review of Nuclear and Particle Science, 62, 485 (Cited on page 25.)

Lattimer J. M., Prakash M., 2001, ApJ, 550, 426 (Cited on page 25.)

Lattimer J. M., Prakash M., 2004, Science, 304, 536 (Cited on page 25.)

Law C. J., et al., 2017, ApJ, 850, 76 (Cited on page 107.)

Lazarus P., 2013, in IAU Symposium. pp 35–40 (Cited on page 82.)

Lazarus P., et al., 2014, MNRAS, 437, 1485 (Cited on page 80.)

Lazarus P., et al., 2015, preprint, (arXiv:1504.02294) (Cited on page 39.)

Lazarus P., Karuppusamy R., Graikou E., Caballero R. N., Champion D. J., Lee K. J., Verbiest J. P. W., Kramer M., 2016, MNRAS, 458, 868 (Cited on pages 84, 87, 103 and 104.)

Lee K. J., et al., 2013, MNRAS, 433, 688 (Cited on pages 44 and 59.)

Levin L., et al., 2010, ApJ, 721, L33 (Cited on page 20.)

Lin J., Rappaport S., Podsiadlowski P., Nelson L., Paxton B., Todorov P., 2011, ApJ, 732, 70 (Cited on page 81.)

Liu K., et al., 2014a, MNRAS, 443, 3752 (Cited on page 9.)

Liu K., Eatough R. P., Wex N., Kramer M., 2014b, MNRAS, 445, 3115 (Cited on page 24.)

Liu K., Eatough R. P., Wex N., Kramer M., 2014c, MNRAS, 445, 3115 (Cited on page 42.)

Löhmer O., Kramer M., Mitra D., Lorimer D. R., Lyne A. G., 2001, ApJ, 562, L157 (Cited on page 15.)

Löhmer O., Mitra D., Gupta Y., Kramer M., Ahuja A., 2004, A&A, 425, 569 (Cited on page 15.)

Lorimer D. R., 2005, Living Reviews in Relativity, 8, 7 (Cited on page 21.)

Lorimer D. R., 2008, Living Reviews in Relativity, 11 (Cited on page 82.)

Lorimer D. R., Kramer M., 2012, Handbook of Pulsar Astronomy. Cambridge University Press, Cambridge, UK (Cited on pages 1, 6, 10, 12, 23, 31, 32, 41, 62, 91 and 95.)

Lorimer D. R., et al., 2006, MNRAS, 372, 777 (Cited on pages 67 and 82.)

Lorimer D. R., Bailes M., McLaughlin M. A., Narkevic D. J., Crawford F., 2007, Science, 318, 777 (Cited on page 107.)

Lorimer D. R., Lyne A. G., McLaughlin M. A., Kramer M., Pavlov G. G., Chang C., 2012, ApJ, 758, 141 (Cited on page 7.)

Lorimer D. R., et al., 2015, MNRAS, 450, 2185 (Cited on page 99.)

Lynch R. S., Freire P. C. C., Ransom S. M., Jacoby B. A., 2012, ApJ, 745, 109 (Cited on page 105.)

Lyne A., Graham-Smith F., 2012, Pulsar Astronomy. Cambridge University Press (Cited on pages 15 and 17.)

Lyne A. G., McLaughlin M. A., Keane E. F., Kramer M., Espinoza C. M., Stappers B. W., Palliyaguru N. T., Miller J., 2009, MNRAS, 400, 1439 (Cited on page 21.)

Lyne A. G., Jordan C. A., Graham-Smith F., Espinoza C. M., Stappers B. W., Weltevrede P., 2015, MNRAS, 446, 857 (Cited on page 7.)

Lyne A. G., et al., 2017, ApJ, 834, 72 (Cited on page 7.)

Lyubarsky Y., 2014, MNRAS, 442, L9 (Cited on page 108.)

Manchester R. N., Lyne A. G., 1977, MNRAS, 181, 761 (Cited on page 8.)

Manchester R. N., et al., 2001, MNRAS, 328, 17 (Cited on page 47.)

Manchester R. N., Hobbs G. B., Teoh A., Hobbs M., 2005, AJ, 129, 1993 (Cited on pages 5, 17, 80 and 99.)

Marcote B., et al., 2017, ApJ, 834, L8 (Cited on page 107.)

Masui K., et al., 2015, Nature, 528, 523 (Cited on page 107.)

McLaughlin M. A., et al., 2006, Nature, 439, 817 (Cited on page 20.)

Medin Z., Lai D., 2007, MNRAS, 382, 1833 (Cited on page 18.)

Melrose D. B., Yuen R., 2016, Journal of Plasma Physics, 82, 635820202 (Cited on page 3.)

Mereghetti S., 2011, in Torres D. F., Rea N., eds, High-Energy Emission from Pulsars and their Systems. Springer, Berlin, Heidelberg, pp 345–363 (Cited on page 2.)

Migdal A., 1960, Sov. Phys. JETP, 10, 249 (Cited on page 2.)

Mingarelli C. M. F., Levin J., Lazio T. J. W., 2015, ApJL, 814, L20 (Cited on page 107.)

Morton D. C., 1964, Nature, 201, 1308 (Cited on page 2.)

Olausen S. A., Kaspi V. M., 2014, ApJS, 212, 6 (Cited on page 20.)

Oppenheim A. V., Schafer R. W., 2009, Discrete-Time Signal Processing, 3rd edn. Prentice Hall Press, Upper Saddle River, NJ, USA (Cited on page 39.)

Oppenheimer J. R., Volkoff G. M., 1939, Phys. Rev., 55, 374 (Cited on page 1.)

Özel F., Freire P., 2016, ARA&A, 54, 401 (Cited on page 81.)

Pacini F., 1967, Nature, 216, 567 (Cited on page 2.)

Pen U.-L., Connor L., 2015, ApJ, 807, 179 (Cited on page 108.)

Perrodin D., Sesana A., 2017, preprint, (arXiv:1709.02816) (Cited on page 24.)

Petroff E., et al., 2015, MNRAS, 454, 457 (Cited on page 107.)

Petroff E., et al., 2016, PASA, 33, e045 (Cited on page 107.)

Phinney E. S., 1992, Royal Society of London Philosophical Transactions Series A, 341, 39 (Cited on page 81.)

Phinney E. S., Kulkarni S. R., 1994, ARA&A, 32, 591 (Cited on pages 19 and 81.)

Pijloo J. T., Caputo D. P., Zwart S. F. P., 2012, MNRAS, 424, 2914 (Cited on page 102.)

Popov S. B., Postnov K. A., 2010, in Harutyunian H. A., Mickaelian A. M., Terzian Y., eds, Evolution of Cosmic Objects through their Physical Activity. pp 129–132 (arXiv:0710.2006) (Cited on page 108.)

Popov S. B., Turolla R., Possenti A., 2006, MNRAS, 369, L23 (Cited on page 25.)

Price D. C., 2016, preprint, (arXiv:1607.03579) (Cited on page 28.)

Proakis J. G., Manolakis D. K., 2006, Digital Signal Processing (4th Edition). Prentice-Hall, Inc., Upper Saddle River, NJ, USA (Cited on page 37.)

Radhakrishnan V., 1969, Proceedings of the Astronomical Society of Australia, 1, 254 (Cited on page 4.)

Radhakrishnan V., Cooke D. J., 1969, Astrophys. Lett., 3, 225 (Cited on pages 11 and 12.)

Radio Regulations 2012, ITU, Geneva (Cited on page 29.)

Rafikov R. R., 2016, ApJ, 830, 8 (Cited on page 105.)

Ransom S. M., 2001, PhD thesis, Harvard University (Cited on pages 38, 40 and 45.)

Ransom S. M., Eikenberry S. S., Middleditch J., 2002, The Astronomical Journal, 124, 1788 (Cited on page 41.)

Ransom S. M., Cordes J. M., Eikenberry S. S., 2003, ApJ, 589, 911 (Cited on page 42.)

Ransom S. M., et al., 2014, Nature, 505, 520 (Cited on pages 80 and 81.)

Ravi V., Shannon R. M., Jameson A., 2015, ApJ, 799, L5 (Cited on page 107.)

Ravi V., et al., 2016, Science, 354, 1249 (Cited on page 106.)

Richards D. W., Comella J. M., 1969, Nature, 222, 551 (Cited on page 3.)

Romani R. W., Narayan R., Blandford R., 1986, MNRAS, 220, 19 (Cited on page 15.)

Ruderman M. A., Sutherland P. G., 1975, ApJ, 196, 51 (Cited on page 4.)

Salpeter E. E., 1960, Annals of Physics, 11, 393 (Cited on page 1.)

Scheuer P. A. G., 1968, Nature, 218, 920 (Cited on page 15.)

Scholz P., et al., 2016, ApJ, 833, 177 (Cited on page 107.)

Shannon R. M. et al., 2018, Nature, 562, 386 (Cited on page 107.)

Shapiro I. I., 1964, Phys. Rev. Lett., 13, 789 (Cited on pages 22 and 84.)

Shklovskii I. S., 1970, Soviet Ast., 13, 562 (Cited on page 93.)

Shklovsky I. S., 1967, ApJ, 148, L1 (Cited on page 2.)

Spitler L. G., et al., 2014, ApJ, 790, 101 (Cited on page 107.)

Spitler L. G., et al., 2016, Nature, 531, 202 (Cited on page 107.)

Splaver E. M., Nice D. J., Arzoumanian Z., Camilo F., Lyne A. G., Stairs I. H., 2002, ApJ, 581, 509 (Cited on pages 81, 97 and 99.)

Staelin D. H., Reifenstein III E. C., 1968, Science, 162, 1481 (Cited on pages 3 and 45.)

Stovall K., et al., 2014, ApJ, 791, 67 (Cited on pages 33, 66, 77 and 82.)

Swiggum J. K., et al., 2015, ApJ, 805, 156 (Cited on page 80.)

Tan C. M., et al., 2018, ApJ, 866, 54 (Cited on page 17.)

Tauris T. M., 2011, in Schmidtobreick L., Schreiber M. R., Tappert C., eds, Astronomical Society of the Pacific Conference Series Vol. 447, Evolution of Compact Binaries. p. 285 (arXiv:1106.0897) (Cited on page 80.)

Tauris T. M., Savonije G. J., 1999, A&A, 350, 928 (Cited on pages 19 and 81.)

Tauris T. M., van den Heuvel E. P. J., 2006, Formation and evolution of compact stellar X-ray sources. Cambridge University Press, pp 623–665 (Cited on pages 80 and 102.)

Tauris T. M., van den Heuvel E. P. J., Savonije G. J., 2000, ApJ, 530, L93 (Cited on pages 19, 81 and 98.)

Tauris T. M., Langer N., Kramer M., 2011, MNRAS, 416, 2130 (Cited on page 81.)

Tauris T. M., Langer N., Kramer M., 2012, MNRAS, 425, 1601 (Cited on page 80.)

Tauris T. M., Langer N., Podsiadlowski P., 2015, MNRAS, 451, 2123 (Cited on pages 80 and 81.)

Taylor J. H., 1992, Royal Society of London Philosophical Transactions Series A, 341, 117 (Cited on pages 21 and 104.)

Taylor J. H., Weisberg J. M., 1982, ApJ, 253, 908 (Cited on pages 84 and 95.)

Taylor J. H., Fowler L. A., McCulloch P. M., 1979, Nature, 277, 437 (Cited on page 24.)

Tendulkar S. P., et al., 2017, ApJ, 834, L7 (Cited on page 107.)

Thornton D., et al., 2013, Science, 341, 53 (Cited on page 107.)

Tolman R. C., 1939, Phys. Rev., 55, 364 (Cited on page 1.)

Totani T., 2013, Publications of the Astronomical Society of Japan, 65, L12 (Cited on page 107.)

Tsuruta S., Cameron A. G. W., 1965, Nature, 207, 364 (Cited on page 2.)

Verbiest J. P. W., et al., 2016, MNRAS, 458, 1267 (Cited on page 24.)

Verbunt F., Freire P. C. C., 2014, A&A, 561, A11 (Cited on page 80.)

Verbunt F., Igoshev A., Cator E., 2017, A&A, 608, A57 (Cited on page 52.)

Wang N., Manchester R. N., Johnston S., 2007, MNRAS, 377, 1383 (Cited on page 21.)

Weltevrede P., Stappers B. W., Rankin J. M., Wright G. A. E., 2006, ApJL, 645, L149 (Cited on page 20.)

Wex N., 2014, preprint, (`arXiv:1402.5594`) (Cited on page 23.)

Wex N., Kalogera V., Kramer M., 2000, ApJ, 528, 401 (Cited on page 81.)

Williams P. K. G., Berger E., 2016, ApJ, 821, L22 (Cited on page 111.)

Wolszczan A., Frail D. A., 1992, Nature, 355, 145 (Cited on page 80.)

Yao J. M., Manchester R. N., Wang N., 2017, ApJ, 835, 29 (Cited on pages 32, 66, 68, 89 and 93.)

Zeldovich Y. B., 1962, Soviet physics, JETP, 14, 1143 (Cited on page 1.)

Zeldovich Y. B., Guseynov O. H., 1966, ApJ, 144, 840 (Cited on page 2.)

Zhang B., Gil J., Dyks J., 2007, MNRAS, 374, 1103 (Cited on page 20.)

Zhu W. W., et al., 2014, ApJ, 781, 117 (Cited on pages 44 and 61.)

Zwart S. P., van den Heuvel E. P. J., van Leeuwen J., Nelemans G., 2011, ApJ, 734, 55 (Cited on page 102.)

de Freitas Pacheco J. A., Steiner J. E., Neto A. D., 1977, A&A, 55, 111 (Cited on page 2.)

van Straten W., Demorest P., Oslowski S., 2012, Astronomical Research and Technology, 9, 237 (Cited on pages 64 and 104.)

van den Heuvel E. P. J., 1989, in Ögelman H., van den Heuvel E. P. J., eds, NATO Advanced Science Institutes (ASI) Series C Vol. 262, NATO Advanced Science Institutes (ASI) Series C. p. 523 (Cited on page 19.)

van den Heuvel E. P. J., 1994, A&A, 291, L39 (Cited on pages 81 and 99.)